

MICROSECOND PULSED GRIMM GLOW DISCHARGE
TIME-OF-FLIGHT MASS SPECTROMETRY
STUDY OF AERSOLS GENERATED BY
NEBULIZATION AND LASER ABLATION

By

FARZAD FANI-PAKDEL

A DISSERTATION PRESENTED TO THE GRADUATE SCHOOL
OF THE UNIVERSITY OF FLORIDA IN PARTIAL FULFILLMENT
OF THE REQUIREMENTS FOR THE DEGREE OF
DOCTOR OF PHILOSOPHY

UNIVERSITY OF FLORIDA

2009

© 2009 Farzad Fani-Pakdel



To my mom, Farideh Arjmand, and My dad, Manouchehr Fani-Pakdel
To my brothers, Kiumars and Kiarash
To my sister, Azar



ACKNOWLEDGMENTS

I thank my advisor, Professor Nicolo Omenetto, for giving me the opportunity to work in his lab and for supporting my research over the course of the last five years. He provided me with insightful advice throughout my education, and always gave encouragement when I faced difficulties in my research. He analyzed my results with extreme thoughtfulness and suggested better approaches and new ideas. I also learned from him to have the courage to address my results scientifically. I will always appreciate his patience, wisdom and kindness; lo ringrazio dalle profondità del mio cuore.

I also want to mention my previous advisor, Dr. Jason Telford at the University of Iowa, where I earned my Master of Science in chemistry. From him, I learned lots of important things about approaching problems. He taught me that it is important not to be afraid of problems and always think of things as if they are simple and manageable. I will never forget his wisdom and kindness and will always appreciate being his student.

I would also like to thank Professor James Winefordner for his scientific and moral support during my years of study. He was always a source of energy and encouragement. Dr. Ben Smith was always a reliable source of advice in science and academia. I will always remember his kindness and hospitality upon first applying to join the chemistry department at the University of Florida. I also thank Dr. Igor Gornushkin for his contributions to my research and for his friendship.

I am grateful for the additional guidance by Dr. Harrison in the field of glow discharge and his kindness in lending me beneficial books and also allowing me to use some of the images from his group for this dissertation. I thank Dr. Kevin Turney for helping me at the beginning with the basics of the glow discharge mass spectrometer.

I express my appreciation to past and current students in the Omenetto-Smith-Winefordner group for their friendship and support during these years: Jonathan Merten, Ronald Whiddon, Dr. Mariela Rodriguez, Dan Shelby, Anderson Warren, Heh young moon, Dr. Benoit Lauly, Dr. Nick Taylor, Dr. Kate Herrera, Dr. Lydia Edwards, Akua Oppong-Anane, Dr. Joy Guingab and Lydia Edwards. Jonathan was a great friend, and excelled in aiding me with any and all technical issues, as well as fielding my questions about optics. I always enjoyed discussing scientific and social matters with him. Through his electronics expertise, Ron helped me a lot with my research and the time-of-flight instrument. Mariela and Kate were good friends who imparted a lot of useful information to me. Mariela was always a source of energy and encouragement as well. Benoit and Nick always helped me with my optical questions. Dan Shelby was a great friend with whom I enjoyed discussing experimental matters. Andrew was a great friend who was always there to help when asked. Heh young was a kind friend and I specially thank her for filming my final defense. I also thank Lydia and Dan for helping me with my tie before the oral exam and final defense, respectively.

I also thank my PhD committee members, Dr. Yost, Dr. Powell, Dr. Eyler, Dr. Hahn and the late Dr. Zaman for their scientific contributions to my dissertation. Dr. Yost is a great teacher, and my interest in mass spectrometry was really shaped after taking his class. He was always available to answer my random questions. Dr. Powell is a very friendly scientist that always had his door open to helping me solve problems with my instruments. He was often the first person I would seek advice from. I also thank Dr. Eyler for supporting me when I needed help. He also helped me with editing my dissertation with accuracy and extreme care. I thank him for reading my work carefully and suggesting useful changes. I thank Dr. Hahn for sharing interesting ideas during my final defense and also during the laser ablation symposium in New

Orleans. Dr. Zaman was a very kind scientist at the Department of Material Science and I always enjoyed talking to him. I will always remember him and wish the best for his wife and family. I also thank Dr. Martin for what I learned about nano-science while in his group, especially making conical nano-pores.

I thank the Department of Chemistry at the University of Florida for supporting me during the last 5 years with teaching assistantship. I thank all the kind faculty members whom I was a teaching assistant for: Dr. Young, Dr. Horvath, Dr. Keaffaber, Dr. Mitchell, Dr. Christou, Dr. Fanucci, Dr. Angerhofer, Dr. Ucak and finally Dr. Williams. I thank Dr. Kathryn Williams for being a very kind and considerate supervisor. During my time as her TA, I learned a lot of useful techniques and concepts in analytical chemistry, while teaching for her. Without her support I would have a very difficult time. Dr. Ucak was also a good friend who always gave me her support.

I would like to acknowledge Joe Shalosky, Brian Smith and Todd Prox in the machine shop, Steven Miles and Larry Harley in the electronic shop and Stephen Pritchard and Joseph Carvson in IT shop for providing me with technical support during my research. Without Joe's help, many designed parts that helped me during my research would not be built. I would also like to mention the kind and effective help by Jeanne Karably and Antoinette Knight, the analytical chemistry division secretaries. Without their help things would not be as easy.

It is important to remember the kind consideration of LECO Corporation in providing technical support in maintenance and repair of the Renaissance time-of-flight mass spectrometer. I especially thank Dr. Eric Oxley for his kind attention during my communications with LECO. I also like to thank Dr. Fred Smith from CETAC Corporation for providing me with technical information on the nebulizer-dehydrator. I express my appreciation to the kind members of Dr.

Hieftje's group at Indiana University, Dr. William Wetzel and Dr. Steven Ray, who always helped me with troubleshooting the time-of-flight mass spectrometer.

I would like to acknowledge my chemistry high school teacher Mr. Soleymani who was one of the main reasons for my interest in chemistry. Also, I thank my undergraduate advisors during Iranian National Chemistry Olympiad and undergraduate studies, Dr. Abedini, Dr. Seyyedi, Dr. Nejat, Dr. Aghaei, Dr. Boghaei, and Dr. Maghari in the University of Tehran and the Sharif University of Technology in Iran. Without their guidance it would not have been possible for me to do my best.

Finally, I thank my family and friends for their support during the last six years. I truly appreciate the friendship of my dear Iranian friends in Gainesville: Dr Masoumeh Rajabi (also known as Masi), Ashkan Behnam, Babak Mahmoodi, Saeed Moghaddam and Ayyoub Mehdizadeh. Ashkan helped me with modeling the electric field and Ayyoub was nice enough to run a modeling of flows in fluids. Masi was a great help in editing my dissertation and pushing me to get things done. She is a very strong and giving person. Babak helped me with processing my mass spectra on computer using MATLAB. Saeed was always a great help with my computer related issues. I also like to thank my former students and friends Katherine Winter, Samantha McCall, Alexandria Berry, Kasia Cudzilo, Chenan Zhang and Bernadette Boac for their friendship. Katie Winter and Sam helped me with parts of this dissertation in editing the English. My friend Heera Sharma was also a great help in editing Chapter 5 of my dissertation. I also thank Valori Chapman for doing a good job in helping me with typing and editing. My good friend Julie heaweon Park was also a great friend who always encouraged me not to give up and try hard.

Last, but not the least, I express gratitude to my parents, Manouchehr and Farideh, my brothers Kiumars and Kiarash, my sister Azar and my brother-in-law Mohamad-Reza and my sisters-in-law Shokofeh and Atusa for their encouragement during all stages of my life. My beautiful nephews and nieces Alvand, Sahand, Armita and Raha, were always inspiration when I looked at their photos. I cannot wait to see and hug them in person.

I thank my dad for being a kind father and always teaching me interesting things with his wisdom. I especially thank my mom for always caring for me and doing all she can to keep me healthy and strong. She was always there to support me during all the years of my education. For bringing and sending me food from thousands of miles away and for cooking for me when she visits, I am particularly grateful.

TABLE OF CONTENTS

	<u>page</u>
ACKNOWLEDGMENTS.....	4
LIST OF TABLES.....	12
LIST OF FIGURES	13
ABSTRACT	19
CHAPTER	
1 GLOW DISCHARGE.....	21
Introduction	21
Different Regions of Glow Discharge	21
Cathode Dark Space	22
Negative Glow	23
Faraday Dark Space.....	24
Glow Discharge Reactions and Processes	25
Cathode Sputtering	25
Collisional Reactions in Plasma	28
Electron behavior	29
Sputtered species excitation and ionization.....	29
Excitation.....	30
Ionization	30
Modes of Operation.....	31
Direct Current	31
Pulsed Discharge.....	32
Radio Frequency.....	32
Source Configurations	32
Hollow Cathode Geometry	33
Diode (Coaxial) Geometry	34
Grimm Geometry.....	34
2 EXPERIMENTAL DETAILS AND BACKGROUND	46
Introduction	46
Aerosols	46
Aerosol Generation.....	46
Nebulizer-Dehydrator Efficiency	47
Particle Size Distribution Measurements	49
Microscopy method.....	49
Particle impaction method.....	50
Light interaction method.....	50
Electrical property method	50

Sedimentation method	51
Limitations of Particle Sizing Methods.....	51
Presentation of Particle Size Measurement Results	52
Glow Discharge Source	54
Mass Spectrometer	54
Modifications	55
Repeller Modulator Timing.....	56
TOF-MS Detector and Collecting Mass Spectrum.....	58
3 A NOVEL PULSED GRIMM-TYPE GLOW DISCHARGE SOURCE FOR IONIZATION OF SALT AEROSOLS	69
Introduction	69
Experimental.....	71
Aerosol Generation and Particle Size Distribution.....	71
Mass Spectrometer.....	72
Grimm-Type GD Ion Source	73
Cathode modification.....	73
New anode design	73
Pressure and Flow Measurements	74
Results and Discussion	74
Anode A vs. B.....	75
Cathode Dark Space (CDS)	76
Effect of the Flow and Source Pressure	77
Effect of the First Stage Pressure.....	79
Effect of the Cathode Potential Pulse Width	79
Effect of the Cathode Potential.....	80
CsI vs. NaI at Different Repeller Delay Times.....	80
Ionization Mechanism and Sodium vs. Cesium Signal Comparison	81
4 PULSED-GLOW DISCHARGE MASS SPECTROMETRY OF PARTICLES: FUNDAMENTAL STUDIES AND DIAGNOSTICS	96
Introduction	96
Experimental.....	97
Results and Discussion	97
Effect of Solution Concentration	97
Relative Sensitivity Factors.....	98
Effect of Skimmer Orifice.....	98
Effect of Cathode Temperature.....	99
Particle Vaporization Efficiency.....	99
Effect of Background Salt.....	103
Effect of Particle Ionization on Discharge Species	103
Effect of Cathode Potential–Particle Ionization Mechanism.....	104

5	PULSED GRIMM GLOW DISCHARGE TIME-OF-FLIGHT MASS SPECTROMETRY STUDY OF AEROSOLS GENERATED BY LASER ABLATION OF SOLID SAMPLES.....	119
	Introduction	119
	Glow Discharge and Lasers	120
	LA-ICP-MS.....	121
	Ideal LA-ICP-MS System	121
	Fractionation	121
	Particle Size Effect And Use Of Femto-Second Lasers	122
	Carrier Gas of Choice	122
	Laser Pulse Duration	123
	Experimental.....	123
	Ablation Cell.....	124
	Lasers.....	124
	Materials.....	125
	Results and Discussion	125
	Relative Signal Intensities for Different Matrices	128
	The Effect of Cathode Potential on Particle Ionization.....	129
	Crater Shape in Bismuth Sample	130
	Effect of Laser Pulse Energy	130
	Investigation of Particle Ionization Mechanism	130
	Laser Back Ablation of Thin Films	131
	Effect of Laser Ablation and Particle Introduction on Other Discharge Species	133
6	CONCLUSION AND FUTURE WORK	160
	APPENDIX: COMPLEMENTARY FIGURES.....	164
	LIST OF REFERENCES	176
	BIOGRAPHICAL SKETCH	182

LIST OF TABLES

<u>Table</u>		<u>page</u>
1-1	Ionization processes in a glow discharge plasma. Ionization is characterized by primary and secondary ionization processes.	36
2-1	Results of efficiency measurements for ultrasonic nebulizer dehydrator.....	60
2-2	Results of nebulizer-dehydrator efficiency using conductivity measurements.....	60
2-3	Typical operating conditions for time-of-flight mass spectrometer.....	61
3-1	Summary of the experimental parameters.	84
3-2	Thermodynamic properties of CsI and NaI. ⁸¹	85
4-1	Dry particle mean volume diameters (DV) for different concentrations of CsI and NaI.....	105
5-1	The chemical composition of sample material used in laser ablation in mass%.	135
5-2	Relative intensities of particle ionization from ablation of different solid samples.	135
5-3	Particle mean volume diameters (D _v) for aerosol generated by laser ablation of different samples	136

LIST OF FIGURES

<u>Figure</u>	<u>page</u>
1-1	Diagram of voltage vs. current regimes for various discharge..... 37
1-2	Various regions of a glow discharge..... 38
1-3	The three main regions in a simple glow discharge vs. voltage distribution as a function of distance to cathode..... 39
1-4	Major events in the glow discharge: Cathode sputtering and ionization-excitation in the negative glow. 40
1-5	Cathode sputtering due to fast ion/fast atom impact..... 41
1-6	Sputter yield for various elements in the periodic table 41
1-7	The most common types of interaction in the plasma. 42
1-8	Direct and pulsed glow discharge modes are compared..... 43
1-9	Hollow cathode glow discharge source for mass spectrometry 44
1-10	Diode geometry with a direct insertion probe (DIP)..... 44
1-11	Grimm glow discharge geometry for mass spectrometry..... 45
2-1	The schematics of the ultrasonic nebulizer-dehydrator. 62
2-2	The schematics of the particle impactor 62
2-3	The differential mobility analyzer measures the particle size based on their mobility vs. their attraction within electric field 63
2-4	The condensation particle counter (CPC) counts the number of particles after they pass through the DMA unit 63
2-5	Comparing the results of different particle sizing methods..... 64
2-6	The diagram shows continuous ion source (red) vs. the modulator-repeller gating pulses, for the original ICP-MS design..... 64
2-7	The diagram shows the pulsed GD ion source (red) vs. the modulator-repeller gating pulses..... 65
2-8	The schematics of repeller and modulator with respect to the pulsed ion source..... 65
2-9	The timing diagram for the time-of-flight trigger vs. the repeller and modulator 66

2-10	The effect of changing different instrument variables on timing diagram	67
2-11	A sample mass spectrum from the instrument software	68
2-12	A sample mass spectrum from the oscilloscope.....	68
3-1	The overall schematic of the instrumentation for pulsed GDMS of particles	86
3-2	Schematic of the cathode design for particle introduction	86
3-3	Anode A vs. B	87
3-4	Detailed view of the ionization source with anode B	87
3-5	The sharp edge of the cathode orifice, where the particles enter the discharge, was etched due to sputtering	88
3-6	The Cs ⁺ ion signal vs. repeller delay time from CsI aerosols for the two anode configurations	88
3-7	The electric field of anode A vs. B	89
3-8	Ar and Cs signal vs. repeller delay at three different aerosol flow rates into the source	90
3-9	Effect of the first stage pressure on signal profile and intensity	91
3-10	Pulse width, where the two pulse durations of 30 μs and 150 μs are compared for Cs signal	92
3-11	Effect of the cathode potential on particle ionization for CsI and NaI	93
3-12	Signal vs. delay time for different elements	94
3-13	Particles enter from the cathode (left). After vaporization, atomization and ionization, if atoms make it out of the CDS, they can ionize in the negative glow	94
3-14	The heavier Cs ion travels 6 times farther than Na before it goes back towards the cathode	95
4-1	Quantitative study of cesium iodide with different solution concentrations	106
4-2	Quantitative study of sodium iodide with different solution concentrations	106
4-3	Modeling the flow for the glow discharge source.....	107
4-4	Effect of skimmer orifice size and heating the cathode on sensitivity for Cs, I and Na..	108

4-5	Effect of cathode potential for CsI 4 mM at cathode temperature = 75°C and skimmer orifice diameter = 0.56 mm.....	109
4-6	Effect of cathode potential for NaI 4 mM. Cathode temperature = 75°C and skimmer orifice diameter = 0.56 mm.	110
4-7	The change in signal vs. cathode potential for iodine ion using a 4.0 mM cesium iodide solution.	111
4-8	Comparing the ion signal vs. salt concentration for the experimental results vs. partial vaporization model.	112
4-9	Mean volume diameters for different CsI concentrations.	113
4-10	Cs ⁺ ion signal from 2 mM CsI in different NaI backgrounds.	114
4-11	Signal vs. concentration for Na ⁺ ion at different NaI concentrations at the presence of 2 mM CsI background compared with no background.....	115
4-12	Iodine ion signal resulted from different NaI solutions at the presence of 2 mM CsI.....	116
4-13	The effect of particle introduction on argon and copper ion signals.	117
4-14	Comparing the effect of cathode potential on different ion signals.....	118
5-1	Overall experimental set up for LA-GD-MS. Only the skimmer of time-of-flight is shown.	137
5-2	The geometrical dimensions of the ablation cell. All dimensions are in millimeters.....	137
5-3	Iron signal resulted from ablation of stainless steel using power-chip Nd:YAG laser....	138
5-4	Mass spectrum resulted from ablation of stainless steel using the Q-switched, flashlamp-pumped Nd:YAG laser at its maximum pulse power	138
5-5	Monitoring the ⁵⁶ Fe ion signal as a function of time for 300 seconds	139
5-6	Monitoring the ⁵⁶ Fe ion signal as a function of time for ablation of stainless steel using 11 single laser shots	140
5-7	Monitoring the ²⁰⁹ Bi ion signal as a function of time for laser ablation of bismuth alloy.....	141
5-8	Monitoring the ⁵⁶ Fe and ⁶³ Cu ion signals as a function of time for approximately 13 minutes of stainless steel ablation	142
5-9	Iron, copper and zinc ion signals, at 4 different time domains.	142

5-10	The signal ratio for ^{56}Fe to ^{63}Cu , almost remains constant for the 13 minutes duration of laser ablation.	143
5-11	The cathode signal from sputtering the brass cathode increases due to ablation of a brass sample.....	143
5-12	Mass spectrum from laser ablation of a Macor sample	144
5-13	Mass spectrum from laser ablation of a bismuth alloy sample	144
5-14	Cesium signal vs. mole % of cesium at different salt pellets.	145
5-15	Particle size distributions for aerosols generated from different samples.	145
5-16	The effect of cathode potential on ionization of stainless steel particles (^{56}Fe signal) is compared with its effect on cathodic sputtering of brass (^{63}Cu signal).	146
5-17	The effect of cathode potential on ionization of Macor particles.	147
5-18	The effect of cathode potential on ionization of salt particles.	147
5-19	Crater image of bismuth sample after ablation by 219 laser shots at 10 Hz and maximum energy.....	148
5-20	The crater profile shape and dimension measured by an optical profilometer. After ablation by 219 laser shots at 10 Hz and maximum laser energy.	149
5-21	The effect of laser pulse energy on LA-GD-MS Bi ion signal of bismuth alloy particles.	150
5-22	The effect of laser pulse energy on ^{209}Bi to ^{208}Pb signal ratio.	150
5-23	Memory effect investigation: The initiation of glow discharge after ablation of bismuth sample (305 shots) ended resulted in a spike in Bi signal.....	151
5-24	Particle deposition and laser back ablation of bismuth alloy on quartz window.	152
5-25	Ablation cell set up for laser back ablation of sample from the surface of the quartz window.....	152
5-26	Ablation cell set up for laser back ablation of a thin stainless steel film located above a sample of aluminum.....	153
5-27	Signal vs. time for back ablation of stainless steel followed by regular ablation of aluminum sample	153
5-28	Crater diameters for stainless steel and aluminum.....	154

5-29	Spike in copper signal due to entrance of stainless steel particles into the discharge, by a single laser shot.	154
5-30	Increase in copper signal due to entrance of a 20 second ablated package of stainless steel particles into the discharge.....	155
5-31	The effect of ablation of stainless steel on Ar ⁺ and ArH ⁺ ion signals. The right hand Y-axis is for the argon ion only.....	156
5-32	The effect of bismuth alloy ablation on Ar ⁺ ion signal.....	157
5-33	The effect of 4 single shots of laser ablation of bismuth alloy on ⁶³ Cu ⁺ ion signal. No significant change in copper ion signal is observed.....	158
5-34	The effect of ablation of Macor on ⁴⁰ Ar ⁺ and ArH ⁺ ion signals.....	159
5-35	The effect of ablation of Macor on ⁶³ Cu ⁺ signal	159
A-1	Calibration of the digital flow meter by the soap bulb method. The real value of flow in standard cubic centimeter per min is shown.	164
A-2	Calibration of the argon flow into the glow discharge with respect to the first stage pressure	165
A-3	Signal intensities for Cs and I at three different concentrations of CsI solution are shown.	166
A-4	Repeller and modulator ringing from the oscilloscope is shown	167
A-5	The sources of particle and ion loss before the skimmer of time-of-flight are shown. ...	168
A-6	Calculation of the number of ions expected to arrive at the detector assuming 100% ionization and ion transfer efficiency.	168
A-7	The overall efficiency of the particle vaporization-atomization-ionization and ion transfer to detector is calculated.....	169
A-8	Calibration graph for conductivity vs. concentration of CsI.	170
A-9	Result of the particle size distribution measurement for ablation of Macor. Relative abundances of dN/dD is compared to N	171
A-10	The particle size distribution for Macor aerosol is shown as dV/dD	171
A-11	The effect of ablating stainless steel by the power-chip Nd: YAG laser on copper signal	172
A-12	Geometrical modification of cathode resulted in ion signal as high as 22 mV for Cs ⁺ upon nebulization of a 4 mM CsI solution.	173

A-13	The Cs ⁺ signal vs. delay time is shown as well as the error bars	174
A-14	The signal for Cs ⁺ ion vs. CsI concentration show a linear dynamic range from 0.50 mM to at least 10.0 mM.....	175

Abstract of Dissertation Presented to the Graduate School
of the University of Florida in Partial Fulfillment of the
Requirements for the Degree of Doctor of Philosophy

MICROSECOND PULSED GRIMM GLOW DISCHARGE TIME-OF-FLIGHT MASS
SPECTROMETRY STUDY OF AERSOLS GENERATED BY NEBULIZATION AND
LASER ABLATION

By

Farzad Fani-Pakdel

August 2009

Chair: Nicolo Omenetto
Major: Chemistry

This dissertation discusses the experimental results for interaction of particles with the glow discharge plasma. The objective is to investigate the potential ability of a glow discharge (GD) for ionization of aerosols. In this work, a Grimm-type microsecond pulsed-GD source coupled with a time-of-flight mass spectrometer (TOFMS) were used for producing and detecting the ions formed after the introduction of the aerosol stream into the plasma.

At first, as a source for aerosols, an ultrasonic nebulizer-dehydrator unit was used to generate simple salt particles such as cesium iodide. The geometrical design of choice was found to be a modified Grimm-type source in which particles enter the plasma through an orifice in the middle of the cathode and instead of a conventional cylindrical anode, an anode with four off-centered holes was used. The effect of argon flow, source pressure, pulse potential and repeller delay on signal intensity was studied for NaI and CsI particles.

The optimum condition was used for quantitative studies. The signal had a linear correlation with the concentration of the nebulized salt solution. Heating the cathode was found to improve the signal reproducibility and also sensitivity (approximately 1.3 times). At the

optimum condition and heating the cathode to 75 degrees Celsius, a sensitivity of approximately 1.8 mV/mM for cesium was achieved.

Another interesting observation was that the higher-mass ions such as cesium and iodide resulted in larger signals compared to lower-mass ions such as sodium (approximately 10:1 ratio). It was concluded that this was mainly due to the fact that more massive ions experience less scattering at the skimmer orifice. This discrimination between higher-mass and lower-mass ions was reduced by using a larger skimmer orifice ($\text{Cs}^+ : \text{Na}^+ = 2:1$).

Finally, an aerosol stream was generated by laser ablation of solids in an external cell. The ablation lasers were a power-chip Nd:YAG laser and a Q-switched, flashlamp-pumped Nd:YAG laser. The samples investigated were aluminum, stainless steel, brass, bismuth alloy, ceramic and pressed pellets of inorganic salts. The effects of laser pulse frequency, energy and discharge potential on particle ionization were studied. Due to better signal stability and intensities, the laser ablation was found to be a more suitable method for aerosol generation when glow discharge is the ion source.

CHAPTER 1 GLOW DISCHARGE

Introduction

When a cathode and an anode are immersed in an inert gas such as argon and sufficient electrical potential is applied to that gas, an electric breakdown occurs. The gas breakdown results in the formation of electrons and ions, which allows current to flow through the gaseous medium. This breakdown of the gaseous medium and the resulting current is called a discharge or plasma.¹⁻³ Gas pressure, gas type, cathode material, temperature and electrode distance are all factors that play a role in determining the gas breakdown potential.^{4,5} Electrons, positive ions and negative ions are all formed during breakdown and maintain the discharge. The cathode surface is bombarded by the positive ions and a sputtering event is initiated. Analyte atoms are released from the bulk sample due to the sputtering and can then be analyzed. The discharge becomes “self-sustaining” due to charged species being continually produced by collisional events within the plasma.³⁻⁶

Voltage and current characteristics define the operating regimes of discharges and differentiate them from each other. The operating regimes of discharges, with features close to a glow discharge, are shown in Figure 1-1. For both the optical emission and mass spectrometry detection methods, the discharge is maintained in the abnormal mode with the purpose of obtaining the greatest amount of analytical information. Throughout this document, an abnormal glow discharge will be referred to as the glow discharge.

Different Regions of Glow Discharge

The glow discharge is made up of multiple regions as shown in Figure 1-2. The formation of these regions depends on the configuration of the glow discharge cell, in particular the distance separating the electrodes. A highly luminescent positive column region is most

important when the inter-electrode distance is large enough; however, to sustain a glow discharge, it is not required. As the distance between electrodes decreases, this region shortens and eventually disintegrates. Decreasing the electrode separation also causes other regions of the discharge to be diminished, with the exception of the cathode dark space. The cathode dark space must exist to sustain a glow discharge. Most analytical glow discharge devices utilize short electrode distances, so they generally exhibit only the cathode dark space and negative glow regions. When the electrode separation is only a few times larger than the thickness of the cathode dark space, an obstructed glow occurs. This is a discharge in which most of the regions have collapsed.^{7, 8} A distorted dark space region and an unstable, or extinguished, plasma will occur with a further decreased electrode separation. Three prominent regions of the glow discharge include: the cathode dark space, negative glow and Faraday dark space.

Cathode Dark Space

The cathode dark space is a region with low luminosity next to the cathode surface, as shown in Figure 1-2. The negative cathode potential causes electrons to be repelled away from this region, which creates a positive space where most of the potential difference between the two electrodes is dropped.⁴ For this reason, the cathode dark space is often called the cathode fall region.

Figure 1-3 shows a profile of potential distribution as a function of electrode distance for the three major regions of the glow discharge. The figure shows the large potential fall of the cathode dark space region. Electrons are accelerated away from the cathode dark space region and therefore have too much energy for excitation reactions. An excitation cross-section shows a dip at these high energies,^{5, 6} accounting for the low luminosity of the cathode dark space. Since electrons and ions gain extra energy by electric field, the energy distribution of charged species

in this region does not follow a Maxwell distribution. As a result, the cathode fall region is far from a hydrodynamic equilibrium.⁷

A glow discharge cannot exist without the cathode dark space region, even though there is a lack of excitation and ionization processes in this region. Electrons that are accelerated away from the cathode dark space region are responsible for ionizing the gas (Ar) in other regions of discharge. These collisions create electrons, which may cause further ionization and the resulting argon ions are attracted to the cathode. These complex processes are a continuous cycle which leads to a self-sustaining discharge, originating from the acceleration of electrons in the cathode dark space region.

Negative Glow

The negative glow region is a large, bright region adjacent to the cathode dark space and is analytically the most important region of the glow discharge.^{2,4} Both fast, highly energetic electrons and slow, thermal electrons enter the negative glow. Fast secondary electrons are the electrons that are created at the cathode and have passed through the cathode dark space without losing significant energy by collisions. Due to their inherent high energies, these electrons (group I electrons) are only capable of ionizing collisions. It has been shown that group I electrons attain energies of ~20 – 25 eV and number densities of around 10^6 cm^{-3} in the negative glow region.⁸ Another name for these electrons is MC (Monte Carlo) electrons (page 161, reference 2).³

Low-energy or thermal electrons are separated into two groups. Group II electrons are secondary electrons of gas-phase ionization collisions that have electron temperatures of ~2 – 10 eV, and number densities of about $10^7 - 10^8 \text{ cm}^{-3}$.⁸ Electrons from group I or group II that have been through several elastic and inelastic collisions within the plasma are termed group III electrons. These electrons have electron temperatures of 0.05 – 0.6 eV and number densities in

the range of $10^9 - 10^{11} \text{ cm}^{-3}$.⁸ Group II and group III electrons may either excite atomic species or ionize excited state species.⁹

The number of electrons in the negative glow is typically matched by a similar number of positive ions⁴ and the combination of these free ions and electrons results in an essentially field-free region. This region is represented in the potential distribution of a linear segment just above ground potential (V_0) as seen in Figure 1-3. It has been shown that plasma potentials within the negative glow region vary less than 1 V for discharge voltages between 800 and 1000 V.⁸ In this field-free region, electrons are not significantly accelerated and are capable of causing excitation collisions resulting in a bright glow. The discharge gas and, to a lesser degree, the cathode material are responsible for the color of this glow.³

Both the discharge pressure and the distribution of electron energies affect the size of the negative glow region. The number of collisions within the discharge is increased with high operating pressures; this will result in shortening of the negative glow region. A wide range of electron energies, however, can extend the length of this region. Electron multiplication by ionization processes results in the largest population of electrons existing at the interface between the cathode dark space and the negative glow. The greatest emission intensity is also seen at this edge of the negative glow, which fades as a function of cathode distance. Mass spectrometers are able to analyze the high population of ions that exist at this negative glow interface.^{2, 4}

Faraday Dark Space

The Faraday dark space region is the region just before the anode end of the negative glow.²⁻⁴ Electrons that make up the Faraday dark space are thermal electrons, having lost most of their energy due to excitation and ionization collisions.⁴ The separation between the cathode and anode is often so small that this region of low luminosity is not observed.

Glow Discharge Reactions and Processes

The glow discharge is a simplified analytical device full of chaotic processes involving multiple species of varying energy. Summarizing these basic processes will be beneficial to understanding the experimental results in the following chapters. This section will present an overview of the mechanisms that occur within the spatial regions depicted in the previous section. Figure 1-4 illustrates the fundamental processes that will be described in this section, including sputtering, excitation and ionization.

Cathode Sputtering

Sputtering is the phenomenon that occurs when an energetic particle strikes a solid surface and results in the initiation of many processes. Sputtering is a substantial contributor to the analytical utility of the glow discharge. Ion bombardment of the sample surface causes atomization of the sample and provides an atomic population for later excitation and ionization processes.⁴ An overview of the sputtering process, as well as quantitative principles for characterizing sputtering, are given in this section.

Sputtering process: Figure 1-5 illustrates the particle impact, which can lead to extensive sample damage through atom rearrangement or particle implantation. The figure simplifies the sputtering process, since the incident argon ion typically undergoes several charge exchange reactions with neutral gas atoms before impacting the cathode surface.¹⁰ Argon atoms can therefore also contribute to a certain degree to the sputter yield. Upon impact, the kinetic energy of the incident particle (in this case, Ar^+) is transferred to the sample (M) through collisional events, and the potential energy of the particle results in electron ejection. The incident argon ion can either be backscattered from the sample surface or will penetrate the sample and transfer its energy to the surface. If the velocity of the impinging ion is greater than 30 eV, material may be sputtered (i.e., ejected) from the sample surface in the form of atoms or molecules in neutral

(M⁰) or ionized (M⁺ or M⁻) states, or electrons may be ejected.⁴ Sputtered particles usually have low energies (few eV) and can be ejected at many possible angles.

Positively charged ions (M⁺) make up about one percent of the total sputtered particle flux and are redeposited back onto the sample surface, depending on the negative cathode potential.¹¹ Negative ions (M⁻) are accelerated away from the cathode surface. The ejected material is made up mainly of neutral sample atoms, which generally possess kinetic energies of approximately 5 – 10 eV.¹² When these sample atoms are ejected, they lose their momentum to elastic collisions with discharge species due to the small mean free paths at the cathode surface (~0.1 mm for pressures of 0.1 – 10 torr). Harrison and Bruhn^{13, 14} have shown that up to 95% of these atoms may be deposited back onto the cathode surface. Some atoms are not re-deposited, and these can either diffuse into the negative glow region, which is essential for atomic emission, or undergo excitation or ionization processes, which is critical for mass spectrometry measurements.

Sputter rate: The amount of sample ejected for a given analysis time is defined as the sputter rate (ng/s) and is given by the Equation 1-1:^{2, 4, 5}

$$q = \frac{\Delta W}{t} \quad (1-1)$$

Where ΔW (ng) is the amount of sample lost due to sputtering and t (s) is the total time of sputtering. The above equation is generally known as the net sputtering rate for glow discharge, because it recognizes that the glow discharge inherently involves re-deposition of sputtered material.^{9, 15}

Multiple parameters affect sputtering rates, including voltage, current and pressure of the discharge. It is possible that the type of fill gas affects sputtering, since the mass of the sputtering agent depends on the fill gas. Sputtering rate can also be altered by the type of sample. Multi-component alloys of the same matrix demonstrate sputtering rates dependent on the

concentration of other minor constituents contained within the sample. Preferably, all elements (and alloys made of the same matrix) would exhibit the same sputtering rates. This is not the case; however, and sputtering rates vary between elements, with the potential to adversely affect calibration curves. The calibration curves can be normalized based on established sputtering rates.¹⁵

Sputter yield: The sputtering efficiency of a sample can also be characterized by calculating sputter yield (atoms/ions), which represents the number of sputtered atoms per incident sputtering atom/ion.^{2, 4} The target atom receives the energy from the incident ion through a transfer in the lattice (sputtered atom). The following is the expression for sputter yield (S):

$$S = \frac{3}{4} \pi^2 \alpha \left(\frac{4m_1 m_2}{(m_1 + m_2)^2} \right) \frac{E}{U_0} \quad (1-2)$$

Where α is the function of the ratio m_2/m_1 and the angle of collision by the incident ion with respect to the sputtering surface.^{16, 17} Energy of the incident ion and the surface binding energy are denoted by E and U_0 , respectively. The sputter yield depends on the relationship between the ion mass (m_1) and the target atom mass (m_2).

As (m_1/m_2) approaches unity, the mass transfer term maximizes, and thus sputter yield increases. An atom's electron concentration in the d-shell orbital is related to sputter yield. In theory, a greater d-shell filling is indicative of a greater sputter yield.^{2, 4, 19} In addition, the penetration depth of primary ions is partially controlled by the electronic structure of the target atoms. An incident ion can penetrate further into a cathode that has a more open electronic structure, which results in less efficient transmission of energy back to the cathode surface and, thus, a reduction in the sputtering process.

Figure 1-6 is a collection of sputter yields for various elements at conditions similar to a glow discharge, 400 eV argon ions.¹⁸ Sputter yield is shown in terms of $S/(1 + \gamma)$, where S is the sputtering coefficient in atoms/ions and γ is the secondary electron coefficient. This is in an overall agreement with the electron density of d-shell electrons. Note that the results in Figure 1-6 are for ion beam, vacuum sputtering and not GD.¹⁸ Sputter yield is affected not only by sputter rate but by the masses of incident ion and sputtered atom, incident ion energy, angle of incidence and the surface binding energy. More neutral atoms are available for ionization if there is a higher sputter yield.

Collisional Reactions in Plasma

Many of the processes within the glow discharge can be accounted for by collisions, and collisions also contribute to the self-sustaining nature of the plasma. There are two broad types of collisions that occur within the glow discharge: elastic and inelastic.¹⁻⁴ The simpler of these two types of collisions are elastic collisions, since kinetic energy is conserved. Energy is not transferred; therefore excitation and ionization processes within the plasma are not usually attributed to these types of collisions.^{2,9} In order for excitation (ionization) to occur, an impinging electron would have to have more energy than that needed to excite (remove) an electron from the atom ground state (excitation /ionization energy). If the electron energy is insufficient, the electron will be deflected from the atom.^{2,9}

The significantly large difference between masses of electrons and atoms leads to a negligible amount of energy transferred during an electron-atom elastic collision, as suggested by the energy transfer function. Even though elastic collisions are unable to cause ionization, they are able to redistribute kinetic energy and help to thermalize the plasma. Inelastic collisions are the other type of collision within the glow discharge plasma and involve energy transfer

between plasma species.^{6, 7, 17, 18} Inelastic collisions are responsible for forming species of analytical interest and for maintaining the self-sustaining nature of the plasma.^{4, 5}

Electron behavior

Within a glow discharge, electrons are accelerated away from the cathode, possibly colliding with gas atoms and causing ionization. However, many of the electrons formed from collisional processes are lost due to recombination.¹⁹ It is also possible for electrons to convey their energy to an atom, raising the internal energy of the atom to an excited state. When this newly excited atom relaxes to a ground state, a photon is released which contributes to the characteristic glow of the discharge. These photons can also be useful for investigating optical characteristics of the discharge.

Electrons are generally accelerated with up to 2000 eV at 2 kV of kinetic energy, which is enough to ionize atoms within the discharge. For example, argon is primarily ionized by collisions with electrons and has ionization energy of 15.76 eV. This process is called electron ionization and is illustrated in Figure 1-4. Mass spectrometry detects doubly charged argon (Ar^{+2}) ions, which have an ionization energy of 27.63 eV. This shows that electron ionization is a key process within the discharge since only electrons have enough energy to form these ions.^{9, 20}

Sputtered species excitation and ionization

Sputtering the surface of a sample with argon ions (and atoms) results in the atomization of a sample in a glow discharge. Atoms that are ejected from the sample surface can diffuse into the negative glow region of the discharge, where they may go through a series of collisions with electrons, meta-stable atoms and other ions. It is these collisions that are responsible for excitation and ionization of the sample material, but for these to be possible in the first place, there must be an inelastic collision between an atom and a particle with kinetic or potential energy. There are multiple excitation and ionization mechanisms that can occur in the negative

glow region; Figure 1-7 lists the three most common of such processes which can take on different roles depending on the operating conditions of the discharge.^{2, 4, 5}

Excitation

In general, thermal electrons in the virtually field-free negative glow region possess low kinetic energy, mainly because of loss of energy due to multiple collisions. The electron energy distribution function (EEDF) can show the abundance of electrons at different energies. It has been shown that thermal electrons will likely result in excitation mechanisms that preferentially involve energy transfer to levels less than or equal to 3-4 eV above ground state.⁸ The atomic transitions that occur in the ultraviolet-visible region are primarily caused by these ground state transitions, and they are wholly responsible for the emission from the negative glow. Glow discharge atomic emission spectrometry (GD-AES) can measure the photons that are released.

Electron impact causing electronic excitations can also be cited as a cause for the population of argon meta-stable atoms. Argon has two long-lived (approximately one millisecond) excited states with energies of 11.55 and 11.72 eV, respectively. A Penning collision²⁰ describes the possibility that collisions between the meta-stable gas atoms and sample atoms could lead to energy transfer and resulting excitation of the sample atom. Figure 1-7 illustrates this process. The negative glow region has a third possible excitation mechanism, known as asymmetric charge exchange.^{21, 22} However, this mechanism has been found by most researchers to be too selective to contribute significantly to excitation processes.²⁰

Ionization

Ionization mechanisms within the negative glow region occur due to the collision mechanisms described previously. Multiple mass spectrometric techniques can detect the ions that are formed through these mechanisms. The goal in atomic mass spectrometry is to produce and detect the maximum possible number of elementally uniform ions.⁴

Electron ionization comprises of a small portion of ionization within the negative glow. The mechanism, as shown in Figure 1-7, is essentially unselective since any atom can be ionized by an electron with sufficient energy. The cross-section curve for electron ionization is similar in shape and magnitude for all elements of the periodic table.^{23,24} However, as mentioned, there are only a few electrons that will have sufficient energy to ionize metals with ionization energies between 5 – 10 eV. It is for this reason that electron ionization likely only makes up a small portion of ionization within a glow discharge.

The dominant ionization mechanism in the glow discharge is known as Penning ionization.^{11, 20, 25-28} Based on its energies, the argon meta-stable atom should be able to sufficiently ionize most elements (with ionization energy smaller than 11.5 eV). Penning ionization is similar to electron ionization in that it is unselective for elements with lower ionization energies than the meta-stable atom energy. It has been shown through elemental quantitative studies that Penning ionization could account for about 50 to 95 percent of sample ionization in the discharge.²⁹ Table 1-1 lists the other possible mechanisms for ionization in addition to electron and penning ionizations.

Figure 1-7 shows that asymmetric charge exchange or charge transfer² could ionize sample atoms in the negative glow region; however, the process is highly selective and controversial and is not considered to be a significant ionization mechanism. The process of asymmetric charge exchange occurs when an electron is transferred from a sputtered atom to an argon ion but is likely only if the difference in energy between the species is small.¹⁷

Modes of Operation

Direct Current

By applying a constant negative potential to the cathode, a direct current glow discharge¹⁹ is operated. Figure 1-8 is a schematic of a direct current (dc) discharge showing the area of

sputtered species in comparison to the glow region. Typical operating conditions of a dc discharge are 1-3 kV and less than 30 mA current.⁹ Owing to the simplicity, reproducibility, cost-effectiveness and steady-state supply of ions produced, this powering mode is the most conventional. There are some disadvantages to the dc discharge, and these include the low operating power (<10 W) and the inability to analyze non-conducting samples.^{3,9}

Pulsed Discharge

Figure 1-8 shows a comparison of ion generation in a dc and pulsed discharge. Sputtering ions are created from the electrical breakdown of argon atoms after a repetitive high voltage pulse is applied to the cathode in pulsed mode and at pulsed initiation. The ions that are created participate in analyte ejection from the cathode surface. Individual pulses create atom packets, which is subjected to ionization. These packets expand and diffuse away from the cathode with each pulse. Temporal profiles are created as a result of the variation in the elemental response in the induction period. The temporal profiles provide discrimination between gas and analyte ions.^{4,5,33-39} Benefits of the pulsed discharge include short term high power operation, enhanced sputter yield, greater excitation and ionization, less sample consumption and temporal resolution.^{9,30-33}

Radio Frequency

Non-conducting samples, such as glass and ceramics, can be analyzed using the radio frequency powering mode. In this mode, an alternating current, applied at high pulse frequencies (1 MHz), induces a self-biasing direct current (dc) potential.^{40,41}

Source Configurations

The glow discharge has a wide array of applications, which has led to the development of multiple source configurations. Each configuration is able to efficiently analyze different sample shapes, collectively making them well-suited for a range of applications. Included in this section

are descriptions of the hollow cathode, diode and Grimm design glow discharge configurations. Each configuration has its own strengths and weaknesses. There is no one configuration that has proved optimum for efficient analysis of all sample types.

Hollow Cathode Geometry

The oldest glow discharge configuration, dating back to the 1930s,³⁴ is the hollow cathode discharge. Hollow cathode sources^{26, 28, 35} are reasonably successful for atomic emission measurements but are rarely implemented for mass spectrometric applications.³⁶ The plasma in a hollow cathode is restricted within a hollow cavity within the sample, forcing sputtering to occur on the sides of the cavity walls. Highly energetic atoms and electrons are trapped within the hollow area, and extended residence times lead to enhanced excitation and ionization of the sample atoms. Due to efficient ionization capabilities, hollow cathode configurations demonstrate detection limits down to the sub-nano-gram range.³⁷ Typically operating conditions for a hollow cathode configuration are voltages between 200-500 V, currents of 10-100 mA and argon pressures between 0.1 – 10 torr.³⁸

Figure 1-9 shows an early design of a hollow cathode configuration designed exclusively for mass spectrometry, because of the high population of ions that can be formed within the cavity. The figure also illustrates the confined nature of a hollow cathode plasma, which provides an improved population of sample atoms and ions, which must then be extracted from the hollow well and transported to the sampling region, additional steps that can prove complex. Even with the potentially complex and numerous steps involved the potential advantages for hollow cathode mass spectrometry studies, which include enhanced detection limits, provide justification for developing methods to avoid these concerns.

Diode (Coaxial) Geometry

Diode geometry is the most popular glow discharge configuration for mass spectrometry. It is not typically used for atomic emission, however.^{39, 40} This design is usually called a “pin-type” source and is used to analyze sample types that can be mounted on the end of a direct insertion probe (DIP). Figure 1-10 illustrates how the probe and sample assembly are introduced into the glow discharge chamber through a vacuum interlock. The discharge then forms on the end of the sample and ions are extracted from the negative glow region of the plasma. Diode geometries generally employ conditions of 500 – 1000 V, 1 – 5 mA and 0.4 – 2.0 torr Ar pressures.³⁸ In this configuration, the sample serves as the cathode, and the surrounding discharge chamber becomes the grounded anode. There are some limitations to this geometry including problems with sample placement, thermal effects and re-deposition on source components. Glow discharge applications that require layer analysis, such as depth profiling, are difficult using this configuration.

Grimm Geometry

The Grimm-type configuration is widely used for atomic emission measurements and is gaining popularity for mass spectrometry applications. The Grimm-type configuration makes use of flat cathode geometry and was introduced by Grimm as an atomic emission source in the late 1960s.³⁵ In this configuration, the sample is pressed against an O-ring on the flat cathode plate, ensuring adequate sealing and proper vacuum conditions, shown in Figure 1-11. Utilizing a constricted plasma, the discharge is laterally restricted to the sample surface and confined to the size of the surrounding anode. Maintaining a distance between the anode tip and sample that is smaller than the mean free path of the electrons allows the restriction of the plasma to the sample surface.⁴¹ The plasma is also confined in circumference by the cylindrical anode, allowing planar sputtering of the sample. Typical operating conditions of the Grimm-type source are approximately 500-1500V, 3 – 20 mA and 2 – 6 torr argon pressure.³⁸

The Grimm-type source provides a significant advantage over other source configurations due to the easy sample interchange.⁴²⁻⁴⁵ There can be quick sample turn-around time and precise sample placement because samples are mounted externally. There are also no sample positioning concerns.^{35, 46} The Grimm configuration also has the ability to obtain surface and in-depth analysis by properly controlling the discharge parameters to obtain planar sputtering^{15, 42, 47} and can also analyze thin sample layers with pulsed operation.^{15, 42, 44, 48, 49}

The concerns for using the Grimm-type configuration include the analysis of flat samples, since a flat smooth sample surface is required to guarantee adequate sealing, and any other sample shapes with smaller diameters than the anode diameter are less adaptable for analysis. For mass spectrometric applications, ion transport is also a limitation of the Grimm configuration.

Table 1-1. Ionization processes in a glow discharge plasma. Ionization is characterized by primary and secondary ionization processes.

I. Primary Ionization Processes

1. $M^0 + e^- \rightarrow M^+ + 2e^-$
2. $M^0 + Ar^* \rightarrow M^+ + Ar^0 + e^-$

II. Secondary Ionization Processes

1. $M^0 + Ar^+ \rightarrow M^+ + Ar^0$
 $MX + Ar^+ \rightarrow M^+ + X + Ar^0$
 2. $Ar^* + M^0 \rightarrow ArM^+ + e^-$
 3. $M^* + h\nu \rightarrow M^+ + e^-$
 4. $M^0 + e^- \rightarrow M^* + e^- \rightarrow M^+ + 2e^-$
-

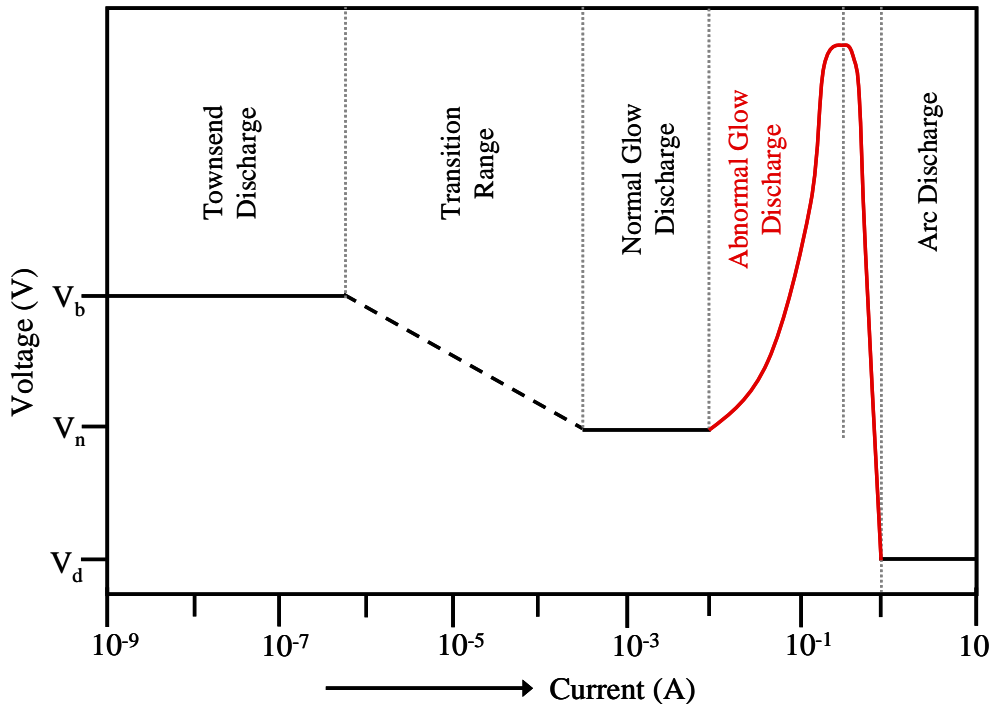


Figure 1-1. Diagram of voltage vs. current regimes for various discharges. [Reprinted with permission from E. P. Hastings, Reactive gases in glow discharge ion sources: sputtering and ionization considerations. Ph.D. dissertation, University of Florida, Gainesville, Florida, 2004.]

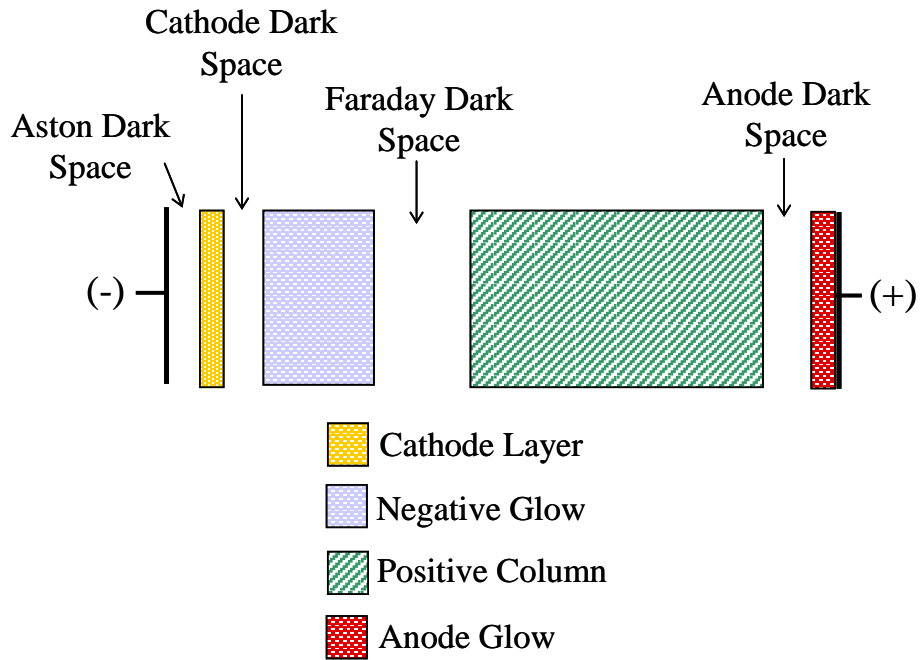


Figure 1-2. Various regions of a glow discharge. The three main regions are the cathode dark space (CDS), negative glow (NG) and Faraday dark space. [Reprinted with permission from E. P. Hastings, Reactive gases in glow discharge ion sources: sputtering and ionization considerations. Ph.D. dissertation, University of Florida, Gainesville, Florida, 2004.]

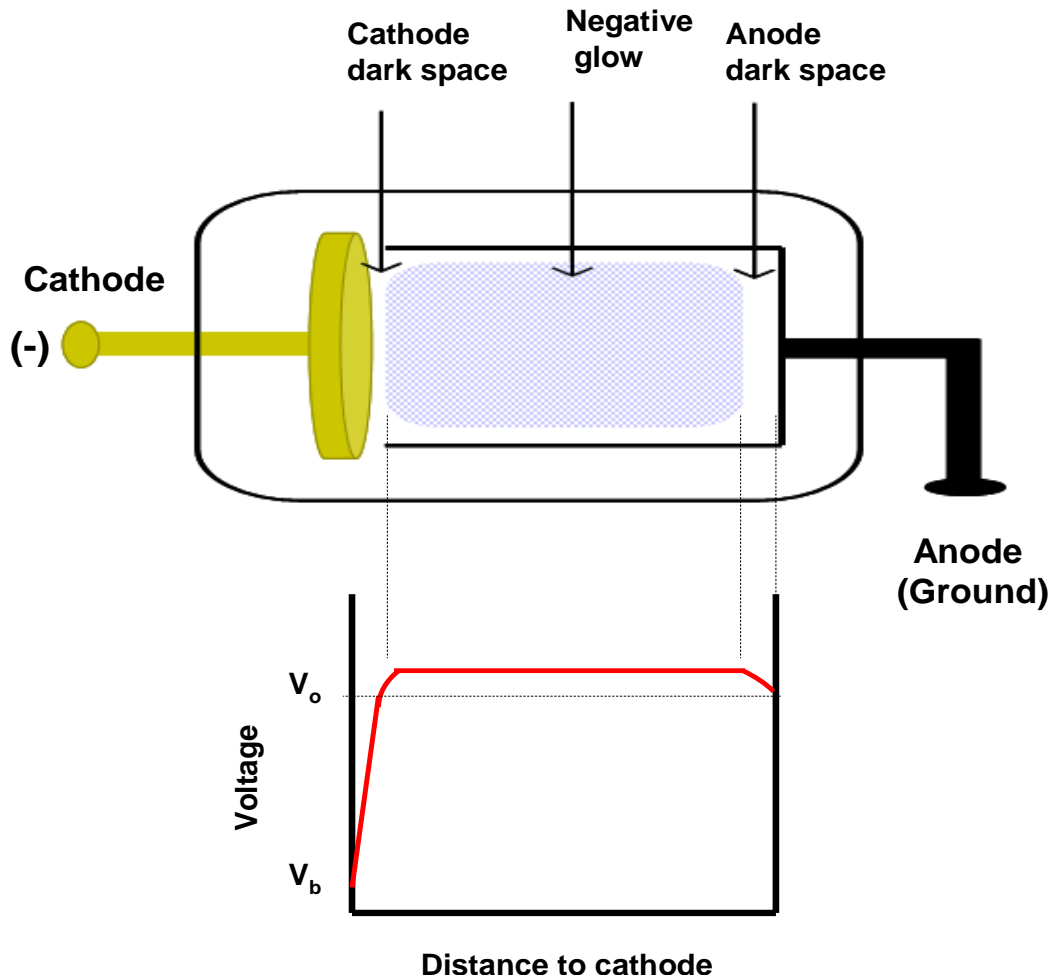


Figure 1-3. The three main regions in a simple glow discharge vs. voltage distribution as a function of distance to cathode. [Adapted from E. S. Oxley, The microsecond pulsed glow discharge: developments in time-of-flight mass spectrometry and atomic emission spectrometry. Ph.D. dissertation, University of Florida, Gainesville, Florida, 2002]

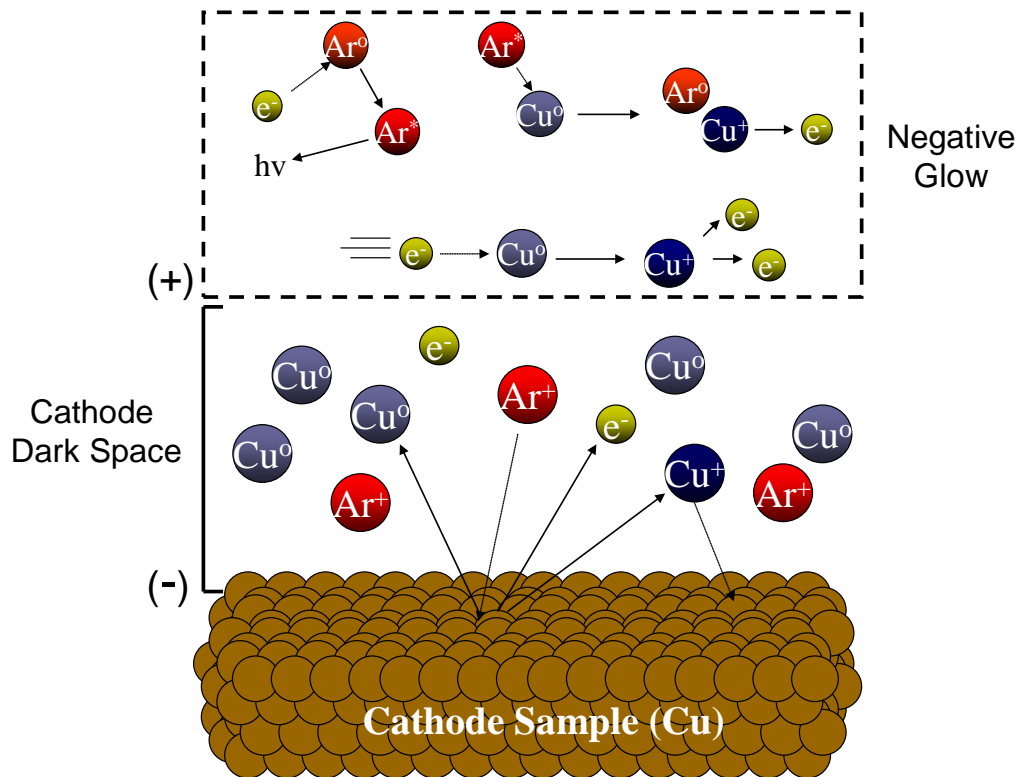


Figure 1-4. Major events in the glow discharge: Cathode sputtering and ionization- excitation in the negative glow. [Reprinted with permission from E. S. Oxley, The microsecond pulsed glow discharge: developments in time-of-flight mass spectrometry and atomic emission spectrometry. Ph.D. dissertation, University of Florida, Gainesville, Florida, 2002]

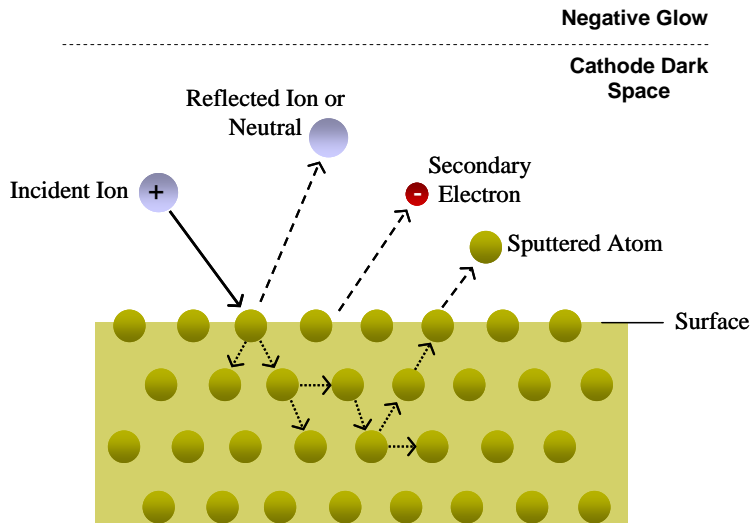


Figure 1-5. Cathode sputtering due to fast ion/fast atom impact. [Adapted from E. P. Hastings, Reactive gases in glow discharge ion sources: sputtering and ionization considerations. Ph.D. dissertation, University of Florida, Gainesville, Florida, 2004.]

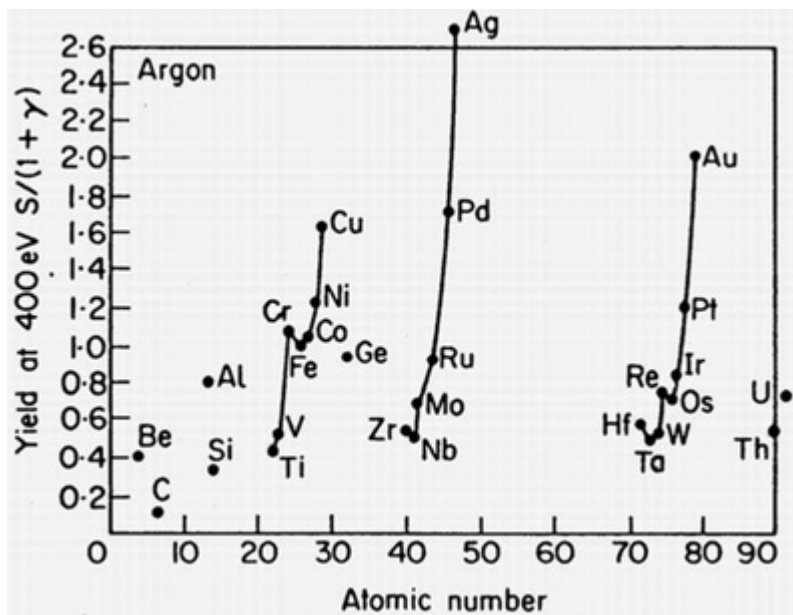


Figure 1-6. Sputter yield for various elements in the periodic table. The elements are bombarded with 400 eV argon ions. (From N. Laegreid *et. al.*¹⁸)

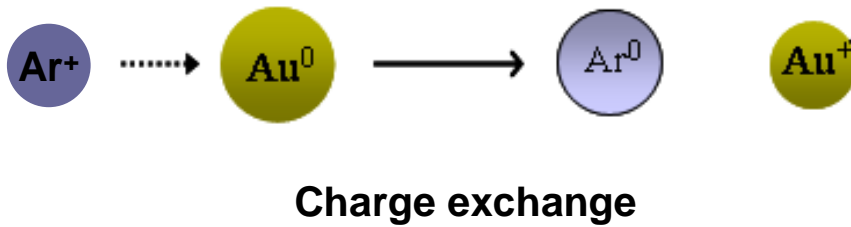
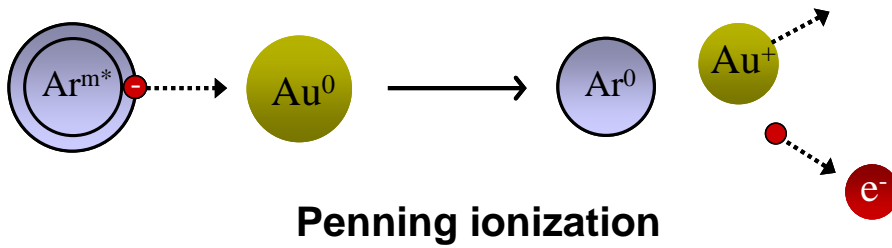
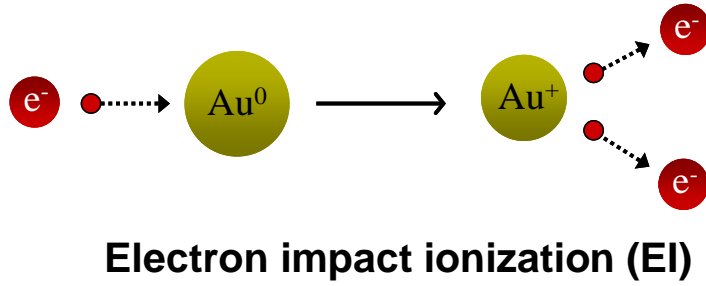


Figure 1-7. The most common types of interaction in the plasma. [Adapted from E. S. Oxley, The microsecond pulsed glow discharge: developments in time-of-flight mass spectrometry and atomic emission spectrometry. Ph.D. dissertation, University of Florida, Gainesville, Florida, 2002]

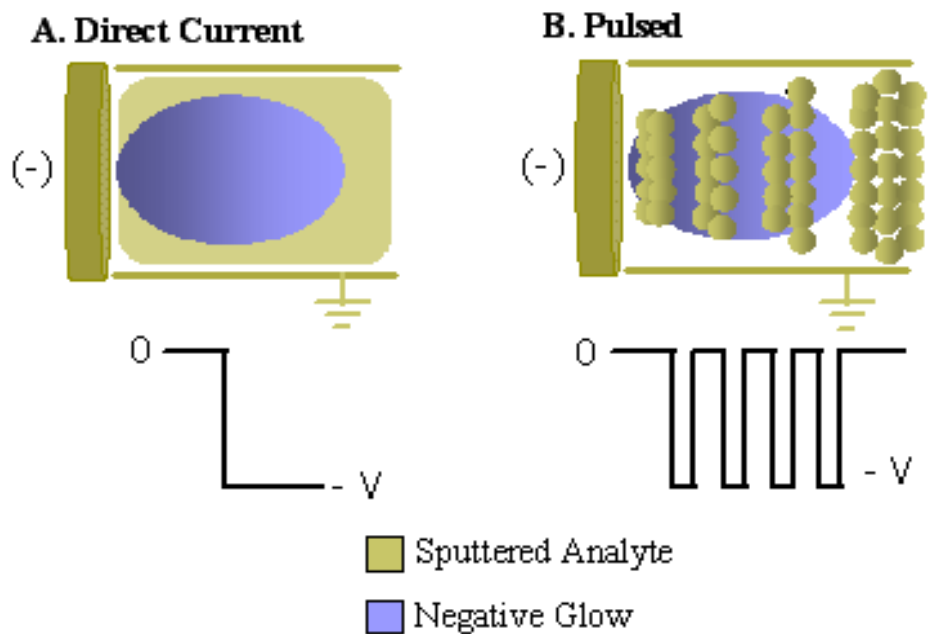


Figure 1-8. Direct and pulsed glow discharge modes are compared. [Reprinted with permission from E. S. Oxley, The microsecond pulsed glow discharge: developments in time-of-flight mass spectrometry and atomic emission spectrometry. Ph.D. dissertation, University of Florida, Gainesville, Florida, 2002]

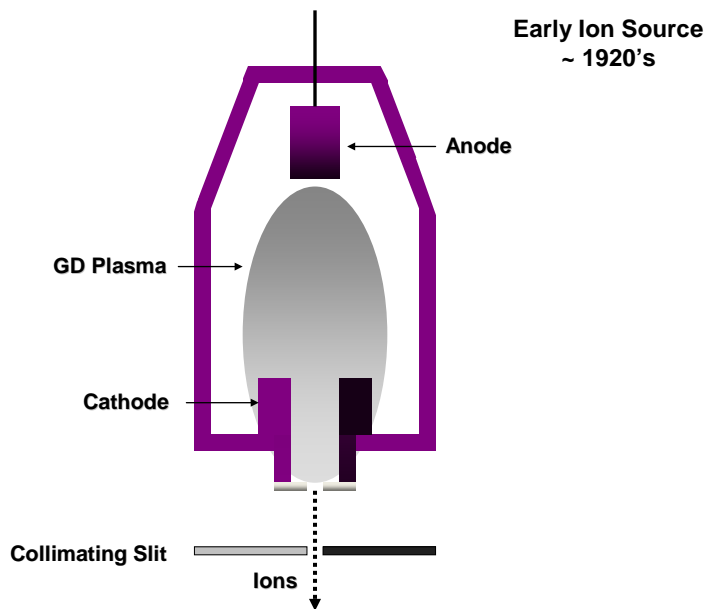


Figure 1-9. Hollow cathode glow discharge source for mass spectrometry. [Courtesy of Dr. W. W. Harrison, University of Florida, Gainesville, Florida]

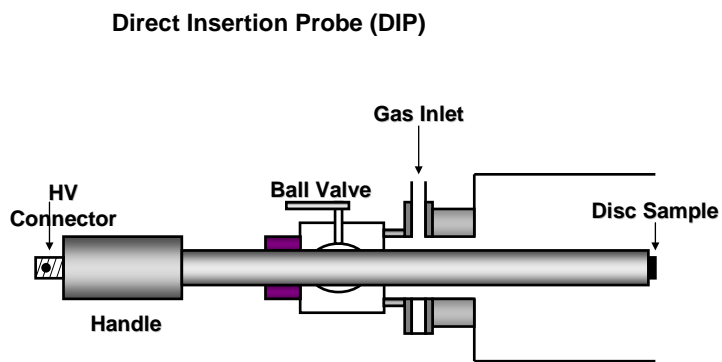


Figure 1-10. Diode geometry with a direct insertion probe (DIP). [Courtesy of Dr. W. W. Harrison, University of Florida, Gainesville, Florida]

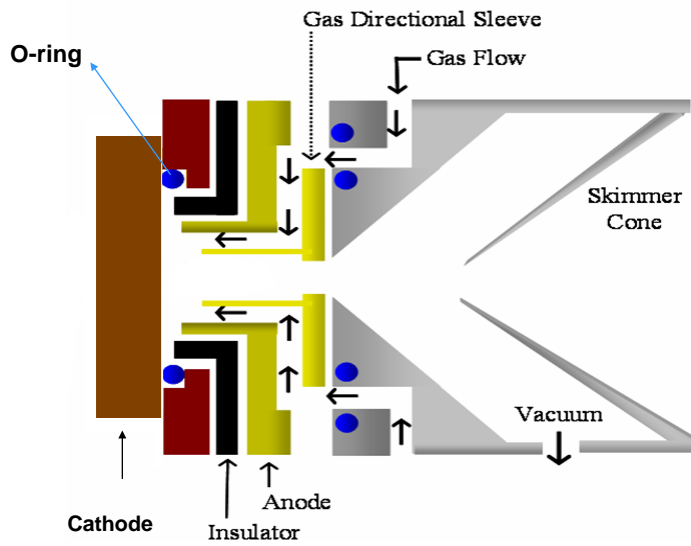


Figure 1-11. Grimm glow discharge geometry for mass spectrometry. [Reprinted with permission from E. S. Oxley, The microsecond pulsed glow discharge: developments in time-of-flight mass spectrometry and atomic emission spectrometry. Ph.D. dissertation, University of Florida, Gainesville, Florida, 2002]

CHAPTER 2 EXPERIMENTAL DETAILS AND BACKGROUND

Introduction

The experimental part of this research is consist of three major components:

- Aerosols: generation and sizing
- Pulsed glow discharge ion source
- Time-of-flight mass spectrometer

In all future chapters, there will be a publication-style experimental section, which briefly discusses the set up and material used for this work. In this chapter, more details and background related to these experiments is provided.

Aerosols

Two methods for aerosol generation have been utilized in our research. The first method is simply based on nebulization of salt solution by an ultrasonic nebulizer. In the work discussed in Chapters 3 and 4 the salt particles generated by this method were used as a source of aerosol. The other method of particle generation is laser ablation of solid samples. Laser ablation of solid samples is a well known technique used in tandem with ICP mass spectrometry. In this chapter particle generation by the ultrasonic nebulizer will be discussed. The information about laser ablation is discussed in Chapter 5.

Aerosol Generation

An ultrasonic nebulizer-dehydrator^{57, 58} was used to generate a flow of dry particles from their corresponding salt solutions. Figure 2-1 shows the schematics of the nebulizer-dehydrator. A peristaltic pump directs the flow of aqueous salt solution onto the surface of a piezoelectric in the nebulizer unit, vibrating at a frequency of about 1 MHz.⁵⁰ About 10% of the solution is converted to a wet aerosol, and a mist is formed. The resulting wet droplets are carried by the argon flow into glass tubing heated to 150°C. Part of the moisture from these wet particles is

evaporated, and a stream of relatively dry particles and water vapor is formed. This stream then goes through a cooling chamber (4°C) to condense the water vapor. The aerosol then goes through a porous tube (made of a special polymer) in the dehydrator unit. A stream of argon heated to 150°C moving in the opposite direction of the aerosol outside the porous tube will completely remove any trace of water vapor from the aerosol. The output of the dehydrator unit is a stream of dry salt particles in argon. In order to verify the necessity of the dehydrator, the nebulizer was directly connected to the glow discharge; it was observed that no plasma was formed due to presence of water vapor. In contrast, when both nebulizer and dehydrator units are used, the discharge plasma can be ignited and remains stable.

Nebulizer-Dehydrator Efficiency

The easiest way to estimate the efficiency of our nebulizer-dehydrator unit is to collect and measure the weight of solutions exiting the waste tubes of the nebulizer. There are three solution collection tubes in the nebulizer unit. The first one (W1) is located at the nebulization chamber, which collects that part of the solution that is not nebulized at all. The second tube (W2) collects the solution formed at the beginning of the heating chamber. This solution is formed by water vapor that is condensed at the end of the heating chamber. The last tube (W3) collects the condensed vapor from the cooling chamber of the nebulizer. Three samples of 4 mM CsI in water with a total solution mass of ~25-30 g were nebulized. The resulting solutions were carefully collected and weighed at the end of all three waste exit ports. Table 2-1 shows the mass and weight percentage of these experiments. It is important to note that the summation of water weight collected at the three waste tubes does not add up to 100%. This is due to loss of water left in the nebulizer and tubing itself. The conductivity of collected solutions was measured to be 94.3 $\mu\text{S}\cdot\text{cm}^{-1}$, 2.76 $\mu\text{S}\cdot\text{cm}^{-1}$, and 1.66 $\mu\text{S}\cdot\text{cm}^{-1}$ for W1, W2, and W3, respectively (S stands for

Siemens). This shows that W1 is mainly un-nebulized solution, while W2 and W3 mostly contain the condensed water resulting from drying the wet particles. This experiment shows that ~10% (W2 + W3) of solution is nebulized. This is the maximum possible yield, as some of the water exiting W2 and W3 can simply be the result of vaporization of water from the nebulization chamber and not from the aerosols.

One should also consider the potential for loss of aerosol during the transfer process through different dehydrator and external tubings to the glow discharge source. The overall efficiency of the nebulizer-dehydrator could even be less than the 10% measured by the above procedure. In order to obtain a more accurate aerosol transfer efficiency to the discharge, another experiment was designed: the outlet of the dehydrator was transferred by Teflon tubing (same length used for aerosol transfer into glow discharge) under 250.0 mL of water. After nebulizing a 4 mM solution of CsI for ~5 minutes, the conductivity of water was measured. After comparing this conductivity with the calibration graph (Appendix Figure A-8) that was prepared separately, one can estimate the concentration of CsI in the aerosol collection solution. From this concentration, the mass of salt transferred as aerosol and efficiency of the nebulizer can be calculated. Table 2-2 shows the results of three such experiments, and the efficiency of the nebulizer-dehydrator unit was found to be ~ 4%. The expected efficiency for such a nebulizer is about 10%.⁵¹ Efficiencies as high as 25% for certain experimental conditions, with optimized nebulizing power and liquid flow rate have been reported.⁵² Our measured efficiency is much lower than the reported values. This might be due to the fact that we are nebulizing solutions of much higher concentration compared to the normal range of concentrations used for ICP experiments in these nebulizers.

Particle Size Distribution Measurements

In order to study the particle interaction with the glow discharge plasma, one must consider the size of particles present in the aerosol. In order to measure the size distribution of particles in our aerosol, at first an attempt was made using a differential mobility analyzer (DMA). However, due to high concentration of salt in our nebulizer intake and also insufficient pumping, the size measurement experiment did not result in any meaningful results. Another problem was splitting the particle flow in order to protect the instrument from contamination by a large amount of particles. Finally, an aerodynamic particle sizer (Chapter 3) was used to measure the particle size distribution. This instrument measures the particle sizes based on their time of flight. This method is an example of light interaction methods of particle size measurements. In this instrument, particles pass through a path crossed by two laser beams. The scattering of laser light is detected and used to measure the velocity of particles, which can be related to particle diameter. Here we discuss the general categories of particle sizing techniques used in the literature.⁶¹⁻⁶⁵

Microscopy method

In this method, the particles are collected on the proper microscope stage. The resulting collection of particles is then placed under the microscope (or microscopic probe/tip) for observation. The resulting image will show the shape and diameter of each individual particle collected on the collection surface. This method is accurate, but is time consuming and requires the collection of particles from the aerosol state to the surface. Optical microscopy, transmission electron microscopy (TEM), scanning electron microscopy (SEM), and atomic force microscopy (AFM) are examples within this category.⁵³

Particle impaction method

In this classic method, a series of impaction plates are placed at the path of particles. The aerosols are accelerated through jet nozzles towards the plates (Figure 2-2).^{62, 63} Each impactor will trap a group of particles within a specific size range. At the end, weighing or chemical methods can be used to estimate the overall volume / mass of particles in that size range.^{64, 65, 68}

Light interaction method

In these methods, the interaction of light (usually in the form of a laser beam) with particles is used to measure particle size in the gas phase.^{53, 54} Laser diffraction, single particle light scattering,⁵⁴ multi-angle light scattering, time-of-flight, and laser doppler velocimetry are examples of light interaction methods of particle size measurement.⁵⁵ For example, the light scattering technique uses the Mie Theory.⁵³ According to Mie Theory,⁵³ the light scattered by an individual particle is a function of the scattering pattern produced by spherical particles of a specific size. The scattered light intensity is a function of the angle, wavelength, particle size and optical properties of the system, such as refraction index of the particles. Therefore, collecting and analyzing the pattern of scattered light at different angles along with complicated calculations can result in particle size distribution of the aerosol sample.

Electrical property method

In this method, usually particles are charged and then the charged particles will have different physical properties due to their size.⁵⁶ The differential mobility analyzer^{61, 64, 65} (DMA) is an instrument that works based on such properties. In this method, particles are charged before they go through a chamber under the electric field of a central rod (Figure 2-3). The intensity of attraction that particles have to this rod depends on their mobility, which also depends on particle size and shape. This is assuming the fact that all particles have the same charge (more likely single charges). By scanning the electric field, only particles of a size within a certain range can

pass through the chamber. A condensation particles counter⁵⁶ (CPC) unit is used in series after the output of DMA (Figure 2-4). The particles are first exposed to vapor of a liquid such as butyl alcohol to enlarge the size of particles by condensation. Then a light scattering system is used for counting the particles in CPC.⁵⁶

Sedimentation method

This category includes measurement techniques such as photo, centrifugal and X-ray sedimentation.^{53, 57} Fluorescence Activated Cell Sorting (FACS) and Field Flow Fractionation (FFF) are also within this category.⁵⁵ As the meaning of the word sediment expresses, this method is based on the rate in which the particles precipitate (usually in a liquid). For example, in X-ray sedimentation, a horizontally collimated beam of X-rays passes through a liquid. Then the precipitation of particles will affect the beam intensity, and as a result, the number of particles is measured. The larger particles will cross the beam first and the smaller particles will precipitate later.

Limitations of Particle Sizing Methods

It is important to understand that a specific particle sizing device can not measure the particle size directly, but rather measures a physical property that is related to particle size / diameter.⁵⁸ For example, the result of a DMA-CPC particle sizing experiment is indeed the mobility diameter of particles (d_m), or a particle impactor works based on aerodynamic properties and the result is aerodynamic diameter (d_a). Another important point is that real particles are not always perfectly shaped spheres; in some cases, they are irregularly shaped or agglomerated.⁵⁹

Agglomeration can result in false data about particle size distributions. This means that the measured diameter does not represent the diameter of a particle that has an equal volume to that of the real particle ($d_{ve} \neq$ measured diameter).⁵⁹ For example, irregularities from spherical shape

will result in reduction of aerodynamic diameter. As a result, a 200 nm agglomerate can have the same trajectory that a 40 nm spherical particle has. In contrast, in a DMA experiment, an agglomerated or irregular particle will have a lower mobility. In other words, the irregularly shaped particle will behave like a larger particle in a DMA system and will exit the analyzer in conditions similar to that of larger particles.⁵⁹ Consequently, the impaction and DMA will result in falsely low and falsely high results, respectively (Figure 2-5).

Presentation of Particle Size Measurement Results

The result of most particle size measurements is a graph in which the population of particles (absolute or relative) is plotted vs. particle size. However, the population is usually found for a certain range of diameters. For example, N% (relative abundance) or N (absolute abundance) will have a constant value in a size range and then another value in the next diameter range.^{60, 61} Unfortunately, since the diameter bins are not equally distributed, this method can be misleading.⁶⁰ For example, let us assume 20% of particles are within the range of 300-500 nm, while only 10% are within the range of 10-30 nm. If we assume an equal distribution within each range, one might think that a particle in the first range is more abundant than a particle in the second one. This would be correct if both ranges had equal width (20 nm vs. 200 nm). A closer look will show that the 20% of the particles must be distributed among many sizes (from 300 to 500 nm) while the second range only covers 20 nm. In order to avoid such biases, we can normalize the abundance by the related range. Dividing the abundance by the size range width (20% / 200 nm for example) will result in more realistic values of abundance. This way we can see that a 20 nm particle is likely to be 5 times more abundant than a 400 nm particle. (0.5 vs. 0.1 as shown in equations 2-1 and 2-2)

$$\frac{10\%}{20nm} = 0.5 / nm \quad (2-1)$$

$$\frac{20\%}{200nm} = 0.1/nm \quad (2-2)$$

This way of presentation of particle size is normally referred to as dN/dD , where N is the number of particles per unit volume and D is the diameter range.^{60, 61} If particle size is presented in micrometers and number density of particles is in number of particles per cubic centimeter, then the Y axis is labeled with dN/dD and units of $cm^{-3}.\mu m^{-1}$.

Although particle abundance in each size range provides some information, it does not necessarily provide the useful physical information such as their contribution in ion signal after they enter the plasma. For example, here if the number of 20 nm particles is 5 times of that of 400 nm particles, one might misguidedly think that the 20 nm particles will contribute to the signal of our glow discharge 5 times more than that of 400 nm particles. This is correct if we ignore the obvious fact that the diameter of 400 nm particles is 20 times of the diameter of 20 nm particles. Considering this and the cubic relation of volume and mass with diameter, the signal provided by a single 400 nm particle is 8000 times larger than a single 20 nm particle.

Considering the factor of 5 for abundance of 20 nm particles, the 400 nm particles will have an advantage by factor of 1600. The importance of the role of particle volume leads to another method of presentation of particle size. The dV/dD represents the total volume of particles per unit volume of air (or gas) that are within a specific size range and are normalized by that size range.^{60, 61} The unit of this value is $\mu m^3.cm^{-3}.\mu m^{-1}$. If the absolute abundances are not available and relative volume intensity in each range is available, then it will be shown as $(dV\%/dD)$ and the unit will simply be μm^{-1} .

If the surface of the particle is the physical property of interest (i.e. surface chemistry and catalysis applications) then one can present the dS/dD which deals with the surface instead of the volume.^{60, 61}

Finally, when analyzing different aerosols, it is not always easy to reach a quantitative conclusion by just looking at the size distribution plots. They can look very similar, while indeed they represent different aerosols. The volume mean diameter (D_V) is a quantity that is defined as the diameter of a particle, whose volume is equal to the average volume of all particles present in the aerosol.^{60, 61} One can define the surface area mean diameter in a similar way.

Glow Discharge Source

The glow discharge source used in this experiment was modified from the original design used by Harrison group for depth profiling. The details of this geometrical modification are well explained in Chapter 3.

Mass Spectrometer

The mass spectrometer is a time-of-flight instrument (Renaissance, LECO Corp., St. Joseph, MI) that was modified for our application. Table 2-3 shows the typical instrument parameters used during experimentation. These parameters are very similar to those previously used by Harrison Group⁹ with a Grimm glow discharge source. The primary difference was the use of ion deflection at 1.346 μs to deflect the excess of argon ions, which was required since in the new source geometry, the argon flow was much higher (800 ml/min compared to 150 ml/min). Because the argon signal was saturating the detector, deflection of argon ions was used to diminish it. It was also observed that increasing repeller delay time from 1.2 μs to 2.0 μs increased the particle ionization signal. An important point of note is that values of less than 16 μs for repeller delay time are experimentally meaningless. This was discovered by carefully

investigating the repeller ringing on the oscilloscope; when delay times shorter than 16 μs are selected on the software, the real delay time remains at 16 μs and does not go below this value. More details about repeller-modulator delay times follow in this chapter.

Modifications

Original ICP TOF-MS: The time-of-flight mass spectrometer was originally equipped with an ICP ion source. The red line in Figure 2-6 shows a constant supply of ions provided by the ICP plasma. Since the TOF detector requires a gated ion source, the modulator gates this continuous ion source. The modulator (yellow) is a cylindrical part that normally has a positive potential (100V) to prevent ions from entering the flight region. However, for a short time it is pulsed to a negative potential to let ions pass in a gated way. Its delay time is 45.11 μs and its negative pulse duration is 4.89 μs . It allows for a packet of ions of $\sim 1.5\text{cm}$ in length to pass. Modulation delay is the timing between opening the gate and the end of the last modulator pulse. Addition of the modulator delay to its width results in 50 μs timing between the start of two consecutive pulses. As a result, the factory-made ICP-MS works at 20,000 Hz (As reported in the instrument manual).

The repeller is adjacent to the modulator, and it provides a high positive voltage (1000V) to shoot the ions into the flight tube. The repeller was set to have a pulse width of 1.0 μs (in the ICP mode) and the instrument's manual does not clarify the delay time between modulator and repeller. It is predicted that there will be a very short delay time right after the modulator, and that they will work in tandem with each other to gate ions. One thing that is clear, however, is that the role of the repeller here is not gating, but to shoot a packet of ions (partially or completely) into the flight tube, right after the modulator.

Modified GD-MS source: The LECO instrument has been modified for use with a pulsed Grimm-type glow discharge source for ionization. The supply of ions is no longer continuous, but pulsed. According to Eric Oxley's dissertation, the modification includes some structural specifications for replacement of the old ICP with a homemade GD source, as well as some software modifications.

Without these changes, the software may not have accepted the microsecond pulses from the GD source. A repeller delay time adjustment also needed to be made to span a range of 10 μ s to 300 μ s, allowing ion extraction time to be variable so that temporal resolution measurements could be achieved.^{4,33} A complementary software (Alternate timing) we added to allow the switch between ICP and GD modes. The ICP mode of detection (20,000 Hz) for the instrument is still available when the corresponding box is not selected on the software. In all experiments discussed, the only variable delay time is referred to as repeller delay time. Figure 2-7 shows the timing diagram for the HV ionization pulse in the source with respect to the modulator and repeller pulses. The schematics of ion extraction are also shown in Figure 2-8. The exact meaning of the repeller delay used previously was not discussed. In other words, it was not clear that this is the delay from the start of the HV pulse or the end of it, and is it the delay to the repeller or modulator. It was neither understandable what the exact timing between modulator and repeller is.

Repeller Modulator Timing

Since the timing between the external trigger (which initiates the glow discharge pulse) and the repeller-modulator pulses was not clear this was carefully studied by looking at the ringing of the repeller and modulator on an oscilloscope. Figure 2-9 shows the timing diagram for different pulses of glow discharge and mass spectrometer. The time-of-flight mass

spectrometer sends an external trigger (green) to the pulsed high voltage generator ($t = 0$), and a high voltage (HV) pulse (black) is then applied to the glow discharge source with a pulse width determined by the HV pulse generator. The repeller of the time-of-flight will always have its high voltage pulse (red) start according to the repeller delay time value from the software.

The modulator is synchronized with the repeller in a unique way and works as follows: the trailing edge of the modulator is always $1\ \mu\text{s}$ after the leading edge of the repeller. This means any change in the width of the modulator pulse will change the location of its leading edge with respect to $t = 0$, but not its trailing edge. The arrows on the pulse widths in Figure 2-9 indicate which edge of the pulse will move with respect to $t = 0$ as a result of the change in pulse width.

For example, Figure 2.10, A shows a $10\ \mu\text{s}$ high voltage pulse applied to the source. The repeller delay time is $60\ \mu\text{s}$, and the modulator and repeller pulse widths are $5\ \mu\text{s}$ and $1.2\ \mu\text{s}$, respectively. In 2-10 B, the modulator and repeller pulse widths are increased to $20\ \mu\text{s}$ and $10\ \mu\text{s}$, respectively. In C, the repeller delay time is reduced from $60\ \mu\text{s}$ to $40\ \mu\text{s}$. It is important to note that the modulator is physically located a few centimeters behind the repeller, otherwise such timing would not be logical. E shows the source producing a $30\ \mu\text{s}$ package of ions which will move through the skimmer and ion lenses toward the modulator-repeller. It will take about $20\ \mu\text{s}$ for this package to arrive at the modulator. Since the delay time is set at $40\ \mu\text{s}$, the modulator gate will allow a $5\ \mu\text{s}$ package of ions to pass (from $t = 36\ \mu\text{s}$ to $t = 41\ \mu\text{s}$). However, considering a $2\ \mu\text{s}$ flight time from the modulator to repeller, this package will arrive at the repeller from $t = 38\ \mu\text{s}$ to $t = 43\ \mu\text{s}$. The repeller will then choose a smaller portion of this package (from $40\ \mu\text{s}$ to $41.2\ \mu\text{s}$) and accelerate it towards the flight tube. If the repeller width is increased to $2\ \mu\text{s}$ a larger package of ions and a larger signal is expected, which is in agreement with experimental results.

Increasing the repeller pulse width beyond 2 μs does not increase the signal any more, as expected.

Another interesting observation is that repeller delay times of less than 16 μs on the instrument software are all shown to equal 16 μs . This must be due to some electronic oversight in design when modifications were done for pulsed timing. In order to reach shorter delay times, one can place an external delay generator before the HV pulse (Figure 2-10 F). Appendix Figure A-4 shows the repeller-modulator ringing, along with argon signals, collected on the oscilloscope.

TOF-MS Detector and Collecting Mass Spectrum

The detector of the mass spectrometer is a discrete dynode active film multiplier that produces electrons when ions strike it. To acquire and generate a full mass spectrum, the mass spectrometer divides the whole mass range into 10 sections. Then it goes through and integrates for a certain period at low masses (from 0-30 amu), moving to the next window (30-60 amu), and so on. Considering the older technology of the 1990s, taking a full spectrum can take 30-40 seconds (depending on integration time). A sample peak from a typical mass spectrum collected by the software is depicted in Figure 2-11. An SMA to BNC converter was used to connect an oscilloscope to the detector's signal output on the instrument control module (ICM) of the mass spectrometer. The modulator-repeller ringing was used to trigger the oscilloscope. In order to obtain a stable signal, it is very important that the trigger main level be at 77 mV. Connecting the detector signal directly to an external oscilloscope results in a mass spectrum with much less noise (Figure 2-12). The oscilloscope also makes possible the collection of the whole spectrum, and saving it as a spreadsheet (file.csv) on a computer, in just a few seconds.

All mass spectrometry signals in this dissertation refer to positive ion signals. If a specific isotope is not specified, the signal is for the most abundant isotope of that element. For example, copper, argon, cesium and iron signals refer to $^{63}\text{Cu}^+$, $^{40}\text{Ar}^+$, $^{133}\text{Cs}^+$ and $^{56}\text{Fe}^+$ ion signals, respectively.

Table 2-1. Results of efficiency measurements for ultrasonic nebulizer dehydrator. An average efficiency of 10.9 ± 2.0 resulted (95% confidence interval).

	Trial 1		Trial 2		Trial 3	
	Mass / g	Mass %	Mass / g	Mass %	Mass / g	Mass %
Total feed	26.5717	100	29.2761	100	28.2120	100
W1	22.6236	85.14171	25.5053	87.12	23.7122	84.05
W2	2.0286	7.634438	2.1430	7.32	2.4347	8.63
W3	0.7996	3.009217	0.8549	2.92	0.8859	3.14
Total		95.78537		97.36		95.82
W2 + W3		10.64365		10.24		11.77

Table 2-2. Results of nebulizer-dehydrator efficiency using conductivity measurements. The average efficiency was found to be 4.5 ± 0.6 (95% confidence interval). A 4 mM CsI solution was used for both nebulization and conductivity calibration graph. The conductivity values were compared to the calibration graph (Appendix A, Figure 8) and the volumes of CsI solution found from the graph were multiplied by 2.5 (250 mL volume of collector vs. 100 mL for calibration graph). The result is the volume 4 mM of CsI that would lead to the same conductivity as the particles transferred to the collecting solution. Comparing this equivalent volume with the original volume of nebulized solution will result in the efficiency of the nebulizer-dehydrator system.

	Trial 1	Trial 2	Trial 3
Volume of CsI nebulized / mL	5.97	5.74	7.08
Conductivity of 250 mL collector / $\mu\text{S}\cdot\text{cm}^{-1}$	1.02	0.93	1.12
Equivalent volume of CsI transferred / μL	282.5	246.4	322.7
Efficiency %	4.73	4.29	4.56

Table 2-3. Typical operating conditions for time-of-flight mass spectrometer.

Ion Lens 1	-500 V
Ion Lens 2	-550 V
Flight Tube	-1490 V
Detector	-1600 V
Reflectron Low	215 V
Reflectron High	1536 V
Noise Reduction	500 V
Deflection Time 1 (start/width)	0.986 μ s / 0.05 μ s
Deflection Time 2 (start/width)	1.346 μ s / 0.150 μ s
Deflection Pulse	-400 V
X-Steering	-1473 V
Y-Steering	-1630 V
Einzel Lens 1	-1370 V
Einzel Lens 2	-799 V
Modulation Positive	120 V
Modulation Negative	-133 V
Modulation Delay	40 μ s
Modulation Pulse Width	5 μ s
Repeller Bias	-4 V
Repeller Pulse	1000 V
Repeller Pulse Width	1.2 - 2.0 μ s
Repeller Delay Time	15 - 300 μ s
Alternate Frequency	400 Hz
Third Stage Pressure	0.4 – 1.2 μ torr
Integration Time	500 ms – 2 s

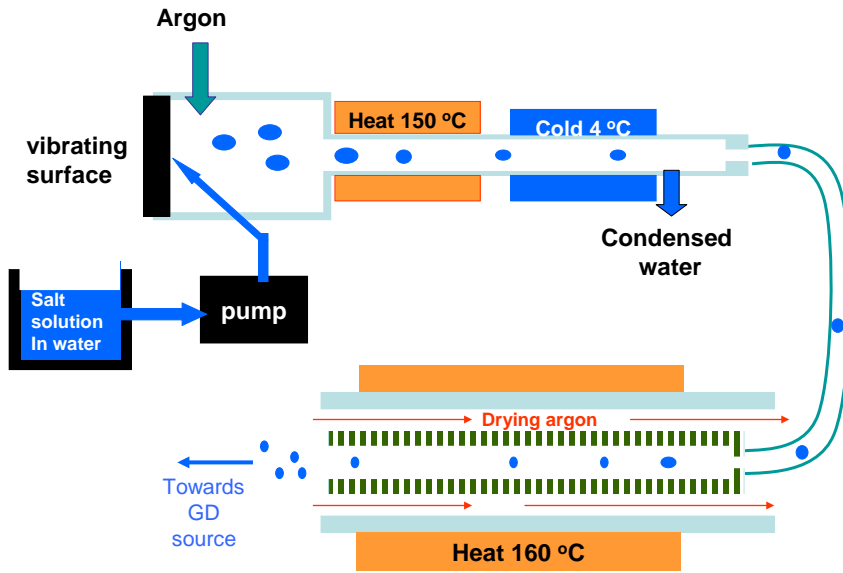


Figure 2-1. The schematics of the ultrasonic nebulizer-dehydrator.

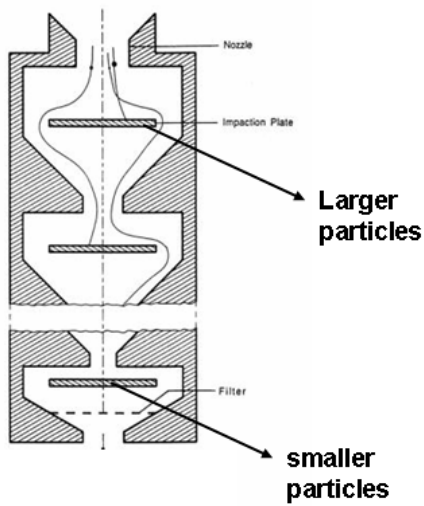


Figure 2-2. The schematics of the particle impactor. [Adopted from Kuhn et. al.⁵⁹]

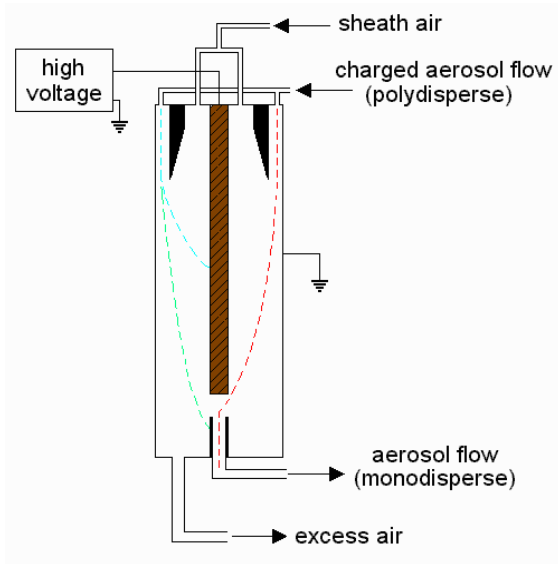


Figure 2-3. The differential mobility analyzer measures the particle size based on their mobility vs. their attraction within electric field.
 [http://www.cac.yorku.ca/mozurke/Analyzer.htm]

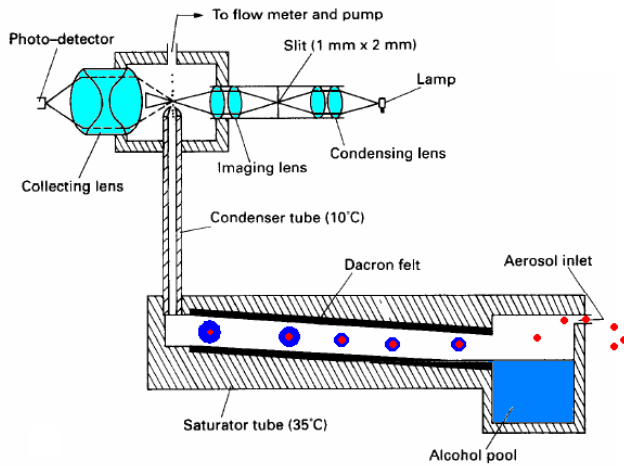


Figure 2-4. The condensation particle counter (CPC) counts the number of particles after they pass through the DMA unit. [Adopted from Clifford et. al.⁵⁶]

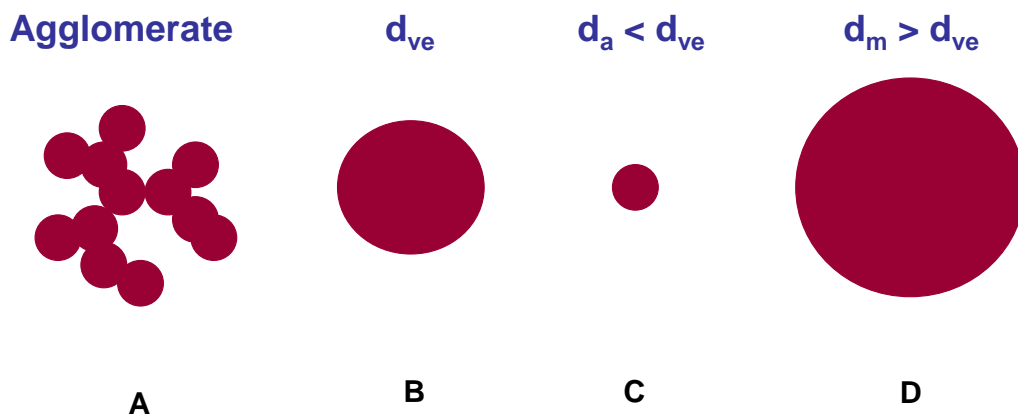


Figure 2-5. Comparing the results of different particle sizing methods. The agglomerated particles (A) will result in false particle size measurements compared to their real equivalent volume diameter (B). The impaction will result in a falsely low aerodynamic diameter (C), while a DMA measures a falsely high mobility diameter (D). [Adopted from Kuhn et. al.⁵⁹]

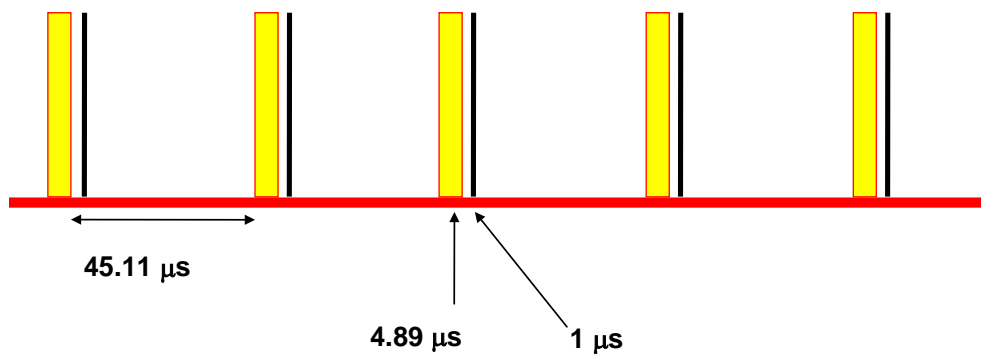


Figure 2-6. The diagram shows continuous ion source (red) vs. the modulator-repeller gating pulses, for the original ICP-MS design.

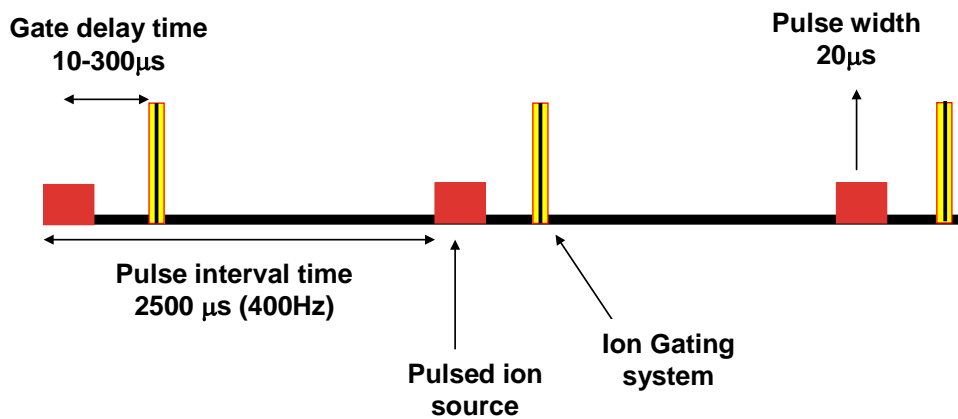


Figure 2-7. The diagram shows the pulsed GD ion source (red) vs. the modulator-repeller gating pulses.

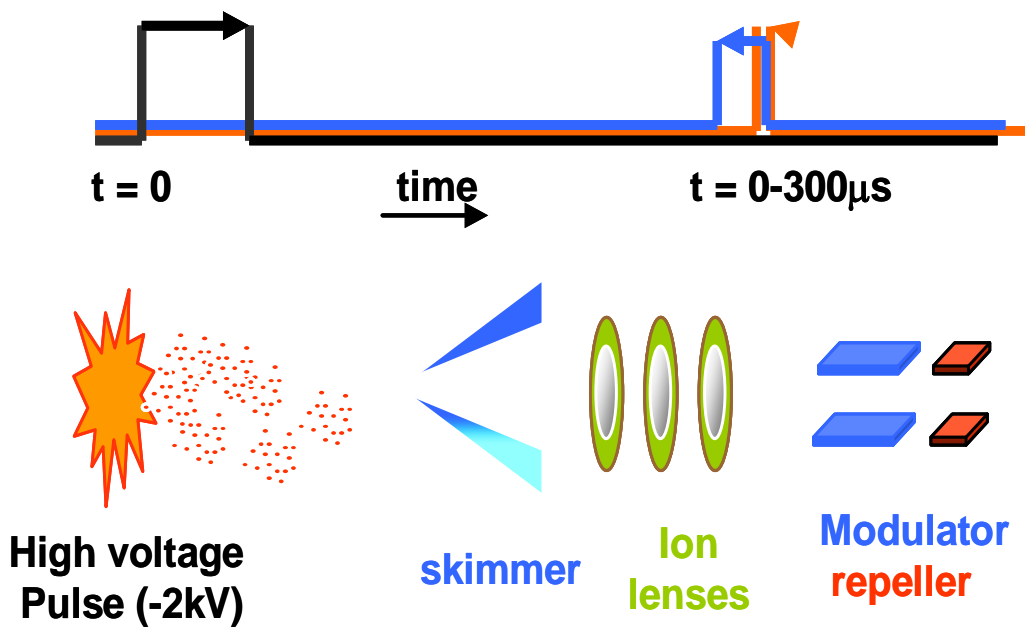


Figure 2-8. The schematics of repeller and modulator with respect to the pulsed ion source.

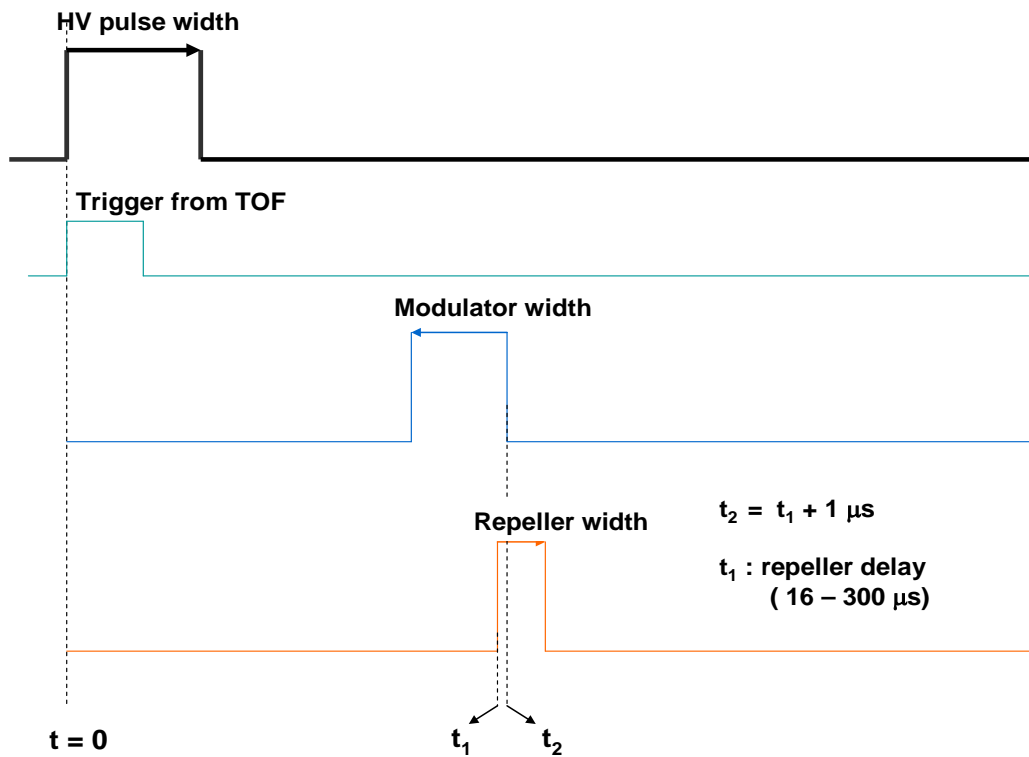


Figure 2-9. The timing diagram for the time-of-flight trigger vs. the repeller and modulator.

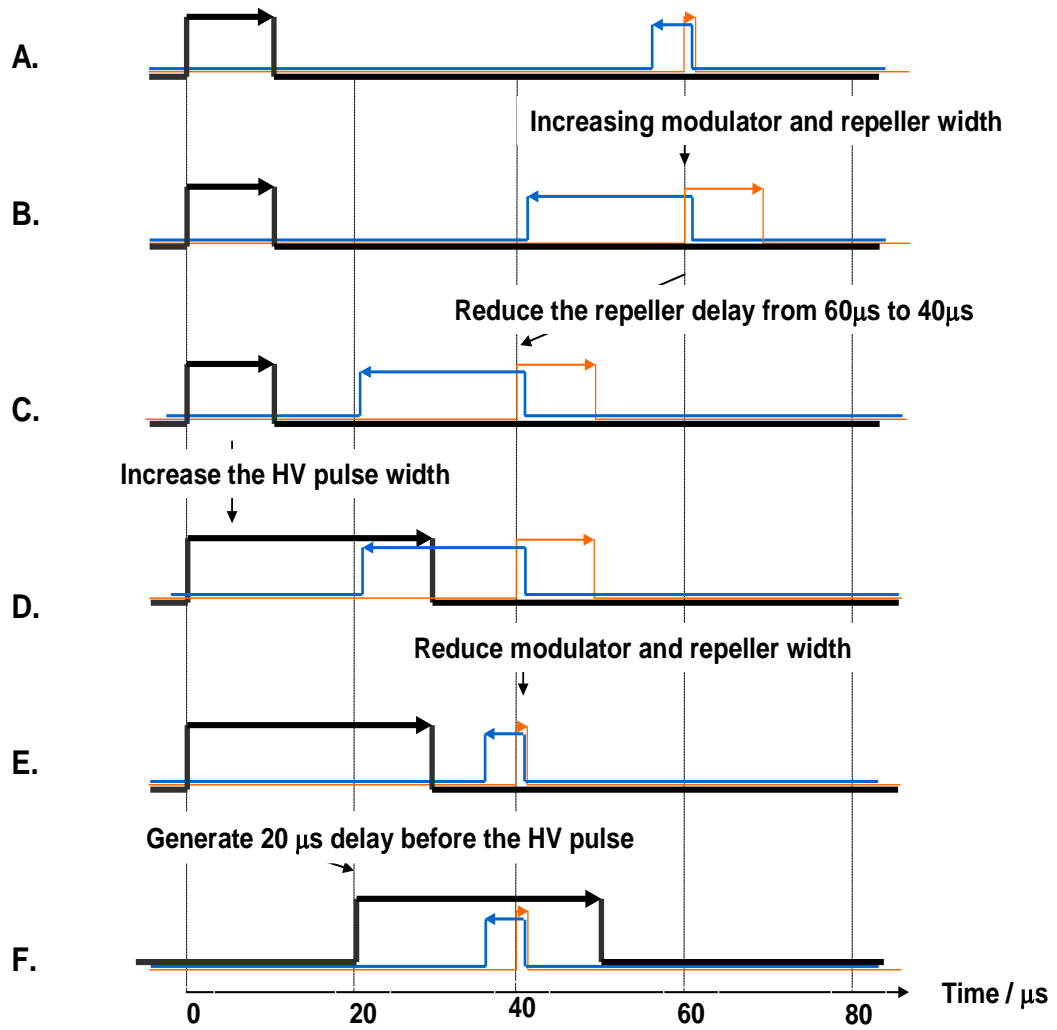


Figure 2-10. The effect of changing different instrument variables on timing diagram.

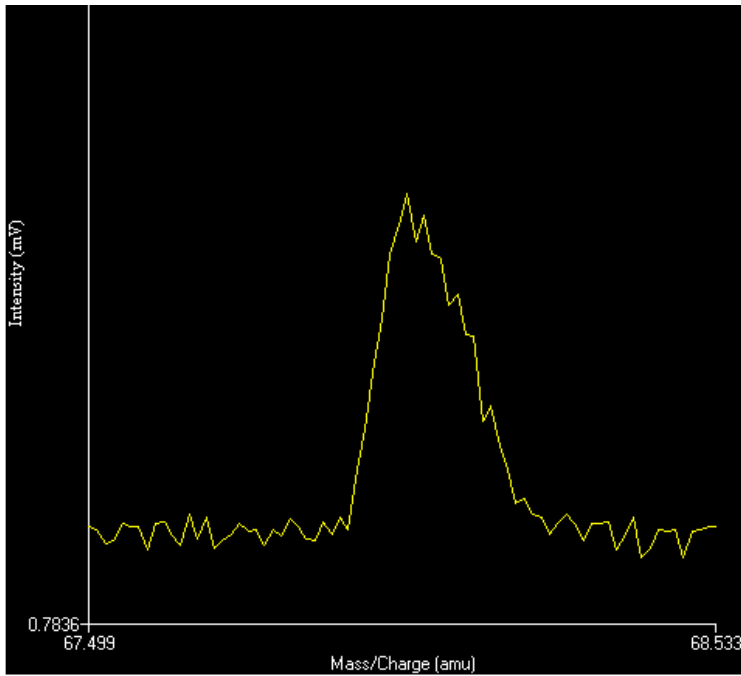


Figure 2-11. A sample mass spectrum from the instrument software. The ^{68}Zn peak is shown for comparison purposes with the same peak in figure 2-12.

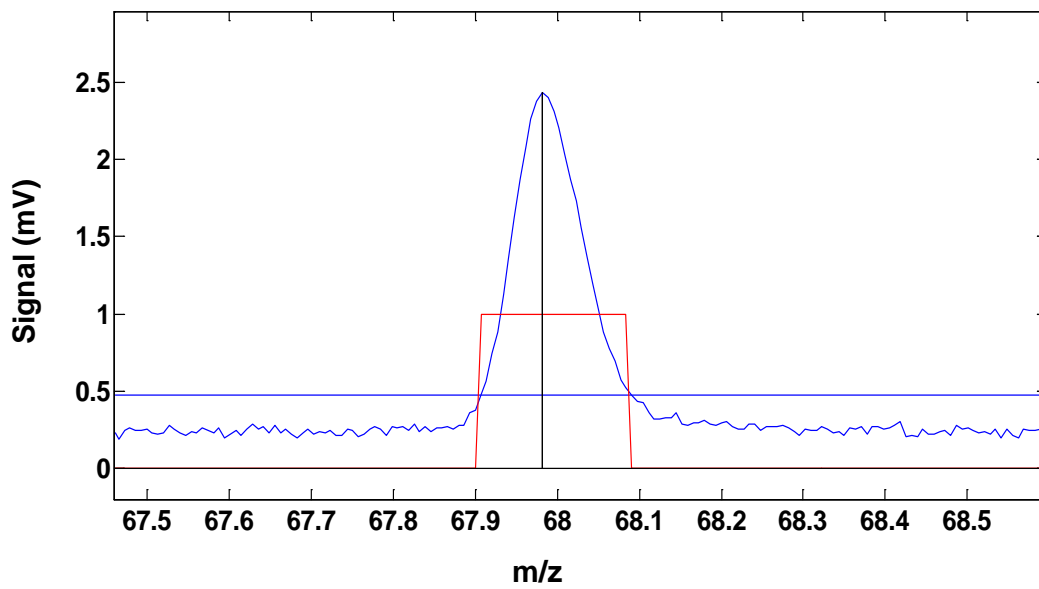


Figure 2-12. A sample mass spectrum from the oscilloscope. The ^{68}Zn peak is shown for comparison purposes with the same peak in figure 2-11.

CHAPTER 3

A NOVEL PULSED GRIMM-TYPE GLOW DISCHARGE SOURCE FOR IONIZATION OF SALT AEROSOLS

Introduction

Glow discharge is a well-known plasma source in analytical chemistry for atomization and ionization. The resulting atoms and ions can be identified using optical emission spectroscopy (GDOES) or mass spectrometry (GDMS). Although glow discharge is mainly used to study solid samples, the increasing interest in the study of aerosols has led analytical chemists to find functionality in glow discharge as a source for atomization and ionization of particles. The need for an online detector for liquid chromatography was the primary motivation for development of particle ionization techniques. As for most other low pressure ion sources, the challenge was to send a stream of dry particles into the ionization source. Since a small amount of solvent can severely suppress the plasma, the complete removal of solvent from the aerosol is very important. Marcus et al. have extensively used a particle beam sample introduction device to generate a dry flow of particles into the glow discharge source.⁶²⁻⁶⁷ The particle beam strikes a hot target (or the heated cathode itself) and evaporates. The resulting vapor will then enter the glow discharge plasma for further atomization and ionization. Both optical emission spectroscopy^{64, 65} and mass spectrometry^{62-64, 66, 67} were used for quantitative and qualitative analysis of the particles.

Grimm-type glow discharges were originally used for depth profiling of solid samples. Pulsed glow discharge time-of-flight mass spectrometry was later introduced.^{31, 69-72} Pulsing has the advantages of enhanced sample sputtering, excitation and ionization and reduced thermal effects.^{32, 33, 68} Due to the timed nature of the pulse, spatial resolution of the sputtered atoms from the plasma ions can also be achieved if the pulse is synchronized with the repeller of the time-of-flight mass spectrometer. It has been shown that the pulsed GDMS can be used to obtain

elemental fractional and molecular information from gaseous analytes.⁶⁹ This is due to different ionization energies at the initiation, plateau and after termination of the pulse.

In recent years the interest in the study of aerosols has prompted scientists to investigate the possibility of the development of aerosol mass spectrometers.⁷⁰⁻⁷² Most of the aforementioned techniques utilize a laser beam for ionization of particles.⁷⁰ Non-laser methods usually include extreme heating of the particles. For example, flash vaporization of particles in a closed-ended tube that was heated up to 600 °C followed by electron ionization (EI), generated ions from particles.⁷¹

To our knowledge, no one has used a pulsed Grimm-type GD as a source of ions for mass spectrometry of particles. The previous particle beam GDMS uses a DC hollow cathode GD source with heating serving as the main source of particle vaporization.^{63, 64, 67, 76-78} It has actually been indicated that vaporization from the cathode walls must be the major means of particle vaporization. This is due to the fact that plasma ionization energies are less than 25 eV, and the kinetic temperature of the plasma is not capable of dissociating particles in the gas phase. However, it is well known^{18, 26, 76, 77} that the high energy atoms and ions in the cathode dark space of a Grimm-type GD are capable of sputtering the metal atoms from the cathode surface. This brings about the potential for vaporization of particles in this high energy region. This chapter investigates the interaction of particles with high energy argon ions and atoms in the cathode dark space (CDS) of the Grimm glow discharge (without heating the cathode).

Most plasma sources such as ICP and glow discharge only provide atomic ions for mass spectrometry. Molecular and fragmented ions have been reported in a few cases. For example, microwave plasma-GD of volatile organic compounds⁷³ and variable frequency, switched, direct current GD of halogenated hydrocarbons⁷⁴ resulted in atomic and molecular ions. Another

purpose of this work is to investigate the possibility of observing atomic versus molecular information at different pulse zones. This application of pulsed-GD has been shown by sending molecular vapors of simple organic compounds into a pulsed GDMS source.⁷⁵⁻⁷⁸

Since the focus of this research is on fundamental study of interaction of aerosols with Grimm pulsed GD-TOF-MS, a commercial ultrasonic nebulizer-dehydrator unit (efficiency of less than 5%) was used to generate simple aerosols from inorganic salt solutions. For quantitative purposes, this is a disadvantage when compared with a particle beam device, which has an efficiency of up to 97%.⁶⁷

Experimental

The overall schematic of the instrumentation is shown in Figure 3-1. A flow of salt particles in argon is generated and transferred through a needle valve into the low pressure GD source for ionization. A high voltage μ s-pulsed power supply (M3k-20, Instrument Research Company, MD) that is triggered by the instrument control module (ICM) of the mass spectrometer provides a negative potential to the cathode of the GD source. The ICM also triggers the repeller of the mass spectrometer with a variable delay time (0-300 μ s), controlled by the software. The temporal pulse voltage and current can be monitored on a 500 MHz digital oscilloscope (TDS-724D, Tektronix Inc., Beaverton, OR). A 5k Ω , 10W resistor was placed in the circuit and the average current is digitally presented on the pulsed power generator. Table 3-1 provides a list of major operating conditions. Additional parameters not included can be found in previously reported literature.³²

Aerosol Generation and Particle Size Distribution

An ultrasonic nebulizer-dehydrator (U-6000, CETAC Inc., Omaha, NE) was used to produce a stream of dry particles from the corresponding salt solution. The solution is transferred

onto the surface of a piezo electric vibrating stage by a peristaltic pump (M312, Gilson, France), where argon flow generates a mist. The resulting aerosol goes through a heating-cooling stage and then enters the dehydrator unit, where an opposite directional stream of hot argon completely dries the particle flow. Industrial argon (Grade 2, Air Gas Inc. Kennesaw, GA) was used as an aerosol carrier into the GD source. Salt solutions were prepared by dissolving the corresponding solid salts (Fisher Scientific, Pittsburgh, PA) in deionized, distilled water. NaI, CsI and acetate salts of some transition metals were used. In an independent experiment, a particle size analyzer (Aerosizer LD, API Inc., TSI Inc, Shoreview, MN) was used for particle size distribution measurements.

Mass Spectrometer

The mass spectrometer is an axial commercial ICP-TOF instrument (Renaissance, LECO Corp., St. Joseph, MI) that was modified by removing the ICP source to accept an in-house designed Grimm-type GD source.³² In addition, a variable repeller delay was added to the instrument and its software (LECO Renaissance version 1.16, LECO Corp.). The repeller delay indicates the time difference from the start of the high voltage pulse at the GD source to the start of the high voltage pulse on the repeller. There is a modulator that always functions in synchrony with the repeller in a way that the trailing edge of the modulator pulse always ends 1 μ s after the leading edge of the repeller pulse. The pulse widths used for the repeller and the modulator were 2 μ s and 5 μ s, respectively. The transient mode of the software was used to record the m/z values for selected peaks as a function of time. Integration time was set to 2.0 s. For collecting full mass spectra, the detector was connected to the oscilloscope and the resulting mass spectrum was saved on the computer through a GPIB-PCI interface.

Grimm-Type GD Ion Source

The GD source geometry was the same as the Grimm source used by Harrison et al. previously.³² In order to send particles into the discharge, the particles were introduced through the gas-directing sleeve entrance from the space between the anode and the sampler. However, sending particles through the gas-directing sleeve entrance resulted in a loss of particles and clogging. As a result, no atomic signal related to the particles was observed.

Cathode modification

In order to overcome this problem, a small orifice (0.5 mm) was placed at the center of the cathode so that the particles could enter the discharge from the back of the cathode. In order to center the cathode orifice with respect to the anode, the cathode base was also threaded. Figure 3-2 shows a schematic of this cathode design. Since the back sleeve was no longer required, the sampler was also replaced with a flat sampling device.

New anode design

After cathode modification, the particle ionization signal was observed using a typical cylindrical Grimm-type anode (anode A). However, implementing a different anode (anode B) that is a concealed cylinder with 4 off axis orifices instead of a hollow cylinder resulted in improved signal intensity and discharge stability (Figure 3-3). One of the advantages of this new anode design was preventing large particles from moving directly towards the skimmer by blocking them. This reduced the risk of particles entering into the second stage of TOF, which can contaminate ion lenses. Figure 3-4 shows the detailed GD source geometry with anode B. The cathode is machined from brass and the anode from copper. The effective cathode diameter is 5 mm. The cathode anode distance is 0.50 mm. The four orifices of the anode have diameters of 1.5 mm each and are 2 mm away from the center. The particles move along the argon flow and enter the area between the cathode and the anode, where a high voltage pulse causes

ionization. The ions pass through the 4 holes of the anode into the first stage of TOF, where some of them reach the skimmer. Since the skimmer and sampler are both grounded, the majority of the flow (including the ions) is pumped out at this stage. An adjustable diaphragm valve (Model: Sp35K, BOC Edwards, Wilmington, MA) controls the amount of pumping and the pressure of the first stage. The ions that pass through the skimmer orifice, after passing through the second stage ion lenses and acceleration by the repeller, will be detected in the TOF analyzer.

Pressure and Flow Measurements

The pressure of all three stages of the instrument is displayed on the mass spectrometer software. For the measurement of the source pressure (the anode-cathode gap), a dual sensor vacuum gauge (Model: 2002, Teledyne Hastings Instruments, Hampton, VA) was connected to the source through the back sleeve gas entrance. Since particles can harm the digital flow meters, the flow of argon gas without the presence of particles was measured using 2 parallel digital mass flow meters/controllers (Model: M100B, MKS Instruments, Andover, MA). A soap bubble meter was used to calibrate the digital flow meters. The argon flow was then calibrated with respect to the first stage and the source pressure (P_1 and P_s). These pressures were used to calculate the flow during aerosol introduction.

Results and Discussion

At first, a 10.0 mM solution of NaCl was used for generating salt particles, and sodium signal was monitored. Since the back sleeve of the source had clogging problems and no sodium signal was detected, the cathode was modified as mentioned in the experimental section. The next course of action was choosing the best salt, one that produced the highest signal and could be used for fundamental studies. The modified cathode, along with anode A, resulted in ionization of a variety of salt particles generated from different salt solutions (10.0 mM). The positive-ion signal for both anion and cation of such salts was observed at the correspondent m/z

value: NaI ($\text{Na}^+ = 23$, $\text{I}^+ = 127$), NaCl ($\text{Na}^+ = 23$, $\text{Cl}^+ = 35, 37$), NaF ($\text{Na}^+ = 23$) RbI ($\text{Rb}^+ = 85$, $\text{I}^+ = 127$), CsI ($\text{Cs}^+ = 133$, $\text{I}^+ = 127$), $\text{Mg}(\text{NO}_3)_2$ ($\text{Mg}^+ = 24$), MnAc_2 ($\text{Mn}^+ = 55$, $\text{CO}_2^+ = 44$, $\text{HCO}_2^+ = 45$), CoAc_2 ($\text{Co}^+ = 59$, $\text{CO}_2^+ = 44$), NiAc_2 ($\text{CO}_2^+ = 127$). Ac represents the acetate ion.

The signal intensity for I^+ was higher than other non-metals due to the lower ionization energy of iodine. The ionization potentials (in eV) for I, Cl, F and Ar are 10.45, 12.97, 17.42 and 15.76, respectively. Since Ar^+ is the major source of ionization in the plasma, Fluorine can not be ionized. The signal for chlorine was also much lower than that of iodine. It is important to consider that the major source of ionization in the negative glow is the Penning ionization, which is due to meta-stable argon atoms ($\text{Ar}^* = 11.55$ eV and 11.72 eV). The sodium in iodide salt showed a higher signal than that of chloride. This can be explained by lower energy of vaporization for NaI, which has a melting point of 670 °C compared to NaCl = 801 °C. Among the metals, the estimated relative signal intensities for Cs, Rb, Na, Co, Mn and Mg were 15, 13, 6, 5, 5 and 1, respectively. It appears that singly charged cations produce a larger signal (for example Na vs. Mg), and that as the mass of the atom increases, the signal also increases. This will be discussed in more detail later in this chapter. The signal for Ni had a very low intensity; this can not be all explained by ionization energy (IE) or atomic mass as the IE of Ni is lower than Co and they almost have the same mass. However, both Co and Mn have only one naturally occurring isotope, while Ni has multiple isotopes ($^{58}\text{Ni} = 63\%$ the most abundant). This could cause the signals for Ni to be lower. CsI and NaI were found to be good choices for further studies, as both salts showed a high degree of ionization and both offer cations with only one naturally occurring isotope.

Anode A vs. B

Although the reconfiguration of the cathode allowed particle introduction into the discharge and resulted in its ionization, it was faced with a few problems. When the argon flow

in this configuration exceeded 300 ml/min, no ionization signal (even from argon) was detected. It seems that at higher flow rates, the atoms do not spend enough time at the electric field of the cathode for ionization. This limits the number of particles transferred to the discharge and potentially causes clogging problems at the needle valve. Another problem was lack of stability in the discharge. The discharge would slowly extinguish after ~30 min, and close inspection showed contamination on the sharp edge of the cylindrical anode. Finally, after a period of about one month, no particle ionization was observed. The careful inspection of the cathode under a microscope showed that the sharp edge of the cathode orifice, where the particles enter the discharge, was etched (Figure 3-5). The sharp edges are responsible for an intense electric field that can enhance ionization. The use of anode B with a higher surface area was a solution for such aforementioned problems. In this configuration, the flow does not pass through the discharge quickly, but rather has to travel in a diagonal way towards the four off-axis anode orifices. As a result, the atoms and the particles will spend a higher time in the discharge area, allowing the use of higher flow rates. Figure 3-6 shows the Cs signal vs. repeller delay time from CsI aerosols for the two anode configurations. The larger surface area of this new anode also provides higher signal stability. In addition to discussed advantages of anode B, it also provides a more intense electric field (Figure 3-7) at the point that particles enter the discharge; this compensates for the lack of sharp edges and allows for stable particle ionization.

Cathode Dark Space (CDS)

Understanding the cathode dark space⁷⁹ (or fall region) is essential in explaining the results of particle ionization. Cathode dark space is the thin layer in front of the cathode which is necessary to maintain the discharge. The electric field decreases linearly across this region from a large value at the cathode to eventually zero at the end of this region. When the anode-cathode distance decreases, the positive column and later the Faraday dark space and finally the negative

glow will disappear in the anode. While the fall region also shrinks, it remains as a component to sustain the discharge.

Anything that facilitates the function of the discharge will shorten the cathode dark space. Increasing temperature, pressure and voltage, as well as utilizing a gas with lower ionization energy, or a cathode material that can readily emit electrons will all reduce the length of the cathode dark space.⁷ In glow discharge mass spectrometry, if an atom is ionized in the cathode fall region, the electric field of the cathode will attract the ion towards the cathode: as a consequence, the ion will not be detected. Atomic emission does not face such a problem. As a result, a shorter cathode fall region and a longer mean free path of the atoms are desired for mass spectrometry.⁹ The mean free path needs to be long to prevent atoms from undergoing collision-ionization with argon ions and fast argon atoms (the main elements for sputtering) until they leave the cathode fall region. Ideally, the mean free path of the atoms must be longer than the cathode fall region.

Effect of the Flow and Source Pressure

To study the effect of the particle flow, 3 different particle flows of 440, 630 and 875 ml/min were used. Figure 3-8 shows that the increase in flow did not change the shape of the Cs signal profile significantly; the signal maximum was only shifted a few microseconds to earlier delay times. This was to be expected, as the ions move faster in the higher flow. When the aerosol flow doubles from 440 to 875 ml/min, the Ar and Cs signals increase. However, closer examination shows that although the amount of analyte transferred to the discharge is only doubled, the signal has increased by the factors of 4 and 9 for Ar and Cs, respectively. This finding indicates that a factor other than flow itself must play a role here.

It is important to note that anode B provides a smaller effective surface area for the flow to proceed towards the first stage compared to anode A (5.4 mm² vs. 20 mm²). As a result, the flow

is at the sonic regime and the pressure of the source is much higher than the first stage pressure. At this regime, the flow is a direct function of the effective surface area and the upstream pressure.⁸⁰

$$\mathbf{F = constant \cdot P_{up-stream} \cdot A_s} \quad (3-1)$$

In this equation, F is the flow from the source into the first stage and A_s is the total surface area of the holes on anode B. As mentioned previously, an increase in pressure reduces the length of the cathode dark space which allows more ions to escape the fall region. It has been shown that a pressure increase from 50 to 100 Pa in a 1400V Grimm-type argon discharge resulted in a decrease in length of the cathode fall region (CDS) from 3.5 mm to less than 1 mm.⁷ Another effect of the increase in pressure is an increase in mean energy of the argon ions and fast argon atoms. These are the main species responsible for sputtering, and also vaporization-atomization and ionization of the particles at the cathode dark region. For instance, as pressure is increased from 50 to 100 Pa, mean energy of the argon ions at the maximum of their profile increases from 170 eV to 220 eV. For fast argon atoms, this mean energy increase is from 44 to 47 eV.⁷

Finally, higher pressure means higher population density of ions and atoms. This density increases the number of collisions and assists in vaporization, atomization, and ionization. Additionally, it is important to note that the increase in pressure reduces the mean free path of the atoms and increases the possibility of ionization. This increases the ion signal due to increase in ionization in the negative glow. However, the ions that are formed in the CDS will not be able to leave this region; hence the cathode's electric field will attract them back. Experimental results illustrate that other factors overcome this problem and the overall signals increase as flow increases.

Effect of the First Stage Pressure

The pressure effect was studied using the optimum flow of 875 ml/min. Figure 3-9 shows that the signal profile and intensity changes with an increase in the pressure from 1.36 torr to 3.1 torr. The 1.45 torr offers the best signal intensity and also shows 3 maxima. The signal profile change due to the first stage pressure (P_1) does not follow a very clear pattern. It seems that the increase in pressure at first increases the signal, while further change in pressure reduces the signal. It is important to note that the pressure of the first stage is increased by reducing the pumping at this stage. Such a change does not affect the pressure of the source (P_s), as the source pressure is a function of the flow. However, the increase in P_1 increases the flow of ions into the second stage and consequently increases the signal. The number of collisions (with other species and the walls) is also a function of the pressure, which has a negative effect on ion transfer yield.

Effect of the Cathode Potential Pulse Width

The pulse width was changed from 30 μs to 150 μs for a 4 mM CsI solution. The increase in pulse width does not change the intensity or the pattern (2 maximums) of the profile. The higher pulse duration just stretches the signal along the time domain. This can be seen in Figure 3-10, in which where the two pulse durations are compared for Cs. Since the power generator is limited to maximum of 8 mA, one can not just increase the pulse at the same pulse potential. In order to keep the average current within instrument range, the 400 Hz frequency was reduced to 40 Hz in the 150 μs pulse. This was done using a homemade frequency divider with the reduction in frequency by a factor of 10.

Using an external frequency (home built) divider, the TOF will send 10 triggers to the pulse generator, of which only one provides a high voltage to the source. However, the detector collects data for all 10 triggers and averages these collections. As a result, not only the signal and

background noise increases due to less sampling per integration time interval (40 vs. 400 per second), but also the signal intensity drops significantly, as it is the average of one signal and 9 backgrounds. The signal intensity in Figure 3-10 was modified to compensate for this signal decrease.

Effect of the Cathode Potential

The effect of the cathode potential on particle ionization for both CsI and NaI particles is depicted on Figure 3-11 at a fixed repeller delay of 62 μs . When the pulse potential increases, the energy of species in the discharge goes up and, as a result, more particle vaporization-atomization-ionization will occur. This will result in a signal increase. Furthermore, the increase in pulse potential reduces the CDS length, and consequently increases the signal. It seems the plot of signal vs. potential reaches a plateau. This effect is caused by the fact that when the CDS becomes too short, then the particles spend an extremely brief time in this high-energy region, therefore jeopardizing the vaporization process. More importantly, an increase in cathode potential will increase the electric field of the cathode, allowing fewer ions to escape the cathode fall region. In the following section, the effect of the electric field will be examined more in depth.

CsI vs. NaI at Different Repeller Delay Times

A solution of CsI (2 mM) and NaI (5 mM) was used and the signal for Na and Cs, as well as iodine was studied (Figure 3-12). Due to lower sensitivity for Na, its signal is much lower than Cs even if the concentration of Na is higher. Iodine has almost the same sensitivity as Cs and its signal is bigger due to higher concentration (7 mM vs. 2 mM). The argon and copper profiles for the same experiment are shown for comparison. The two argon maxima are located in between the corresponding maxima in the Na and Cs profiles. This observation matches the atomic weight of the three. That means the smaller Na atoms reach the repeller faster than Ar, Cs

and I. Cesium and iodine have almost the same mass ($m/z = 133$ and 127) and their profiles are very similar to each other.

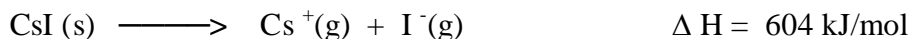
Ionization Mechanism and Sodium vs. Cesium Signal Comparison

As Figure 3-11 demonstrates, the Cs signal from CsI particles is much higher than the Na signal from the NaI particles, whereas both aerosols are generated from salt solutions of equal concentrations (4.0 mM). The signal for iodine, however, is the same for both CsI and NaI. This difference in signal sensitivity could be due to the advantage of Cs and I signals over Na signal at a certain repeller delay time, however, Figure 3-12 shows such discrimination exists at all repeller delays (Na vs. Cs and I). One might attribute this finding to the higher ionization energy of sodium (5.14 eV) compared to Cs (3.89 eV). This cannot be true for a variety of reasons: first, the energy of discharge species in the negative glow is so high that these species are not able to discriminate between Na and Cs. The energies for the meta-stable argon atoms are 11.55 eV and 11.72 eV, while Ar^+ is 15.76 eV. Secondly, when NaI particles are used, the iodine signal is much higher than Na, and iodine has a higher ionization energy of 10.46 eV.

Another possible explanation of the low Na signal could be the higher melting point or heat of evaporation of NaI. Table 3.2 shows the thermodynamic information for these two compounds.⁸¹ It is clear that the processes of vaporization for CsI and NaI do not differ energetically. In addition, when a solution containing both NaI and CsI was nebulized, the Na signal is still much lower than Cs. In this case both compounds share the same crystal so vaporization energy will be the same for them. The last process to consider as the reason for the difference in Na vs. Cs signal is atomization of NaI (g) and CsI (g). This possibility is also rejected, as iodine has a much higher signal than Na (Figure 3-11). If the atomization was the reason, the signal for I must also be much lower for the NaI particles compared to that of CsI. However, the plots of Figure 3-11 indicate that both NaI and CsI with the same concentration

result in almost the same signal for iodine. Any significant difference in vaporization or atomization would not allow this to happen.

Another way to compare the energies involved is through the use of lattice energy combined with electron affinity (-297 kJ/mol) and ionization energy of iodine. For example, for CsI we have:⁸¹



Adding the above reactions will result in the overall reaction:



In other words, the total energy for vaporization, atomization and ionization of both atoms is 1910 kJ/mol for CsI. Similar calculations will result in 2010 kJ/mol for NaI, a mere 5% higher than CsI. Suppression of the Na signal can be explained if we assume that most of the vaporization and atomization of the particle occurs in the cathode dark space of the discharge (Figure 3-13). Since the cathode is not heated to high temperatures and none of the negative glow species have enough energy for particle vaporization, the assumption of vaporization in CDS region must be valid. One other possible mechanism for particle ionization is the aerosol deposition on the cathode surface and its sputtering from the surface. This phenomenon must be very unlikely, as the geometry used in this experiment does not result in particles impacting the cathode. On the other hand, the particles enter from the back of the cathode. Another experiment was also run in which particles were allowed to enter discharge for about 3 mins while the discharge was off. Later, the discharge was turned on and no signal was observed. In another investigation, a droplet of 10 mM CsI solution was placed on the surface of the cathode, and

after vaporization of the water, it was placed into the source. Although a small ion signal was observed, it was much lower than the case of dynamic introduction of particles. These all indicate that the major source of ion signal is due to particle ionization in the CDS by high energy argon ions-atoms. If the resulting ions reach the space beyond the cathode dark space, they will be detected (Figure 3-13). However, it seems that most of the atoms are ionized within the cathode dark space and will not make it to the detector. This is due to the short mean free path of the atoms ($10\ \mu\text{m}$ for Cs, I and $25\ \mu\text{m}$ for Na)⁸² at the discharge condition compared to the CDS length (less than $0.7\ \text{mm} = 700\ \mu\text{m}$).

The reason for detection of some ions, despite this large loss of ions in CDS, is the momentum of these ions. If an ion is formed in the CDS, even if it is attracted towards the cathode it is still possible for this ion to escape the CDS region due to its momentum. Assume a Cs and Na atom are moving away from the cathode with the velocity of V_0 at the same distance from the cathode. If they both get ionized at this point (Figure 3-14), the cathode will attract both of them with an equal force ($F = E \cdot q$); however, for the same force, the smaller ion will have a higher acceleration towards the cathode ($a = F/m$). In other words, Na atoms will accelerate 6 times faster than Cs towards the cathode. The time that it takes for Cs to stop before it moves back will be 6 times longer. Thus Cs will travel a distance 6 times larger than Na, before it is attracted towards the cathode. As a result, Cs has a better chance of leaving the CDS and making it to the detector. Since the reaction cross section of these ions with other species is not well known, it is hard to evaluate the effect of the cross section of ionization on the ionization rate.

Table 3-1. Summary of the experimental parameters.

Category	Parameter	Fixed Value or Range
Nebulizer-Dehydrator	Argon Tank Pressure	90 psi
	Nebulizer Argon Flow	1.0 L /min
	Dehydrator Argon Flow	2.0 L /min
	Solution Flow	1.0 ml/min
	Nebulizer Temperature (high)	150 °C
	Nebulizer Temperature (Low)	4 °C
	Dehydrator Temperature	150 °C
High Voltage Pulse	Pulse Potential (V)	1.5 – 2.5 kV
	Pulse Width	20 – 150 μ s
	Pulse Frequency	100 – 1000 Hz
	Average Current (I)	1 – 8 mA
Gas Flow and Pressure In the Source	Flow	400-1000 ml/min
	Vacuum Valve Position	Turn to Adjust P ₁
	Stage 1 Pressure (P1)	1.3 – 3.0 torr
	Back Sleeve Pressure (Ps)	2 - 30 torr

Table 3-2. Thermodynamic properties of CsI and NaI.⁸¹

Property	CsI	NaI
Melting point / °C	632	661
Heat of melting / kJ/mol	23.9	23.6
Heat of evaporation / kJ/mol	150.2	less than 160*
Lattice energy / kJ/mol	604	704

*The information was not available for NaI, but the value for NaBr is 160.

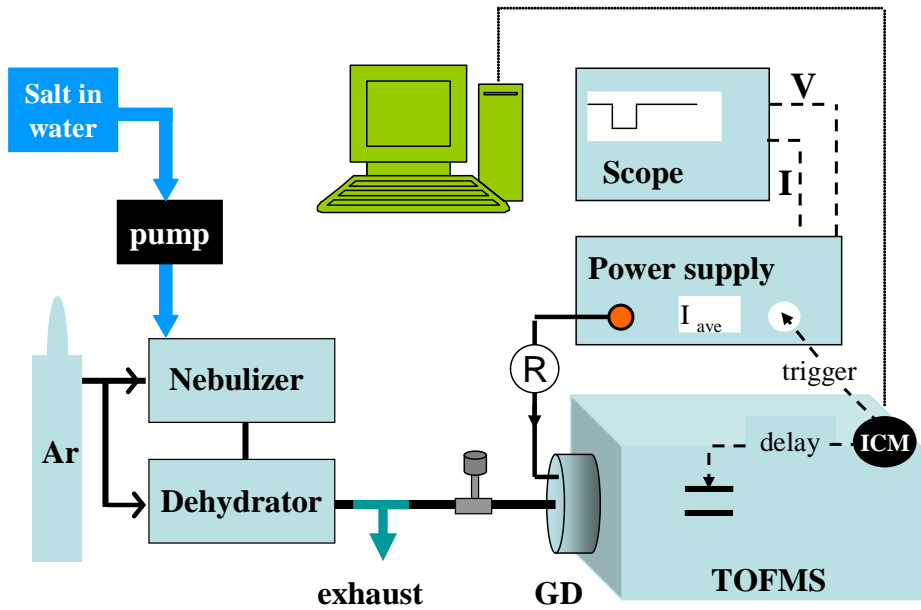


Figure 3-1. The overall schematic of the instrumentation for pulsed GDMS of particles.

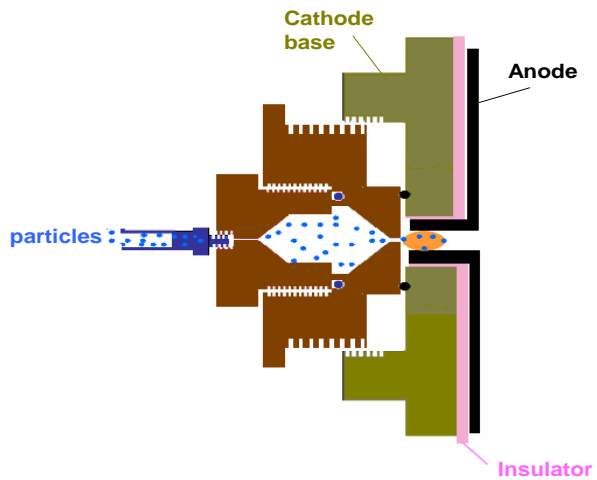


Figure 3-2. Schematic of the cathode design for particle introduction.

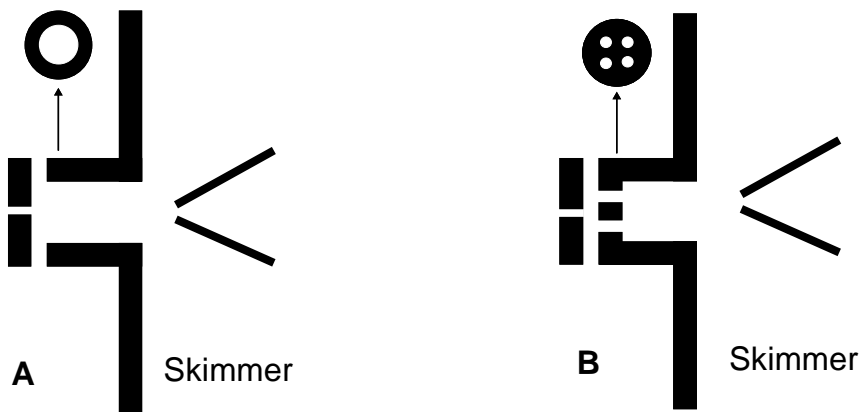


Figure 3-3. Anode A vs. B.

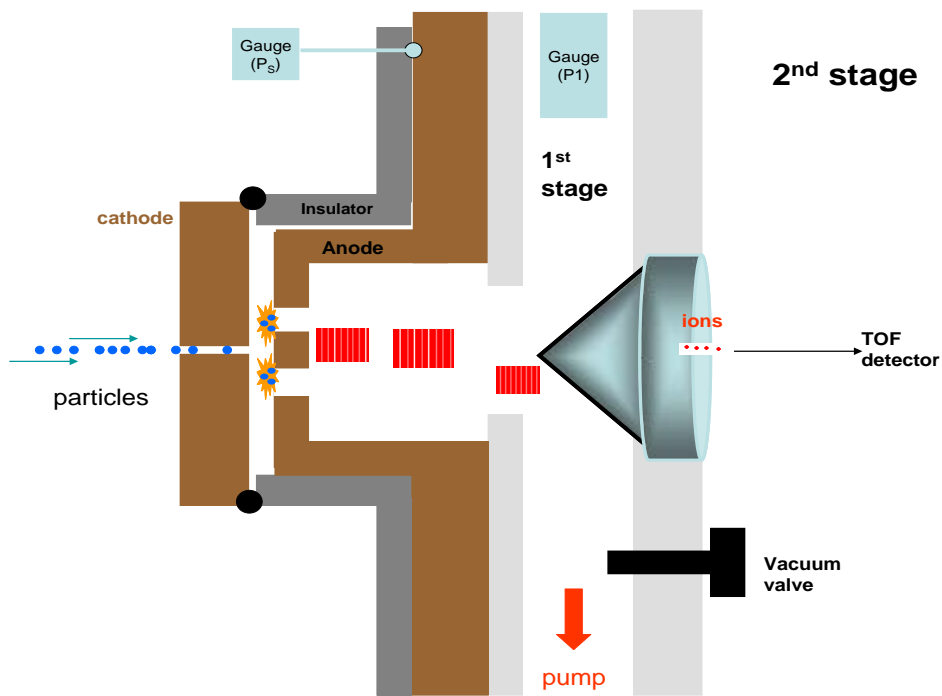


Figure 3-4. Detailed view of the ionization source with anode B. Only the discharge interface of the cathode is shown for simplicity.

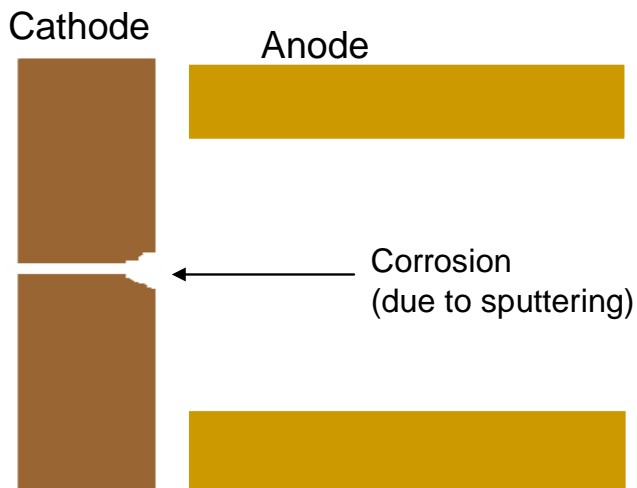


Figure 3-5. The sharp edge of the cathode orifice, where the particles enter the discharge, was etched due to sputtering.

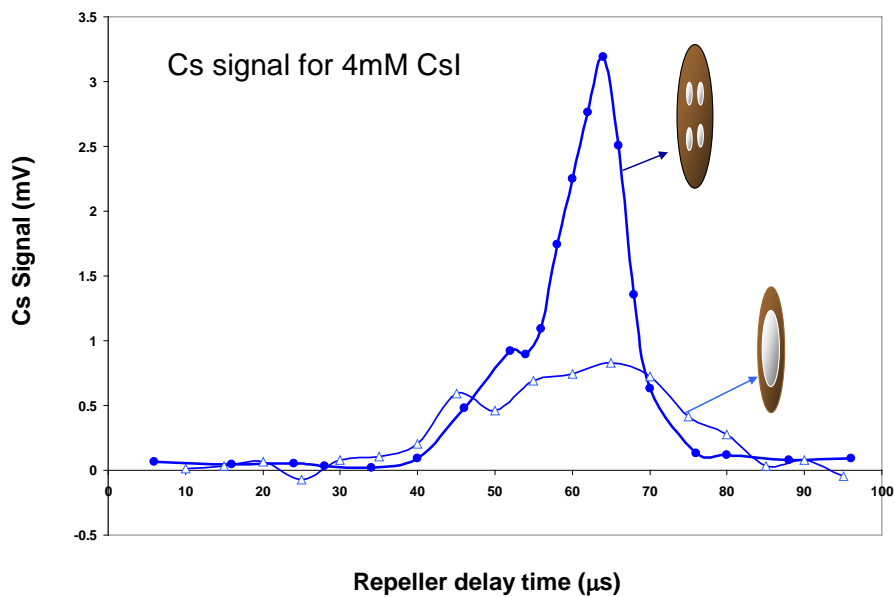
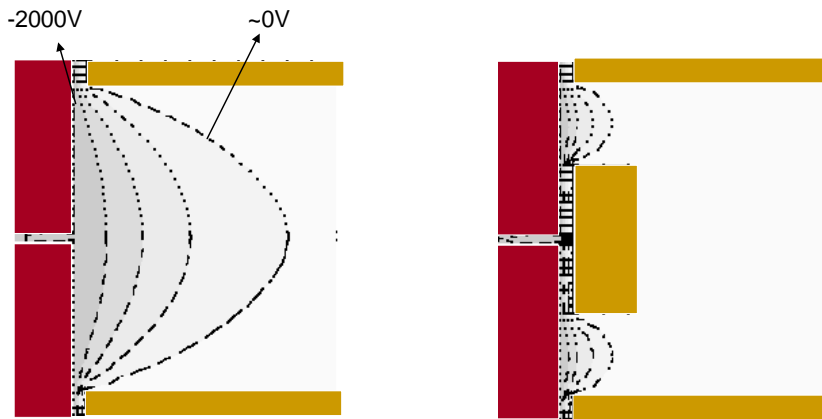


Figure 3-6. The Cs^+ ion signal vs. repeller delay time from CsI aerosols for the two anode configurations. Refer to figure A-13 for a sample with standard deviation of the mean.



Iso-potential lines are shown for both configurations

Figure 3-7. The electric field of anode A vs. B. [Courtesy of Ashkan Behnam, Department of Electrical Engineering, University of Florida, for modeling the electric field using Medici 4.0. Durham, NC: Synopsys, Inc. (2004)]

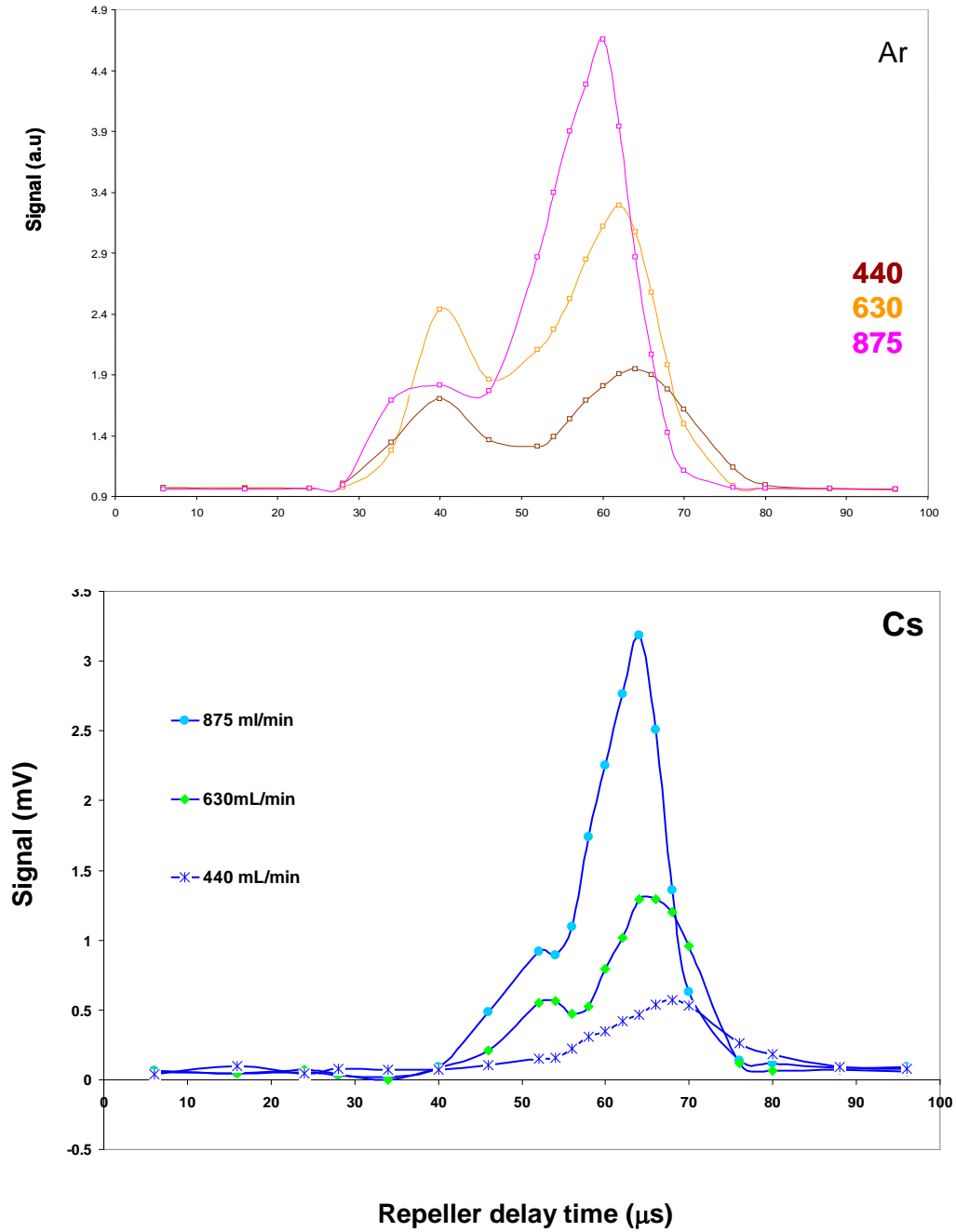


Figure 3-8. Ar and Cs signal vs. repeller delay at three different aerosol flow rates into the source. Refer to figure A-13 for a sample with standard deviation of the mean.

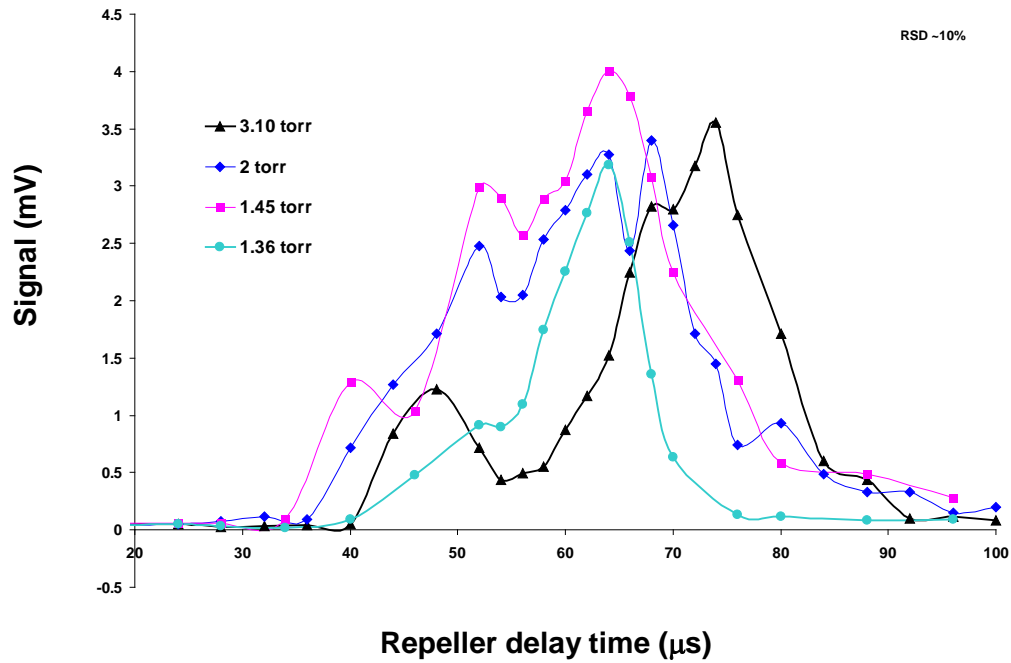


Figure 3-9. Effect of the first stage pressure on signal profile and intensity. Refer to figure A-13 for a sample with standard deviation of the mean.

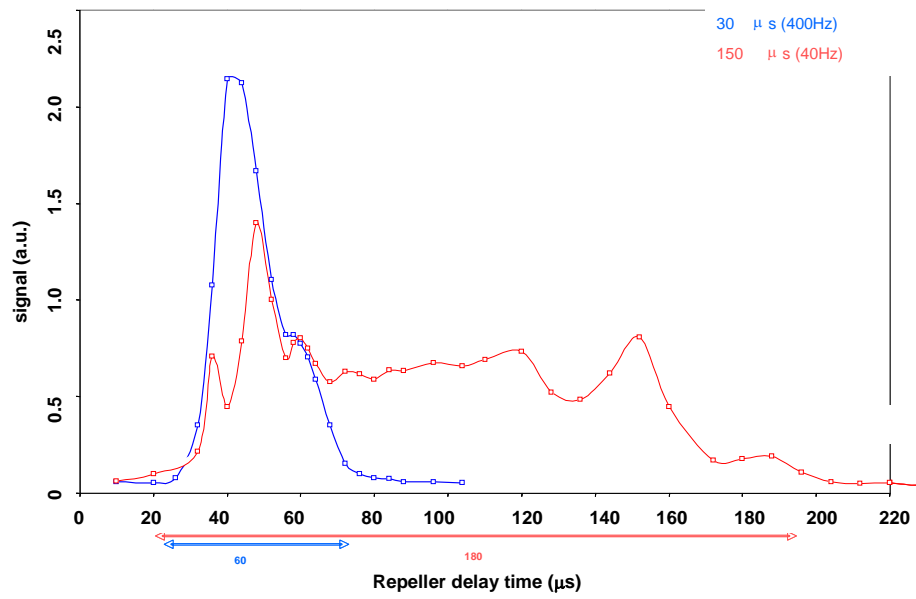


Figure 3-10. Pulse width, where the two pulse durations of 30 μs and 150 μs are compared for Cs signal. Refer to figure A-13 for a sample with standard deviation of the mean.

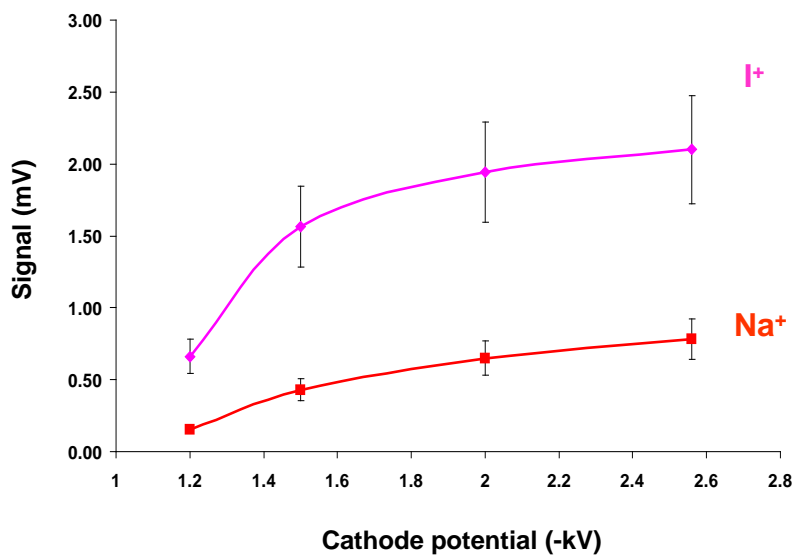
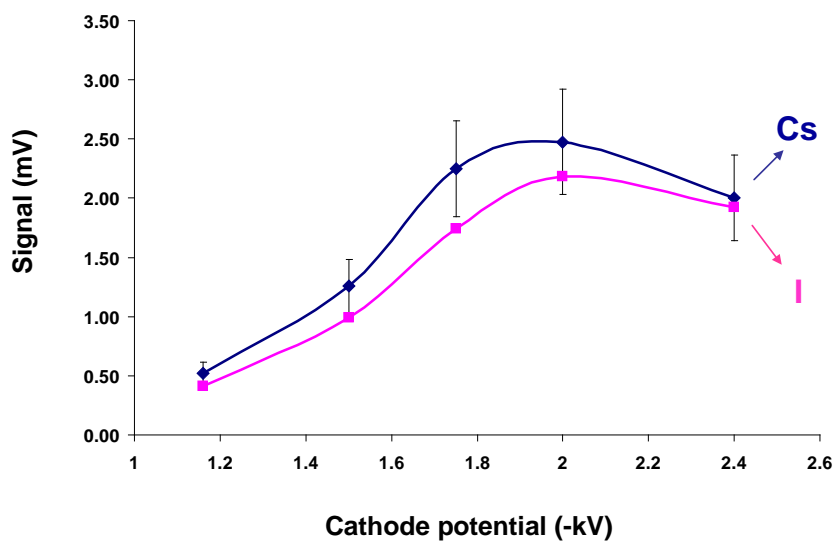


Figure 3-11. Effect of the cathode potential on particle ionization for CsI and NaI. Standard deviation of the mean is shown for an average of $n \sim 15$. The error bars for iodine in CsI are not shown for demonstration purposes as the RSD for I and Cs are similar.

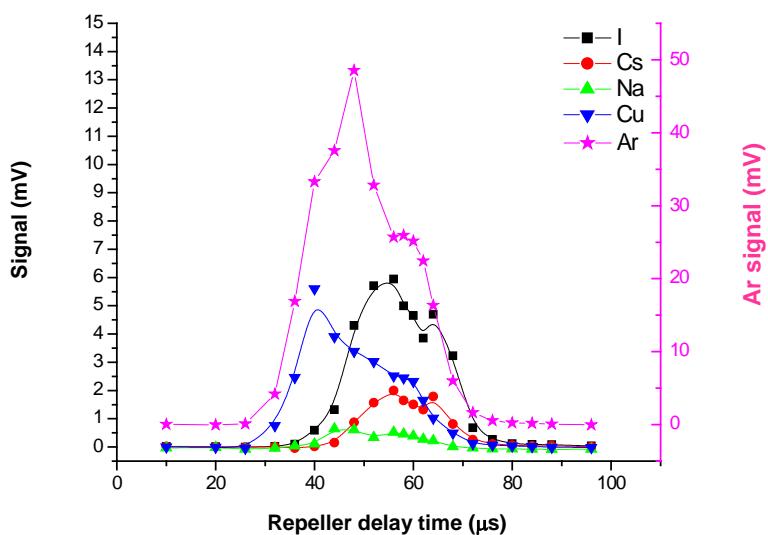


Figure 3-12. Signal vs. delay time for different elements.

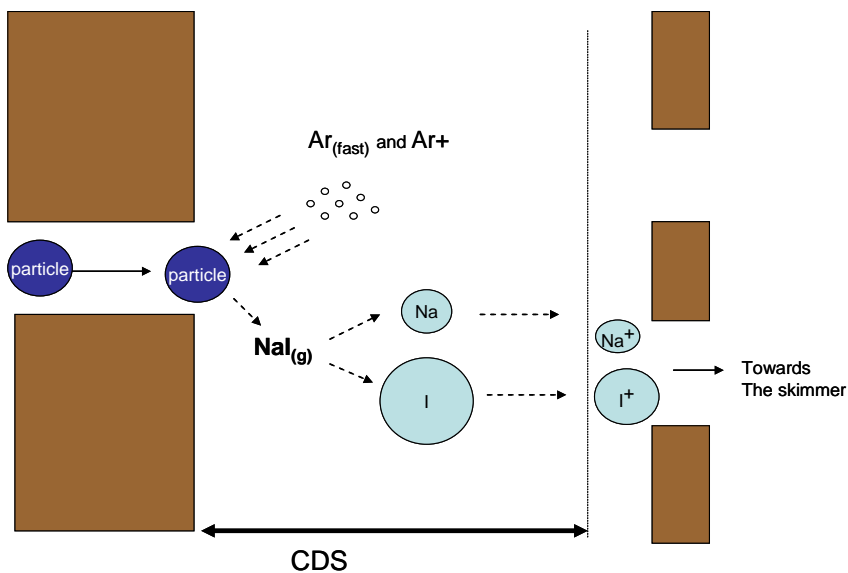


Figure 3-13. Particles enter from the cathode (left). After vaporization, atomization and ionization, if atoms make it out of the CDS, they can ionize in the negative glow. Then pass through the anode and reach the skimmer (sizes are not to the scale). The negative glow region is not shown here due to small anode-cathode distance and for demonstration purposes.

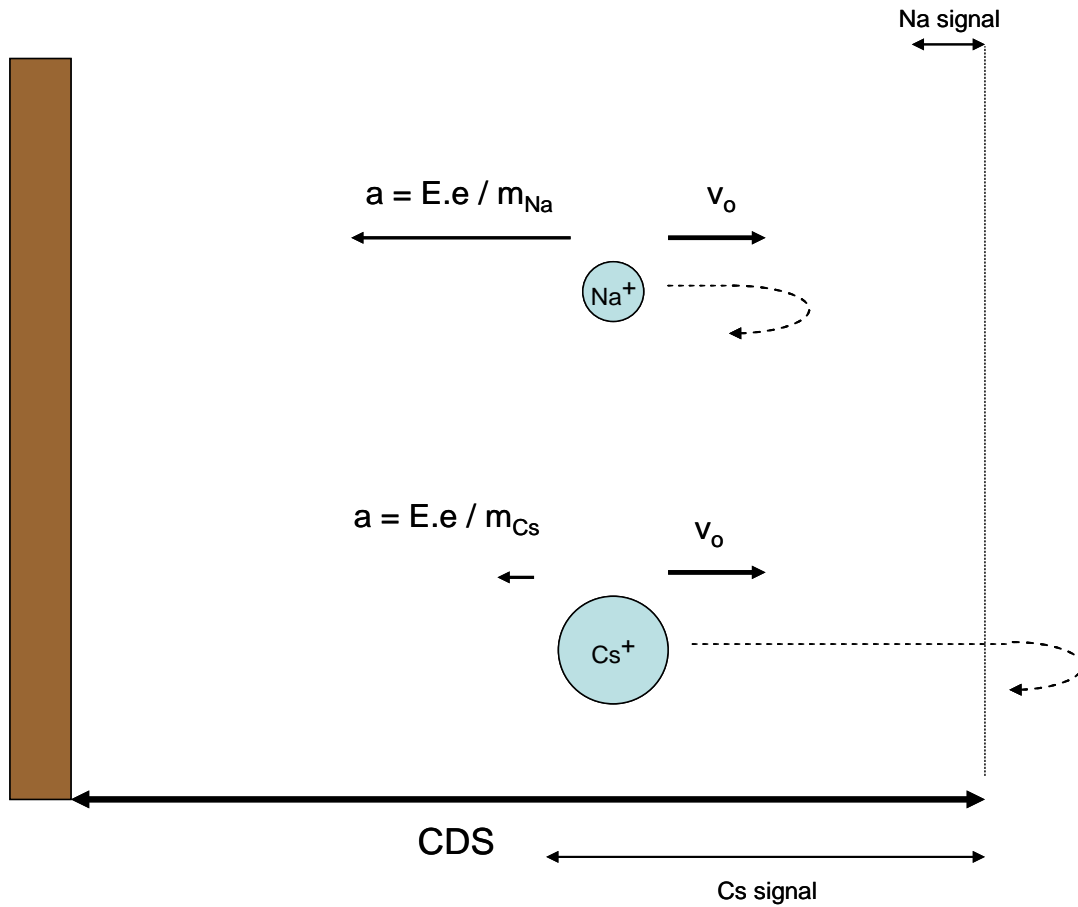


Figure 3-14. The heavier Cs ion travels 6 times farther than Na before it goes back towards the cathode. The Cs and Na ions formed close to the end of the CDS region can still escape the electric field due to their momentum. The Cs and Na signal arrows show the relative distance these atoms have to the CDS border.

CHAPTER 4 PULSED-GLOW DISCHARGE MASS SPECTROMETRY OF PARTICLES: FUNDAMENTAL STUDIES AND DIAGNOSTICS

Introduction

In the previous chapter, the task of introducing particles into the glow discharge was discussed. Of particular interest was the effect of different variables such as aerosol flow rate, discharge pressure and discharge potential on particle ionization.

The vaporization-atomization of particles is believed to mostly happen in the cathode dark space of the discharge, where high-energy argon ions and fast argon atoms have energies as high as 200 eV. Subsequently, the atoms will transfer into the negative glow, and their ionization occurs in this region. In the cathode dark space (CDS) some ions will be formed as well, although most of these ions ultimately return to the cathode due to the large electric field in this region. Nonetheless, those ions formed in part of CDS that is adjacent to the negative glow can still escape the electric field of the cathode due to their momentum. The question remains as to what degree particle vaporization occurs; in other words, does a particle completely evaporate or does it go through partial vaporization? The use of different particle sizes might bring light to such questions. In order to produce salt particles of variable sizes in this investigation, different concentrations of salt will be used for nebulization. In this chapter the results of varying salt concentration and its effect on particle size and ionization signal will be studied.

Another interesting observation was higher signal intensities for Cs and I compared to ion intensity of Na. In the previous chapter, the transfer of ions across the CDS region was recognized to be the main reason for this phenomenon. However, another place in which the possibility for discrimination between the ions may occur is the GD interface with the TOF, where ions are transferred to the second stage of the mass spectrometer. In this chapter, the effect

of skimmer orifice on different ion signals and the effect of cathode temperature on signal intensity will be discussed.

Experimental

Most of the experimental setup used in this chapter is identical to that of Chapter 3. A DC power supply along with two heating cartridges was used to heat the cathode base to the desired temperature. The cathode temperature was measured by a thermocouple thermometer (Digi-Sence, Oakton Instruments, Vernon Hills, IL). Two $\frac{1}{4}$ inch holes and one $\frac{1}{16}$ inch hole were machined on the cathode based in order to place the heating cartridges and the thermometer, respectively. The skimmers with variable orifice diameters were made by LECO Corp. (St. Joseph, MI). For particle size distribution measurements, a particle size analyzer (Aerosizer LD, API Inc., TSI Inc, Shoreview, MN) was used. For modeling the flow, Fluent 6.3.1 (ANSYS Inc. Canonsburg, PA) was used.

Results and Discussion

Effect of Solution Concentration

Solutions of CsI and NaI with different concentrations were used to generate aerosol. Signal vs. concentration was a linear function for these salts. Sensitivities for Cs, I, and Na were 0.61, 0.55, and 0.07 (mV/mM), respectively. The ion signal vs. concentration for cesium iodide and sodium iodide is shown in Figures 4-1 and 4-2. The iodine signal is independent of the type of salt used; this is because the difference between heats of vaporization of these two salts is small, and in both cases the entire particle evaporates. The linearity of signal vs. concentration also indicates that the discharge is completely evaporating the particles of both salts. The particle vaporization efficiency will later be discussed in more detail.

Relative Sensitivity Factors

In the previous chapter, it was observed that the relative sensitivity for Cs and I was much higher than Na. In general, the ion sensitivity in GDMS is a function of: (1) events occurring in the GD source, (2) the ion transfer efficiency through the ion lenses and mass analyzer, and (3) the detector efficiency.²⁹ The effect of atomic mass on ion transfer in the GD source along with the role of the cathode dark space electric field was discussed in Chapter 3. The extraction of ions from the first stage to the second stage through the skimmer orifice is another crucial step in the transfer of ions. In our system, the skimmer and sampler are both grounded and the pressure difference (1.2 torr vs. 0.001 torr) between the two stages is the only driving force for ion extraction. The first ion extraction lens is located about 20 mm behind the skimmer orifice. A large portion of the flow will be scattered and pumped out just past the skimmer orifice. The ions with smaller drift velocities (heavy ions), such as Cs and I, will face less scattering and have a higher chance of reaching the ion extraction lenses. On the other hand, the smaller ions such as Na will drift and pump out; as a result, they carry a lower possibility for detection. This is potentially another explanation for higher Cs and I signal compared to Na. Figure 4-3 shows the fluid dynamic modeling for Grimm source geometry similar to the employed source configuration. As it is demonstrated, the flow will deviate from the center after it passes through the skimmer orifice. If this explanation is correct, changing the skimmer orifice size should affect the relative sensitivity for heavy and light atoms; thus the increase in skimmer orifice diameter should result in higher signal, especially for lower-mass ions such as Na.

Effect of Skimmer Orifice

As the skimmer orifice diameter was increased from 0.43 mm to 0.56 mm, signal sensitivity increased for all elements as expected. As the orifice diameter/surface area increases, more flow is transferred into the second stage and the signal intensifies for all ions. Figure 4-4

shows the relative sensitivity for Cs, I, and Na at two different skimmer orifice diameters. It is also observed that the Cs:Na signal ratio changes from ~10 to ~3 as skimmer orifice diameter increases. This is due to reduction of ion scattering (which influences the smaller ions more) at the extraction orifice when a larger orifice is used.

Effect of Cathode Temperature

As the cathode temperature increased from 23 °C to 75 °C, the particle signal increased by a factor of ~1.25 (Figure 4-4). Figure 4-5 shows the particle ionization signal for various cathode potentials at 75 °C and a skimmer orifice diameter of 0.56mm for CsI. Figure 4-6 shows the same for NaI. Figure 4-7 compares the iodine signal vs. cathode potential at 23 °C and 75 °C. At 75 °C, the signal reaches a plateau at ~1.1 kV, while at 23 °C it reaches its plateau at ~1.8 kV. This demonstrates that the particle vaporization is facilitated at the higher temperature. Since the temperature increase from 23 °C to 75 °C is not an intense increase in the energy of the species, there might be other reasons for these observations. One explanation could be that the higher temperature of the discharge decreases the length of the cathode dark space, and consequently the intensity of the electric field increases. In such a condition, argon ions and fast argon atoms of higher energy participate in the vaporization of particles. In addition, in a shorter cathode dark space more atoms are able to leave the electric field before they ionize through collisions with other species. This way, the atoms will ionize in the field free glow region, where they will not be attracted back to the cathode surface. Thus, more ions will be transferred to the skimmer orifice.

Particle Vaporization Efficiency

The ion signal intensity at the detector (S) in a mass spectrometer is a function of vaporization, atomization, ionization, ion transport and ion detection efficiencies:

$$S = \mathbf{Const.} \cdot f_{(vap)} \cdot f_{(atomization)} \cdot f_{(ionization)} \cdot f_{(ion-transport)} \cdot f_{(detection)} \quad (4-1)$$

Atomization efficiency is only a function of the salt type and does not depend on concentration. Ionization, ion transport and detection efficiencies are also constant for a specific ion and are concentration independent. If the vaporization efficiency is 100%, then the signal will be proportional to particle mass, which linearly corresponds to solution concentration. Thus, the linearity of the signal-concentration graph is indicative of complete particle vaporization.

If the particle vaporization is not complete, this means that only a constant thickness of particles (x) is sputtered by the glow discharge plasma. As a result, the amount of mass evaporated from each particle will be a function of particle surface area:

$$\Delta m = V \cdot \rho = A \cdot x \cdot \rho = 4\pi r^2 \cdot x \cdot \rho = \text{const} \cdot r^2 \quad (4-2)$$

Where V is volume of the dry particle, ρ is particle (salt) density, A is particle surface area and r is particle radius. If one assumes constant total number of particles and constant volume mean diameter (D_v) of wet aerosol regardless of salt concentration, the mean volume of the dry particle will be proportional to the salt concentration (C). It is important to note that as it was discussed in Chapter 3, the particles that arrive in the glow discharge plasma are dry salt particles. Since radius is proportional to the cubic root of volume in a dry particle, in consideration of Equation 4-2, the sputtered mass should be proportional to $C^{2/3}$:

$$\Delta m = \text{const} \cdot C^{2/3} \quad (4-3)$$

If the above assumptions are correct and particle vaporization is partial, then the signal would not show a linear relationship with concentration. Therefore, the linearity of signal vs. concentration is a further evidence for complete particle vaporization. Figure 4-8 depicts the comparison between a partial vaporization model and the experimental data.

However, one might argue that the assumption of constant diameter for the wet particles is erroneous, and wet particle diameter varies as a function of the salt concentration. Table 4-1

shows the experimental values for volume mean diameter (D_v) for particles generated from different salt concentrations. It is well known⁵² that the wet particle diameter produced by an ultrasonic nebulizer is a function of nebulizer frequency (f), solution surface tension (σ) and solution density (ρ):

$$\lambda = \left(\frac{8\pi\sigma}{\rho f^2} \right)^{1/3} \quad (4-4)$$

$$D_v = 0.34\lambda \quad (5-4)$$

Using a nebulizer frequency of 1 MHz and the density and surface tension of pure water, the wet particle diameter for this nebulizer was calculated to be about 5 μm . However, this theoretical value for average wet particle diameter does not agree with experimental and known⁵¹ parameters (10-15 μm) of our commercial nebulizer (due to reasons that are beyond the scope of this work). Figure 4-9 shows the experimental D_v values for dry CsI particles compared with calculated ones based on different wet particle diameters. Both experimental and calculated D_v 's for dry particles show similar trends. Based on experimental dry particle diameters, it is expected that the mean volume diameter of wet particles generated by the nebulizer- dehydrator unit must be about 8-10 μm for CsI at salt concentrations of 1-4 mM. As salt concentration increases, the particle diameter increases as well. Although the experimental results for particle diameter are not exactly the same as calculated results, they would still not result in a linear signal vs. concentration graph.

One interesting observation was the evidence of decrease in the diameter of the wet particle as the salt concentration increases. For example, the experimental D_v value for dry particles generated from a 0.50 mM solution is similar to what is expected from a wet particle diameter of 12 μm . However, for the 4.0 mM solution the expected wet particle diameter is

closer to that of the 8 μm curve. This behavior can not simply be explained by Equations 4-4 and 4-5. The only factor in Equation 4-4 affected by salt concentration is surface tension, which does not change significantly as a function of concentration. For instance, the surface tension of a solution of 0.58% NaCl (wt%) in water is 72.92 dynes / cm, compared to 74.93 dynes / cm when concentration of salt increases nearly 10 times (5.43%).⁸¹ This small increase in surface tension (1.028 times) when entered into Equation 4-4 will result in a minor increase (0.9 %) in wet particle diameter.

It is not easy to find a study in which wet particle diameters are measured directly. Only one example was found in which D_V of wet aerosol generated by 2 different ultrasonic nebulizers and an air-jet nebulizer were measured by laser diffraction analysis.⁸³ The study was aimed to measure the particle size as an indicator of medical nebulizer performance in pulmonary drug delivery.⁸³ The result of this study showed that the wet particle diameter is dependent on salt concentration. Interestingly, this is in agreement with our results; as salt concentration increased, the wet particle diameter decreased.⁸³

Additional evidence for complete particle vaporization is the result of signal vs. cathode potential. Figure 4-5 shows the signal for Cs and I increasing as cathode potential increases at first, and later the signal reaches a plateau. This shows that at a certain potential, the particles have reached complete vaporization and the potential increase does not improve the signal anymore.

Finally, another experiment was devised to investigate the extent of particle vaporization. In this experiment, four different solutions with a constant concentration of CsI = 2.0 mM were prepared. The concentration of NaI in these solutions ranged from 0 to 6.0 mM. As Figure 4-10 shows, the Cs signal was almost constant regardless of NaI concentration. If the particle

vaporization had not been absolute, Cs signal would be expected to decrease as the concentration of background NaI salt increases.

Effect of Background Salt

Four different solutions with a constant concentration of CsI = 2.0 mM were prepared. The concentration of NaI in these solutions was 0, 2.0, 4.0 and 6.0 mM. Figure 4-10 shows the Cs signal vs. NaI concentrations for these four solutions. Interestingly, the increase in concentration of NaI (background salt) does not have a significant effect on Cs signal. Figure 4-11 shows the Na signal for these four solutions vs. NaI concentration and compares it with a similar plot in which no Cs background is present. The results show that no significant change in sensitivity of Na is observed due to the presence of 2.0 mM CsI. Figure 4-12 shows the iodine signal produced from these solutions. The concentration of iodine is equal to the total concentration of both NaI and CsI solutions. These results reconfirm the complete vaporization of salt particles in the glow discharge plasma.

Effect of Particle Ionization on Discharge Species

When CsI particles enter the discharge the copper signal increases while the argon signal is subject to a minor depression. Figure 4-13 shows the ion signal vs. time for Cs, Cu, and Ar for an experiment in which particles were generated by nebulization of a 4 mM CsI solution for 30 seconds. The spike in copper signal is indicative of increasing cathode sputtering efficiency. This can be explained by the temporal increase in pressure due to particle vaporization and also the bombardment of the cathode by Cs and I ions. The decrease in argon signal is due to loss of argon ions in ion exchange reactions between argon ions and Cs, I and Cu atoms. Another reason for the decrease of argon signal could simply be the plasma cooling down due to introduction of particles. The temporal decline in argon signal upon particle introduction has also been reported in ICP studies.

Effect of Cathode Potential–Particle Ionization Mechanism

Figure 4-14 compares the iodine signal from the particle ionization with the signals from argon and copper. The increase in copper signal (due to particle introduction) is also shown as a function of cathode potential. The Cu signal increases linearly with cathode potential due to an increase in cathode sputtering. Conversely, the iodine signal reaches a plateau and does not follow a linear pattern. The pattern of particle ionization signal (iodine) is similar to that of argon signal. This indicates that particles ionize in the gas phase as opposed to the cathode surface. The change in Cu signal indicates the increase in Cu signal due to introduction of particles. This signal increase follows a pattern similar to that of particle ionization, which indicates the ions resulting from particle ionization are the source of this increase in sputtering.

Table 4-1. Dry particle mean volume diameters (DV) for different concentrations of CsI and NaI. A particle size analyzer (Aerosizer LD, API Inc., TSI Inc, Shoreview, MN) was used for particle size distribution measurements.

Salt concentration /mM	DV /nm for CsI	DV /nm for NaI
0.1	290 ± 10	NA
0.5	333 ± 6	316 ± 8
1	380 ± 5	350 ± 10
2	441 ± 8	385 ± 9
4	510 ± 5	470 ± 10
10	610 ± 15	510 ± 15
40	820 ± 20	NA
100	1023 ± 20	NA

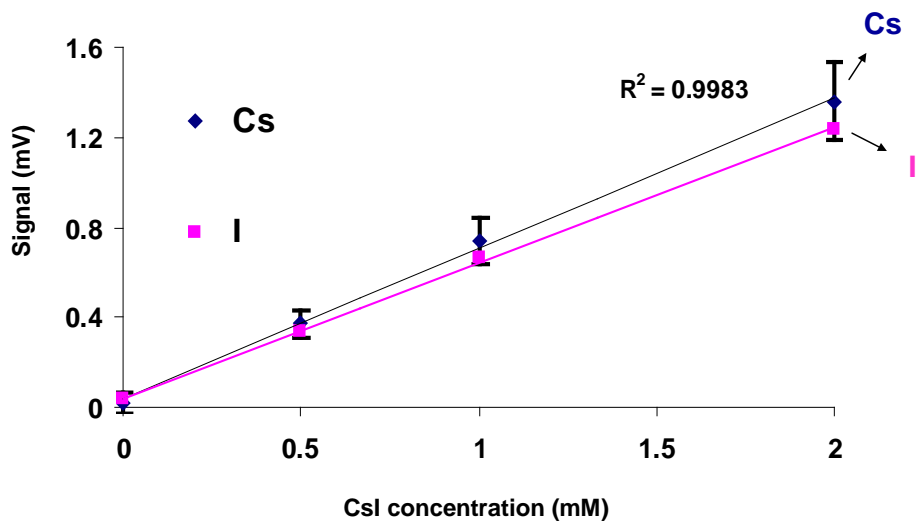


Figure 4-1. Quantitative study of cesium iodide with different solution concentrations. The error bars for iodine are not shown for demonstration purposes as the RSD for I and Cs are similar. Refer to figure A-14 in Appendix A for more information about linear dynamic range and detection limit.

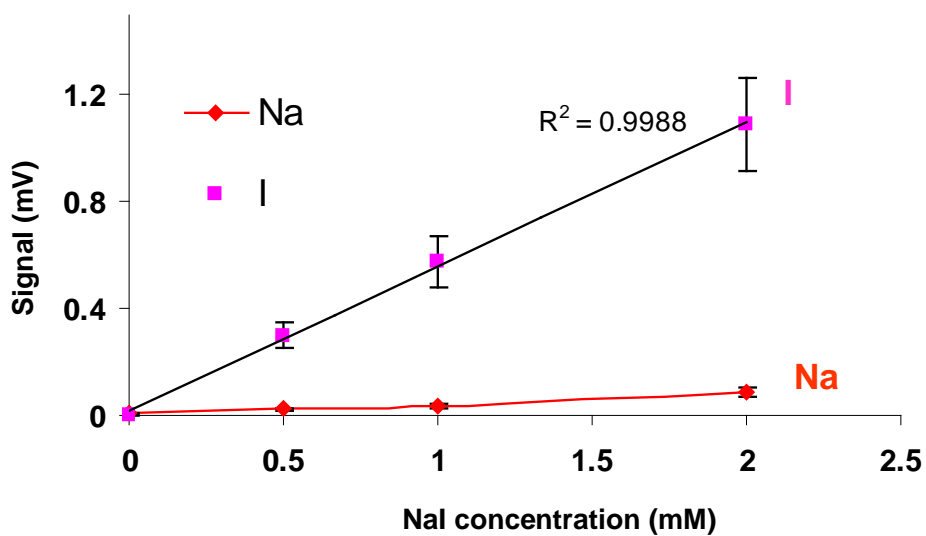


Figure 4-2. Quantitative study of sodium iodide with different solution concentrations.

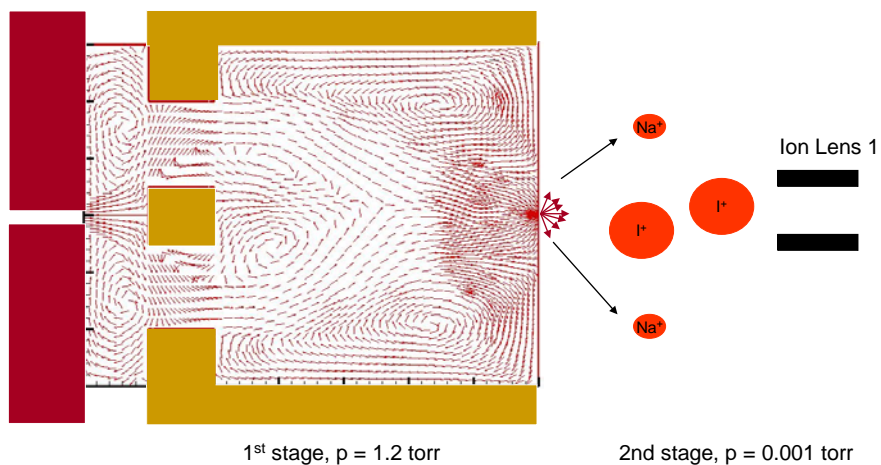


Figure 4-3. Modeling the flow for the glow discharge source. Courtesy of Ayyoub Mehdizadeh, Department of Mechanical engineering, University of Florida. The software used is Fluent 6.3.1 (ANSYS Inc. Canonsburg, PA). Divergence of smaller ions at skimmer orifice can explain the low signal value for sodium in comparison with iodine and cesium.

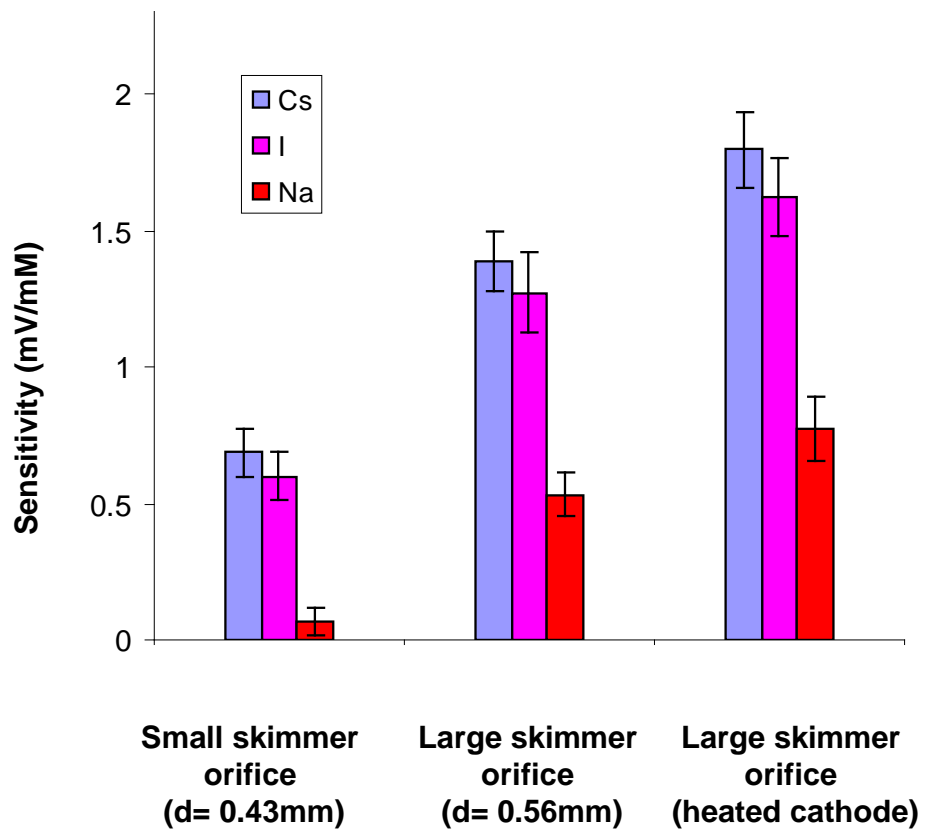


Figure 4-4. Effect of skimmer orifice size and heating the cathode on sensitivity for Cs, I and Na.

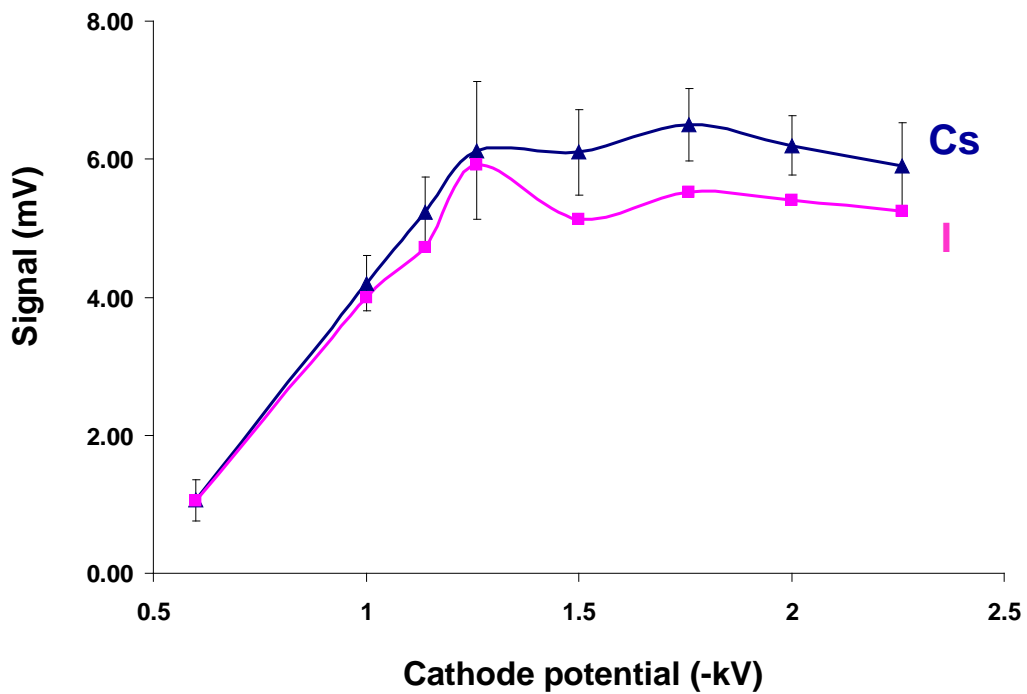


Figure 4-5. Effect of cathode potential for CsI 4 mM at cathode temperature = 75°C and skimmer orifice diameter = 0.56 mm. The error bars for iodine are not shown for demonstration purposes as the RSD for I and Cs are similar.

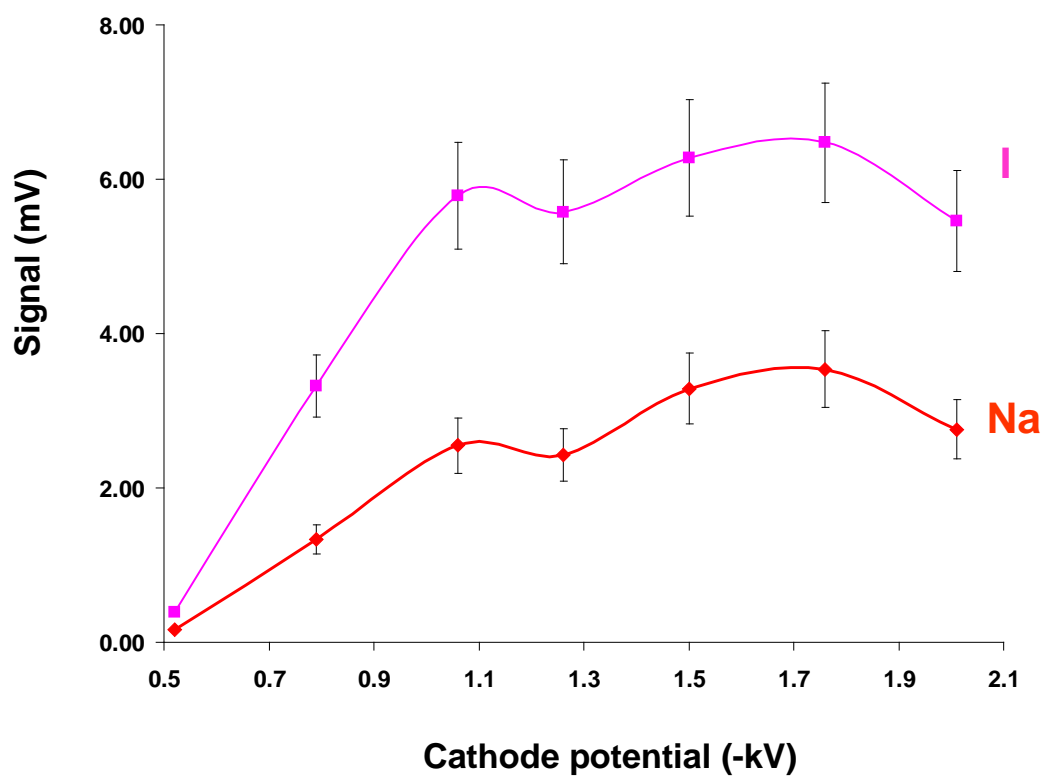


Figure 4-6. Effect of cathode potential for NaI 4 mM. Cathode temperature = 75°C and skimmer orifice diameter = 0.56 mm.

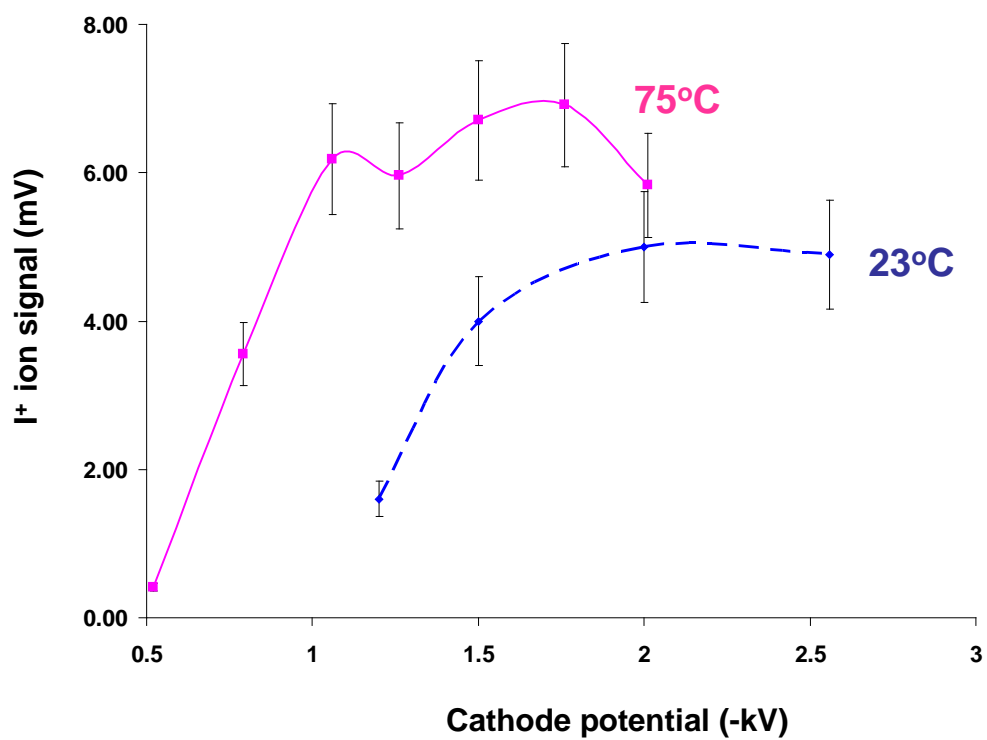


Figure 4-7. The change in signal vs. cathode potential for iodine ion using a 4.0 mM cesium iodide solution.

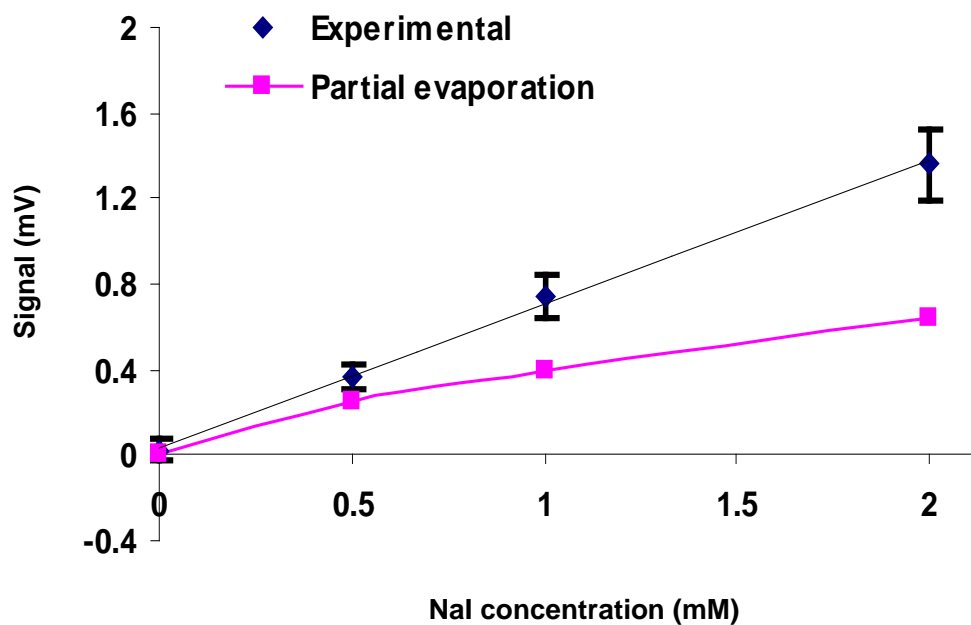


Figure 4-8. Comparing the ion signal vs. salt concentration for the experimental results vs. partial vaporization model.

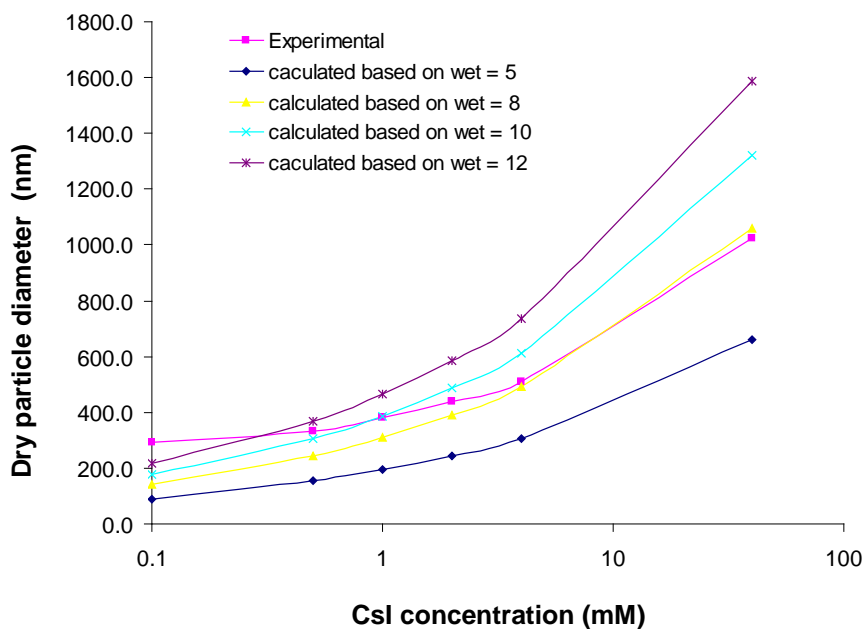
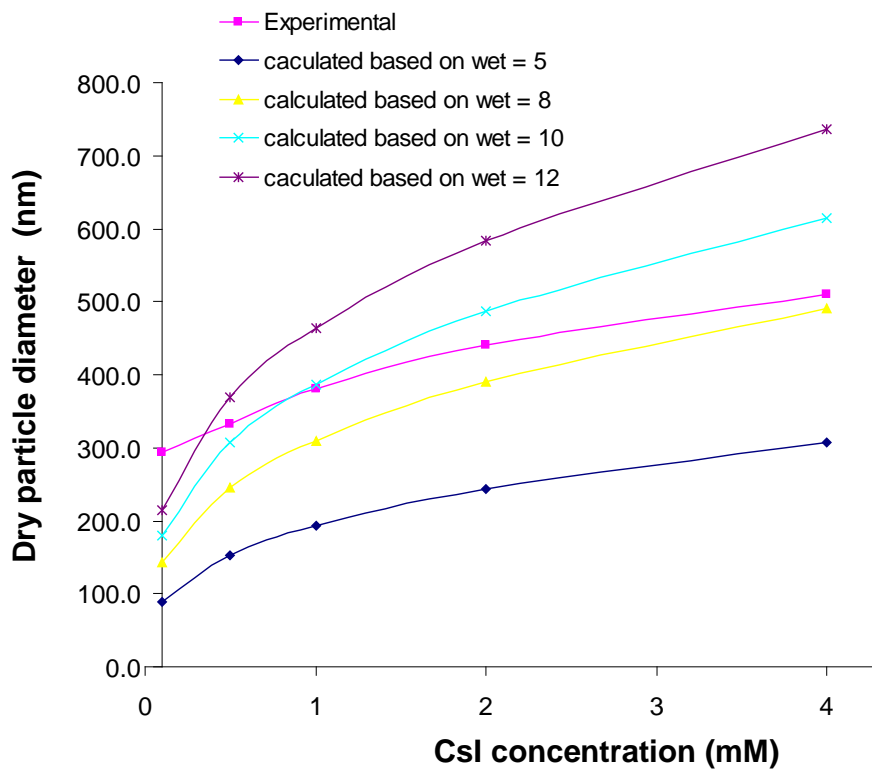


Figure 4-9. Mean volume diameters for different CsI concentrations. Top: 0.1 mM to 4.0 mM, Bottom 0.1 to 100 mM (logarithmic scale). Experimental values are compared to calculated values based on 4 different wet particle diameters.

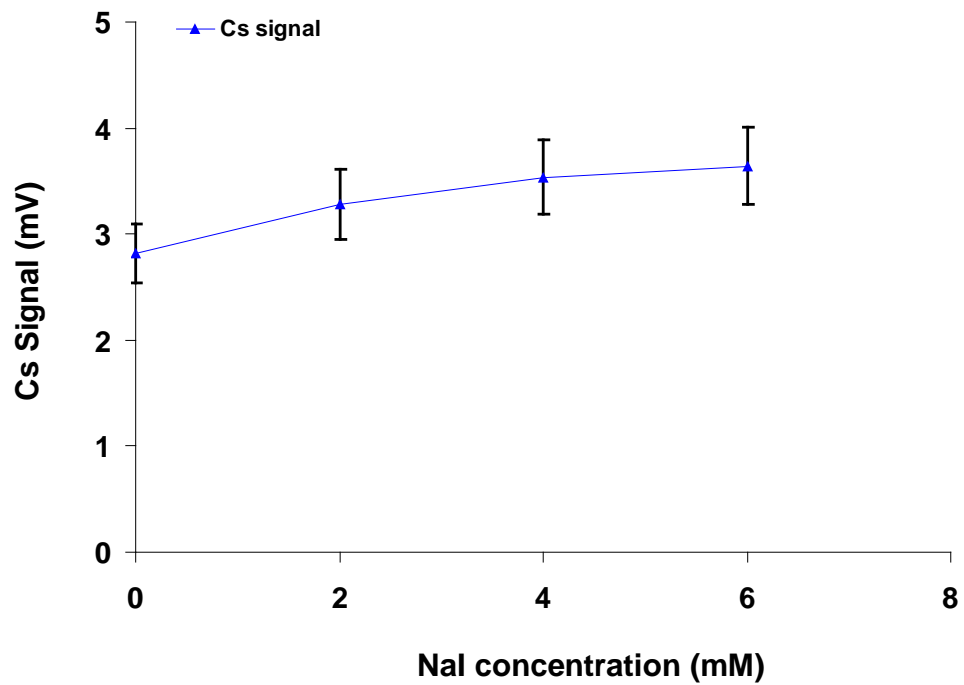


Figure 4-10. Cs⁺ ion signal from 2 mM CsI in different NaI backgrounds.

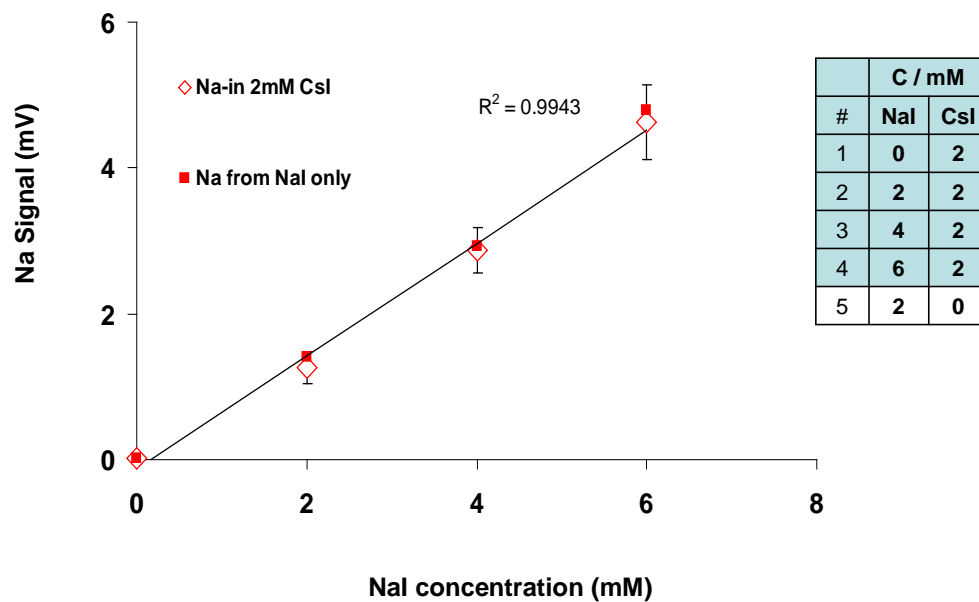


Figure 4-11. Signal vs. concentration for Na^+ ion at different NaI concentrations at the presence of 2 mM CsI background compared with no background.

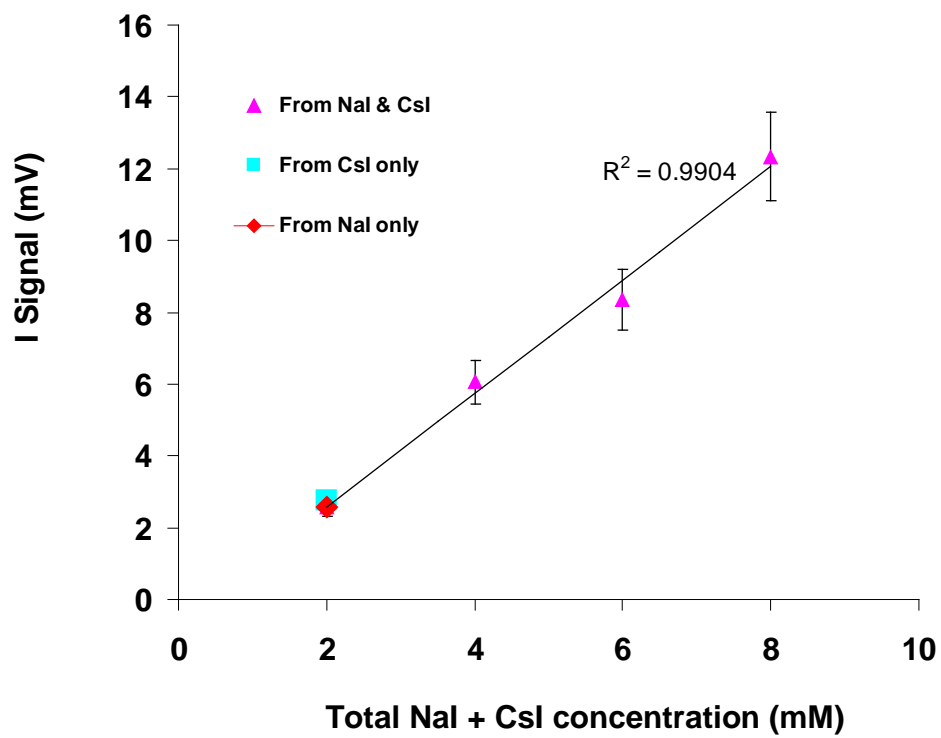


Figure 4-12. Iodine ion signal resulted from different NaI solutions at the presence of 2 mM CsI.

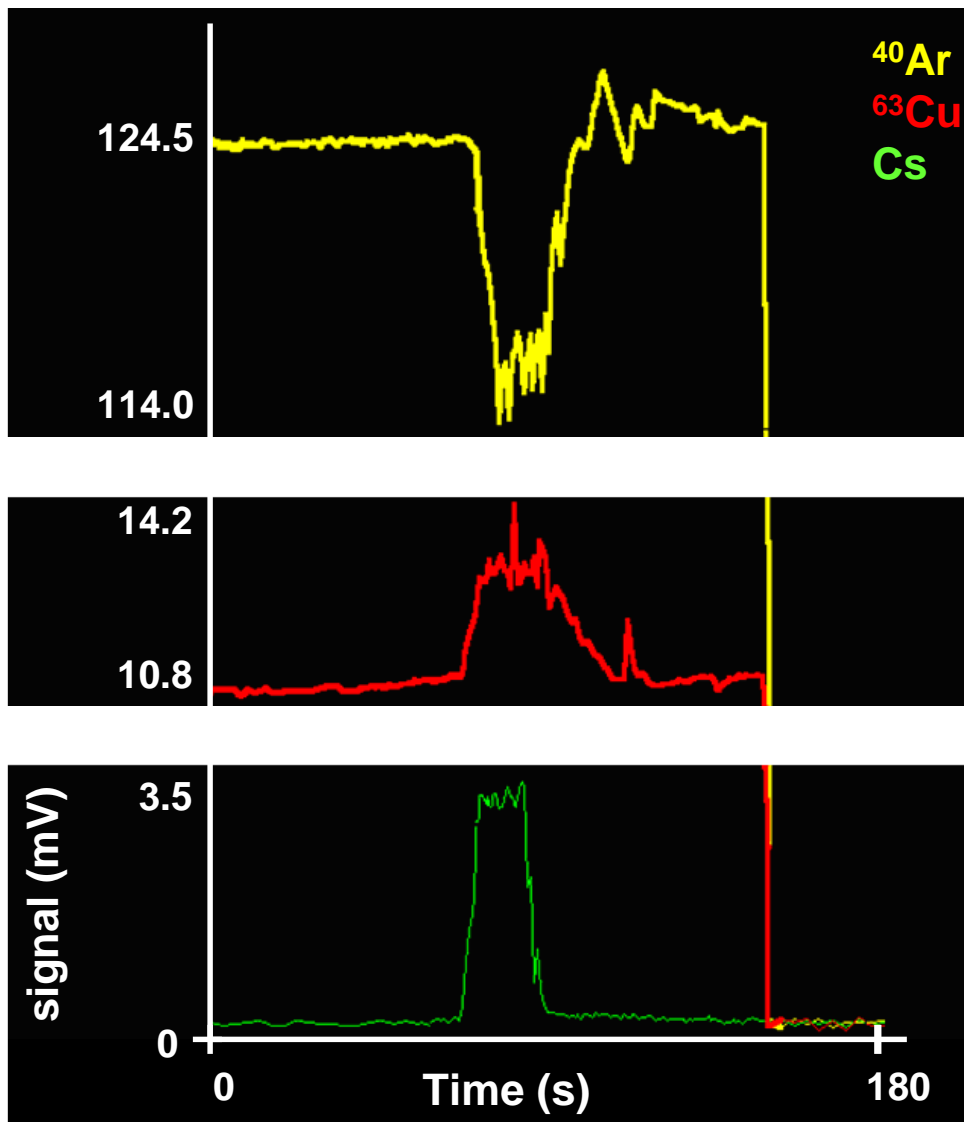


Figure 4-13. The effect of particle introduction on argon and copper ion signals: A package of particles is nebulized to the plasma will result in a decrease of argon ion, while it increases the copper signal. At $t = 150$ s, the discharge is turned off.

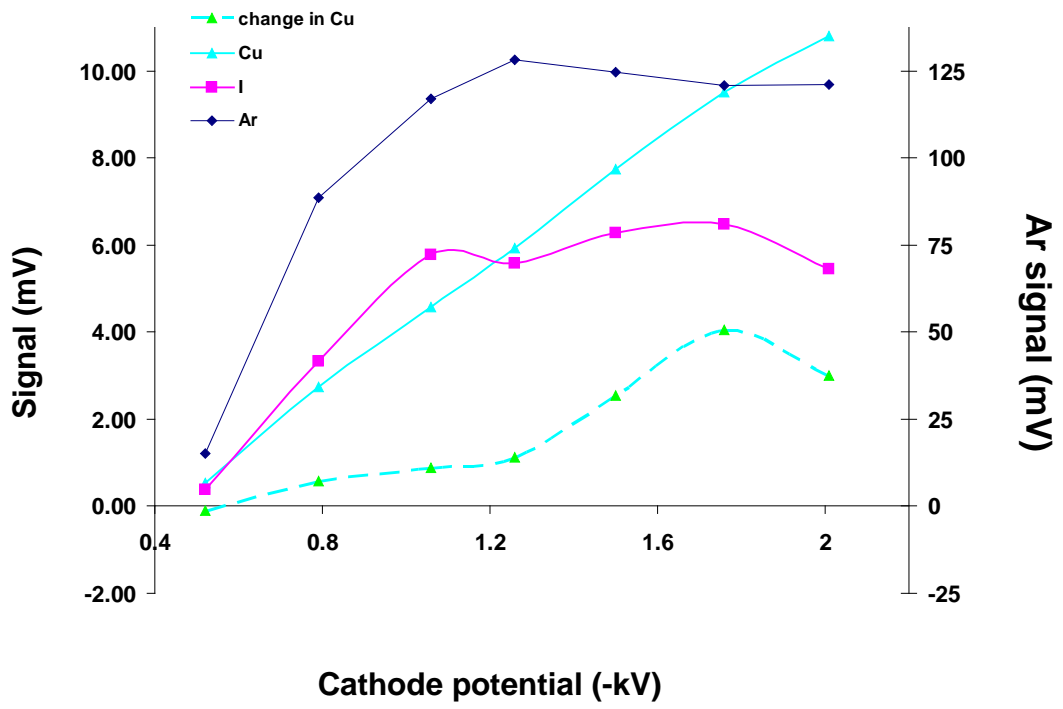


Figure 4-14. Comparing the effect of cathode potential on different ion signals.

CHAPTER 5
PULSED GRIMM GLOW DISCHARGE TIME-OF-FLIGHT MASS SPECTROMETRY
STUDY OF AEROSOLS GENERATED BY LASER ABLATION OF SOLID SAMPLES

Introduction

The field of inorganic mass spectrometry deals with the elemental analysis of solid and liquid samples. Inductively coupled plasma mass spectrometry (ICP-MS) is the most common way for elemental analysis of inorganic solutions. However, solid samples are harder to analyze. These samples must first go through sample preparation and dissolve in proper solvent before being introduced into the ICP-MS. Sample preparation is usually time consuming and a method that allows for direct analysis of solids is desirable. In the past decades, techniques such as spark source mass spectrometry (SSMS), glow discharge mass spectrometry (GDMS), secondary ion mass spectrometry (SIMS) and thermal ionization mass spectrometry (TIMS) were used as methods of choice for direct solid analysis.⁸⁴

In recent years, the high sensitivity of ICP-MS along with the advances in laser technology have led to development of Laser Ablation Inductively Coupled Plasma Mass Spectrometry (LA-ICP-MS). This technique has become a very popular analytical technique for element- and isotope-selective analyses of solid samples such as geological, archaeological, environmental and even biological matrices.⁸⁵ This is due to the simplicity and versatility of this technique for solid samples, since there is no need for time consuming sample preparations as needed for traditional ICP methods.⁸⁶

Although GDMS is another common plasma source that has been employed for solid analysis, less work has been done that combines laser ablation with GDMS. This is due to the fact that ICP is a much more powerful plasma that can reach higher sensitivity and lower limits of detection. In the work, presented in this chapter the objective is to understand more about the

fundamentals of particle interaction with our pulsed discharge plasma, and laser ablation can therefore provide a potential pulsed source of particles for this purpose.

Glow Discharge and Lasers

Laser Ablation coupled with Inductively Coupled Plasma Optical Emission Spectroscopy (LA-ICP-OES) or Mass Spectrometry (LA-ICP-MS) are well-established techniques of chemical analysis. Many of the articles, which include both concepts of glow discharge and laser, are about the application of a laser beam for the purpose of plasma diagnostics.¹⁰⁰ On the other hand, few reports are found describing the coupling of Laser Ablation with Glow Discharges (LA-GD).⁸⁷⁻⁹¹ Most of these articles use Optical Emission Spectroscopy (OES), as opposed to Mass Spectrometry for detection of the resulting ions/atoms.⁸⁸⁻⁹⁰

In addition, in almost all the aforementioned GD-laser studies, the laser interacts with the sample within the glow discharge chamber.⁸⁷⁻⁹¹ Indeed, in many of these cases, the sample itself is the cathode of the glow discharge. For example, the polarity of a Grimm-type glow discharge was reversed to have a hollow cathode formed by the anode of the Grimm source, now acting as cathode.⁸⁹ Then a Nd: YAG laser at 1064 nm and 1 kHz (0.76 mJ / pulse) was used for laser ablation of a sample of stainless steel placed as the cathode (anode considering the reverse phase) of the discharge. The steel sample was directly ablated into the plasma and analyzed by OES. In another study, King *et al.* used a pulsed glow discharge source as an auxiliary for excitation of ablated copper that was the cathode of the discharge as well.⁹⁰ The ablated material was studied by means of OES. In a recent paper by Gunther *et al.* LA-GD-TOFMS was introduced and investigated to evaluate the analytical capabilities of this technique.⁸⁷ Although in part of this work, the ablation sample was not the cathode itself, the experimental set up was different from that of a typical LA-ICP. The sample and the pulsed (2 ms) hollow cathode discharge were both placed in a low pressure chamber, from which ions are extracted towards the

mass spectrometer. The closest analog to LA-ICP-MS is a recent work in which an atmospheric helium GD was used to detect laser ablated organic compounds such as caffeine and acetaminophen.⁹² To our knowledge, the study of the transfer of laser ablated metallic aerosols from an external ablation cell into a pulsed GD-MS has not yet been reported.

LA-ICP-MS

As mentioned above, the field of LA-GD-MS is not yet fully investigated by scientists. Due to this lack of literature resources for LA-GDMS, some of the principles of LA-ICP-MS, the closest field that has been studied extensively, will be discussed here. It has been shown that experimental parameters, such as the laser wavelength, energy and pulse width of the laser, the geometry of the ablation cell, the cell carrier gas, the particle transport efficiency and its atomization in the ICP plasma have an impact on the analytical performance of LA-ICP-MS.⁹³

Ideal LA-ICP-MS System

An ideal laser ablation ICP-MS system must have three characteristic components:⁹³

- The ablated particles have the same overall composition as the sample itself.
- The transport efficiency of aerosols is 100%.
- The particles will go through complete atomization and ionization in the plasma source without affecting the plasma parameters.⁹³

Fractionation

However, the challenge of LA-ICP is performing fractionation-free analysis without the necessity that sample and standards' matrices have to match.⁹⁴ Therefore, only matrices that have variety of standards to provide a matrix-matched calibration graph, can be analyzed by this method. Consequently, LA-ICP-MS can only be used to analyze samples like stainless steel, minerals and silicate glasses that have a range of available standards.⁹⁵

Particle Size Effect And Use Of Femto-Second Lasers

It has been shown that the use of femto-second lasers can reduce the effect of fractionation. This is because the aerosols generated by this type of laser are stoichiometric and exactly reflect the composition of the sample itself.^{95,96} The aerosols generated by laser ablation usually include particles that vary in size, and cover a wide range of diameters from as small as 10nm to larger particles of a micron. The resulting particles have different chemical composition based on their size. In other words, a source of fractionation could be due to the fact that the particles of different size have different composition and also different transfer efficiency. As a result the particles of a specific size that will transfer the most will influence the result of analysis the most. However, these particles might have a chemical composition that does not necessary represent the bulk of the sample.⁹⁷

Particle transport efficiencies of up to 80% have been reported using femto-second lasers and helium as carrier gas.⁹⁸ This was done by particle impacting and measuring the weight loss in the sample. However, in order for this technique one must be able to neglect the re-deposition of particles on the sample surface, which might be a good approximation with helium but not with argon.^{86,99,100}

Carrier Gas of Choice

Helium is usually the carrier gas of the choice and results in better accuracy and sensitivity when compared to argon.⁸⁶ This is in part due to the higher ionization energy of helium. The plasma breakdown and shielding is less intense for helium which reduces the propagation of material in the horizontal mode (as opposed to vertical mushroom cloud mode) and less sample re-deposition on surface occurs in case of helium.⁹³ However, argon is easily available and cheaper. In addition, argon has lower ionization energy, and it requires a lower potential to form a discharge plasma. In our pulsed glow discharge system, the introduction of helium resulted in

total suppression of the discharge and the maximum possible potential delivered by our pulsed supply could not ignite a stable plasma discharge.

Laser Pulse Duration

Short laser pulses interact with the sample directly, while longer pulses can result in heating the plasma.⁹³ This can increase the electron density, which will reduce laser sample interaction. As a result, the mass removal efficiency will decrease. This phenomenon is more pronounced at higher laser fluence. Another drawback of longer laser pulses is the possibility of melting that can result in fractionation.⁹³ In order to reduce this fractionation, it is recommended to focus the laser below the surface of the sample to reduce laser fluence.

Experimental

The experimental setup is very similar to that of Chapter 3, only the source of aerosol has changed; instead of an ultrasonic nebulizer-dehydrator for particle generation, laser ablation of solid samples is the source of aerosol. Figure 5-1 shows the overall experimental setup for laser ablation glow discharge mass spectrometry. The laser pulse ablates the sample in the ablation cell from which the generated aerosol is transferred by the flow of argon into the discharge plasma. The needle valve is located before the ablation cell to break the pressure from atmospheric to low pressure. The pressure of the ablation cell is about 20 torr, while the discharge pressure is 12 torr. The glow discharge geometry used is the anode B geometry from Chapter 3, and mass spectrometer and discharge parameters are similar to those values used in the previous chapter unless otherwise noted. For a majority of the experiments, the optimum condition listed in Table 3-1 was used. The TOF detector was connected to a 500 MHz digital oscilloscope (TDS-724D, Tektronix Inc., Beaverton, OR) to obtain mass spectra with larger signal to noise ratio compared to the spectra collected by the instrument software.

Ablation Cell

The ablation cell was machined from aluminum in three parts (Figure 5-1). Figure 5-2 also shows the geometric dimensions of the cell. The laser beam goes through a lens (focal length = 55 mm) and then enters the cell through a quartz window at the top of the cell. The sample is machined to the shape of a disc with a diameter of 12 mm and thickness of 10 mm, and its surface is located 20 mm below the quartz window. The surface of the sample is 3 mm above the center of the argon inlet which has a 5 mm diameter. The center of the argon outlet is slightly higher than the argon inlet so that it is at the same height as the sample surface. The overall cell volume is 10.3 cm³. This volume includes the volume of argon inlet and outlet but not that of the transfer tubing. At 10 mm below the quartz window, the cell narrows down to form an edge to provide support for additional thin samples or quartz windows. This can be used for the purpose of laser induced forward transfer of thin films into the ablation cell.

Lasers

Two different lasers were employed for sample ablation. The first one was a passively Q-switched, diode-pumped Power-chip laser (JDS Uniphase, Santa Rosa, CA). This laser is a solid state Nd: YAG laser that operates at 1064 nm with pulse repetition frequency of 1 kHz. The pulse width of the laser is 500 ps with 50 μJ pulse energy. The other laser was a Q-switched, flashlamp-pumped Nd:YAG laser (Big Sky Laser Technologies, Bozeman, MT). This laser has variable frequency of 1, 2, 5, 10 and 20 Hz, temporal pulse length of 5 ns and maximum energy of ~75 mJ/pulse). The laser probe was set on a stand perpendicularly to aim at the top window of the ablation cell. The stand was also set on an XYZ stage, allowing for minuscule movements of the laser probe in the XY direction. The lens (focal length = 55 mm) is supported on the same stand as the laser probe, and as a result, will move along with the laser beam. This way, the ablation spot could be moved on the sample's surface without moving the ablation cell, which is

constrained by tubing that connects it to the discharge source. The laser beam was focused 3 mm below the sample surface to minimize fractionation.

Materials

Commercially available samples of stainless steel, bismuth alloy, aluminum, brass and Macor were machined into small discs. Table 5-1 shows the chemical composition of these samples. For generating salt particles, a mixture of desired salt (for example CsI) and a buffer salt (for example NaCl) was ground as finely as possible and the resulting mixture was pressed into a disc and placed into the cell for ablation.

Results and Discussion

In order to compare the efficiency of the two lasers in laser ablation, both lasers were utilized at their maximum power on a stainless steel sample, and the iron signal at $m/z = 56$ was monitored. When the Power-chip laser was used, no detectable iron signal was observed using the instrument's software. However, when the detector of time-of-flight mass spectrometer was directly connected to the oscilloscope, due to reduction of background noise, a very small iron peak appeared at $m/z = 56$. The resulting mass spectrum is depicted in Figure 5-3. When the flashlamp-pumped Nd:YAG laser (20 Hz) was used, the iron signal was significantly stronger than that of the Powerchip laser (~15 times), and was also detectable with the instrument's software. Thus, the flashlamp-pumped Nd:YAG was used throughout the rest of the experimentation. Figure 5-4 shows the mass spectrum resultant from ablation of stainless steel by the flashlamp-pumped Nd:YAG laser. As is shown in Figure 5-4 in addition to a large ^{56}Fe signal ions of ^{52}Cr , ^{53}Cr , ^{54}Fe (overlaps with ^{54}Cr), ^{57}Fe , ^{55}Mn , ^{58}Ni and ^{60}Ni were detected as well.

To investigate the stability of aerosol generation by Nd:YAG laser, the stainless steel sample was ablated for ~240 seconds, and the ^{56}Fe signal was monitored by time. The results shown in Figure 5-5 indicate acceptable signal stability with relative standard deviation of 10%.

Laser frequency, glow discharge frequency and integration time for detector of the time-of-flight were 10 Hz, 400 Hz, and 500 ms, respectively. As was expected, the particles generated by the Nd:YAG laser provided a continuous source of aerosol for the mass spectrometer. This is due to broadening of the particle package generated by each laser pulse during aerosol transport from the ablation cell to discharge. This broadening is clearly demonstrated in Figure 5-6, when laser frequency of 1 Hz and integration time of 10 ms was used. At this low laser frequency, individual signal pulses from each laser shot could be detected. The width of each particle package at the discharge source was about 150 ms. This indicates that for a laser frequency of 10 Hz or higher, these packages of particle will start to overlap and provide a continuous flow of aerosol into the glow discharge.

Similar behavior was also observed for bismuth alloy. Figure 5-7 shows an experiment in which bismuth alloy was ablated for ~10 seconds. The laser frequency and glow discharge frequency were 5 Hz and 400 Hz, respectively. The integration time of detector was 5 ms in order to see the particle profile with higher resolution. As can be seen, the individual pulses can still be resolved at the maximum of each pulse. However, the bases of each pulse (a package of particle) broaden and merge into each other. At higher frequencies (10 and 20 Hz), no individual particle package (due to a single laser pulse) can be detected, and a continuous signal is observed. At 1 Hz, however, each laser pulse can be completely resolved.

When the laser is employed at a frequency of 5 Hz, the particle packages are at the threshold of merging into each other. As a result, the signal vs. time for such frequency will present borderline characteristics between a continuous and pulsed source of aerosol (Figure 5-7). This shows that at laser frequencies of 10 Hz or higher, there is no need to synchronize the

laser and discharge pulses with respect to each other as the particle flow into the discharge is continuous and not pulsed.

Figure 5-8 shows the result (Cu and Fe signals vs. time) for laser ablation of stainless steel for ~12 minutes. The ablation spot was not moved during this experiment, and interestingly, the sample was able to provide a relatively stable source of aerosol from the same spot during this experiment. At the very beginning of ablation, the signal had a slight reduction (in the first minute) and then remained stable for about 9 minutes (to the 10th minute). Figure 5-9 also shows the ^{56}Fe , ^{63}Cu and ^{64}Zn peaks for four different time zones in this experiment. The early reduction in both Cu and Fe signals could be due to the change in the nature of the cathode and plasma due to introduction of particles, which will reach a steady state after the first minute. After about 10 minutes, the iron signal started to decay along with the copper signal. However, after the laser ablation ceases, the copper signal (resulting from the sputtering of the cathode) becomes stable. Figure 5-10 shows that the iron to copper signal ratio is very stable, and the decay of the copper and iron signals are related to each other. This means that the decay in both iron and copper signals is due to contamination of the cathode and plasma as a result of particle introduction that changes the nature of the discharge and the quality of the plasma. This is not a surprising phenomenon, as the glow discharge cathode requires regular cleaning, even without the introduction of particles. However, as a result of particle introduction, more frequent cleaning of the cathode is required.

Figure 5-11 also shows the copper signal vs. time where a sample of brass was ablated for a period of ~30 seconds, followed by a time lapse of ~20 seconds in which the particle introduction was halted, and then resumed for another ~10 seconds. The origin of the primary ^{63}Cu ion signal is the sputtering of the brass cathode. Every time the brass sample was ablated,

there was a boost in ^{63}Cu signal, which represents the contribution of brass particles in providing copper ions. It is interesting to note that the standard deviation of the signal increases as a result of particle introduction. However, after the termination of particle flow, the copper signal returns to its previous state without any significant perturbation.

Ablation of Different Materials

The Nd:YAG laser was used to generate aerosol from different samples. Figure 5-12 shows the resulting spectrum for Macor. Peaks for silicon, aluminum and magnesium were detected. However, no signal for fluorine or boron was observed. This is due to high ionization energy of fluorine and boron. A peak for potassium at $m/z = 39$ was expected; however, for some unknown reason, no significant potassium peak was detected. Only at higher resolution and with the oscilloscope was a small ^{39}K signal detected.

Figure 5-13 shows the result of LA-GD-MS for bismuth alloy. The peaks for bismuth ions ($m/z = 209$), lead ions ($m/z = 206, 207, \text{ and } 208$), cadmium ions ($m/z = 110, 111, 112, 113, 114, \text{ and } 116$) and tin ions ($m/z = 112, 114, 116, 117, 118, 119, 120, 122 \text{ and } 124$) were observed. It is important to note that $m/z = 112, 114 \text{ and } 116$ are common to both cadmium and tin. Isotopes $m/z = 106 \text{ and } 108$ for cadmium, and $m/z = 115$ for tin are not detected due to low isotopic abundance. Three samples of salt pellets with different CsI percentages (7.65%, 16.42% and 20.16%) in an NaCl matrix were prepared. The Cs signal vs. CsI molar percent resulted in a linear relationship, which is depicted in Figure 5-14.

Relative Signal Intensities for Different Matrices

A list of relative intensities for different elements in these samples can be found on Table 5-2. Bismuth alloy resulted in the highest sensitivity, due to the low heat of vaporization of lead and bismuth, while Macor resulted in a lower sensitivity due to high heat of vaporization of this material. The ionization energies of the elements in the bismuth alloy are also lower than those

of Macor elements. In addition to heat of vaporization, higher atomic weights of bismuth and lead are also important factors in their higher sensitivities (Chapter 4). Figure 5-15 shows the particle size distribution for these materials. The lower sensitivities for aluminum, Macor, and salt pellets could be explained by the higher D_V values of these particles (Table 5-3).

The Effect of Cathode Potential on Particle Ionization

The effect of cathode potential on the ionization of stainless steel particles is shown in Figure 5-16 and compared to the copper signal that originates from the brass cathode. As expected (Chapter 4), the copper signal is almost a linear function of cathode potential. However, interestingly, the iron signal reduces as cathode potential increased. This phenomenon can be explained by considering the small mean volume diameter of stainless steel particles (200 nm). The particles are so small that even a low cathode potential is enough to ensure their complete vaporization. Any further increase in cathode potential will result in reducing the length of the cathode dark space. Consequently, particles will spend a shorter time in this high energy region, which can reduce the vaporization efficiency. A more important explanation for the decay of the iron signal is the increase in the electric field by increasing the cathode potential. It was previously mentioned in Chapter 3 that the electric field of the cathode dark space can significantly suppress the ion transfer out of this region.

Figures 5-17 and 5-18 show the effect of cathode potential on Macor and salt particles. It can be seen that for these larger particles that are also harder to evaporate, the cathode potential behavior is similar to that of salt particles generated by an ultrasonic nebulizer-dehydrator. The particle signal increases by cathode potential at first; as the cathode potential increases further, the signal starts to decline. This difference from the stainless steel behavior can be explained by the larger diameter of Macor and salt particles ($D_V \sim 700$ nm).

Crater Shape in Bismuth Sample

Figure 5-19 shows the crater image for the ablation of bismuth alloy obtained by optical microscope. The crater diameter was measured to be 1.1mm, and the depth of the crater was estimated to be 500 μm . In another experiment, 219 laser shots (at maximum pulse energy) were used to ablate another crater. The crater profile shape and dimension were measured by an optical profilometer. Figure 5-20 shows the result for this experiment. The diameter of the crater was about 1000 μm on top in agreement with what was measured by optical microscope (Micromaster, Fischer Scientific). However, the diameter at the bottom of the crater was only 400 μm . The crater depth was 50 μm . Considering a cylindrical shape for the crater and using average of 700 μm for its diameter, a crater volume of $1.92 \cdot 10^{-5} \text{ cm}^3$ was calculated. Considering density of the bismuth alloy (9.37 g/cm^3) will result in mass removal of 0.82 $\mu\text{g/pulse}$ for the bismuth alloy.

Effect of Laser Pulse Energy

As the laser pulse energy was increased from 1 to 10, both bismuth and lead signal increased as expected (Figure 5-21). However, the increase in signal for lead had a higher rate than that of bismuth. Figure 5-22 shows the Bi to Pb signal ratio at different laser pulse energies. This is an example of the effect of laser fluence on fractionation.

Investigation of Particle Ionization Mechanism

In the previous chapters, we discussed some evidence that showed particles are ionized in the cathode dark space of the glow discharge plasma, as opposed to cathode sputtering of particles deposited on the cathode. In order to eliminate the possibility of the ionization of particles from the cathode surface, an experiment was devised. In this experiment, the bismuth sample was ablated for ~30 s (305 shots) while the glow discharge source was off. Then the laser

ablation was stopped and the glow discharge plasma was initiated. Figure 5-23 shows the bismuth signal vs. time for this experiment. Only a small spike in the signal was observed at the beginning of plasma initiation. This signal is much lower than the signal observed during previous experiments in which the alloy was ablated into the plasma while plasma was on. In other words, only a small portion of the signal results from the particles that are deposited on the surface of the cathode. It's also important to note that no signal was observed when only the laser was operating without the discharge plasma glowing. This means that no ions generated by laser plasma can reach a detector of TOF. In another experiment, a 200 μm filter (porous metal disc with pore diameter of 200 μm) was placed between the laser ablation cell and the plasma source while both laser and plasma were on. The presence of the filter resulted in no iron signal. This shows that no atomic vapor from the sample is transferred to the discharge, and the majority of the material is transferred in the form of particles.

Laser Back Ablation of Thin Films

After ablation of bismuth sample during few experiments, it was observed that a very thin film of material is formed on the quartz window. As Figure 5-24 shows, this is a very minute amount of deposition that might not even be considered a film. A closer investigation of the window shows that parts of this deposited material are removed by the laser beam from the center of the window. This is shown in Figure 5-24 by zooming into the center of the quartz window where the laser beam passed through. This is an evidence for laser back induced forward transfer of material.

As mentioned in the experimental section, the ablation cell was designed in a versatile way so that it can accommodate another quartz window or a thin film for laser back ablation studies (Figure 5-25). The secondary quartz window was spiked with a few micro liters of CsI solution

and placed on the ablation cell. The back ablation of CsI was investigated. Although there was physical evidence for the removal of some CsI from the window, no Cs signal was detected. In another experiment, a tape with a thin layer of copper (5 μm) was placed on the surface of the quartz window. Although the laser beam clearly removed the copper layer from the surface of the tape, no increase in copper signal was detected. It is then conceivable that the laser back ablation of aforementioned samples does not provide the appropriate amount of aerosol for detection.

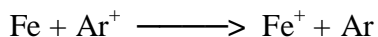
In another experiment, a thin, circular stainless steel film was affixed in place of the quartz window (Figure 5-26). The laser was operated at maximum energy and frequency (20 mJ and 20 Hz), and the iron signal was monitored as a function of time. In order to distinguish between laser back ablation and regular ablation, a pure aluminum sample (more than 99 % Al) was placed below the stainless steel film in the usual sample position, and aluminum and iron signals were monitored. Figure 5-27 shows that for about the first thousand laser shots, no signal for either aluminum or iron was observed. The aluminum signal appeared after 1,002 shots, and continued until the laser beam was terminated. This shows that after 1,002 laser shots, the stainless steel film has been penetrated and the beam reaches the aluminum. It was interesting to see that a small iron signal appeared a few shots before occurrence of aluminum signal. This iron signal started to decay immediately after the aluminum signal appeared.

One explanation could be that right before complete penetration of the laser through the stainless steel, laser back ablation of the remaining thin layer of stainless steel has occurred. Another explanation might involve the transfer of iron particles from the sides of the crater in the stainless steel through a small hole at the bottom of the crater. Another experiment is required to evaluate the validity of these explanations. In this experiment, the ablation must be terminated

immediately after the appearance of iron signal, and then the stainless steel must be examined for existence of any hole at the bottom of the crater. Figure 5-28 shows the hole in the stainless steel film, and the crater on the aluminum sample.

Effect of Laser Ablation and Particle Introduction on Other Discharge Species

When the stainless steel was ablated and particles entered the glow discharge, it caused a minor decline in argon signal while copper and argon hydride signals increased. Figure 5-29 shows an increase in copper signal upon ablation of stainless steel by a single laser shot. Figure 5-30 also shows the increase in copper signal as a package of stainless steel particles produced by a laser frequency of 10 Hz enters the discharge for duration of ~20 seconds. The change in Ar and ArH signals is shown in Figures 5-31. The effect of particle introduction is negative and positive for Ar and ArH signals, respectively. As discussed in previous chapters, the increase in copper signal is due to increase in discharge pressure due to introduction and vaporization of stainless steel particles. The bombardment of the cathode by resulting iron atoms is another reason for increase in the sputtering of the cathode, and copper signal. The decrease in argon signal can also be explained by charge transfer reactions between iron atoms and argon ions. An increase in concentration of iron atoms after introduction of the particles in the negative glow will result in the following reaction:



Due to higher ionization energy of argon, this reaction is thermodynamically favorable and will decrease the population of argon ions.

Bismuth alloy ablation also reduces the argon signal for the same reason (Figure 5-32). However, as shown in figure 5-33, the copper signal does not change much in the case of the bismuth alloy. This can be explained by the fact that ionization energies of bismuth and lead (7.3 and 7.4 eV) are slightly lower than that of copper (7.7 eV). As a result introduction of this Bi-Pb

alloy will reduce the population of copper ions due to ion exchange reactions. Since the sputtering increase is still expected, overall there is not much change in copper signal.

The Macor particles decrease the argon ion population for a similar reason as did the stainless steel particles (Figure 5-34). However, unlike stainless steel, when Macor particles enter the discharge, they result in a reduction of copper signal (Figure 5-35). There could be a few explanations for this different behavior. First, Macor is a non-conducting material that can disrupt the function of discharge upon its introduction by contaminating the cathode surface. In addition, Macor particles are larger than stainless steel particles ($D_v = 900\text{nm}$ compared to 200nm), and have a higher enthalpy of vaporization. As a result, the vaporization of Macor particles is not complete, and less temporal increase in discharge pressure is caused by Macor when compared with stainless steel. Finally, the majority of ions generated by Macor particles (Si, Al, and Mg) have lower masses compared to atoms generated by stainless steel (Fe, Cr, and Mn), and heavier ions accelerated in the electric field of the CDS can sputter the cathode more efficiently.

Table 5-1. The chemical composition of sample material used in laser ablation in mass%.

Macor	Stainless steel	Bismuth alloy	Brass	Aluminum
SiO ₂ 46%	Mn 2%	Bi 50%	Cu 61.5%	Al 99%
MgO 17%	Si 1%	Pb 26.7%	Zn 35.4%	
Al ₂ O ₃ 16%	Cr 18-20%	Sn 13.3%	Pb 3.1%	
K ₂ O 10%	Ni 8-10.5%	Cd 10%		
B ₂ O ₃ 7%	Fe 71-66.5%			
F 4%				

Table 5-2. Relative intensities of particle ionization from ablation of different solid samples.

Sample	isotope	mole % of isotope	Signal	Normalized
Stainless steel	⁵⁶ Fe	61.6	40.3	65.4
Bismuth alloy	²⁰⁹ Bi	42.1	72.1	171.3
Macor	²⁸ Si	14.2	6.5	45.8
Aluminum	²⁷ Al	99	25	25.3

Table 5-3. Particle mean volume diameters (D_v) for aerosol generated by laser ablation of different samples. A particle size analyzer (Aerosizer LD, API Inc., TSI Inc, Shoreview, MN) was used for particle size distribution measurements.

Sample	D_v /nm
Stainless steel	180 ± 10
Brass	239 ± 10
Bismuth alloy	332 ± 12
Aluminum	908 ± 22
Macor	934 ± 35
Salt pellet	900 ± 15

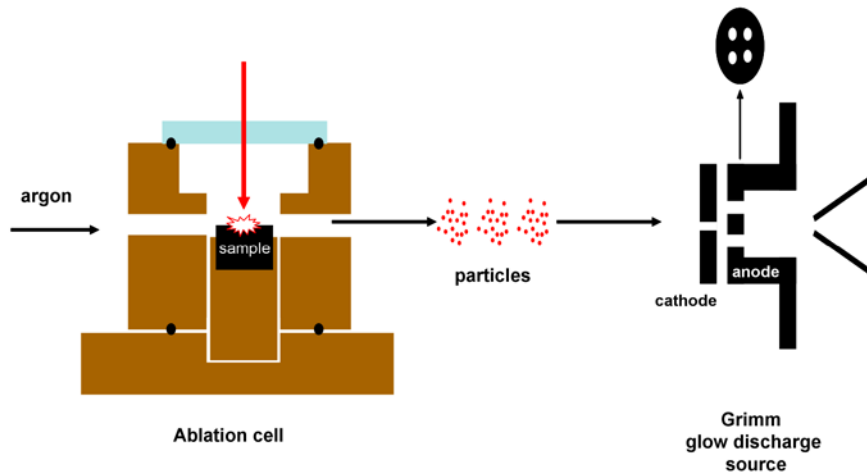


Figure 5-1. Overall experimental set up for LA-GD-MS. Only the skimmer of time-of-flight is shown.

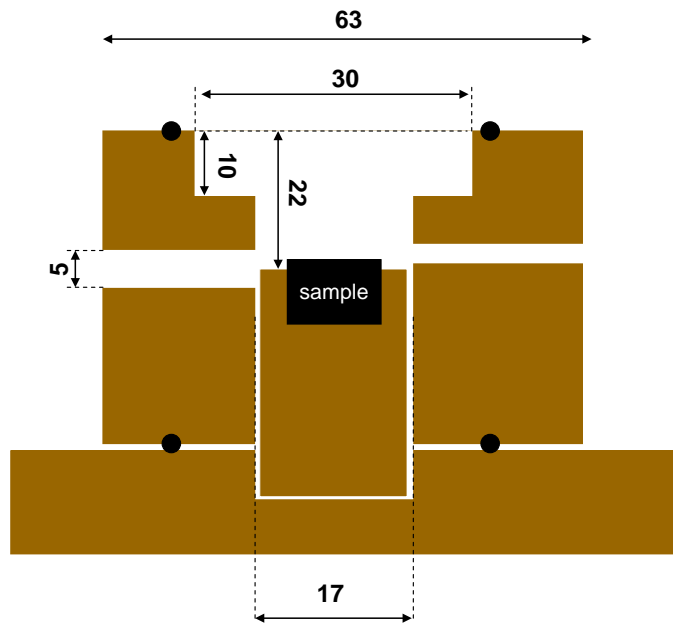


Figure 5-2. The geometrical dimensions of the ablation cell. All dimensions are in millimeters.

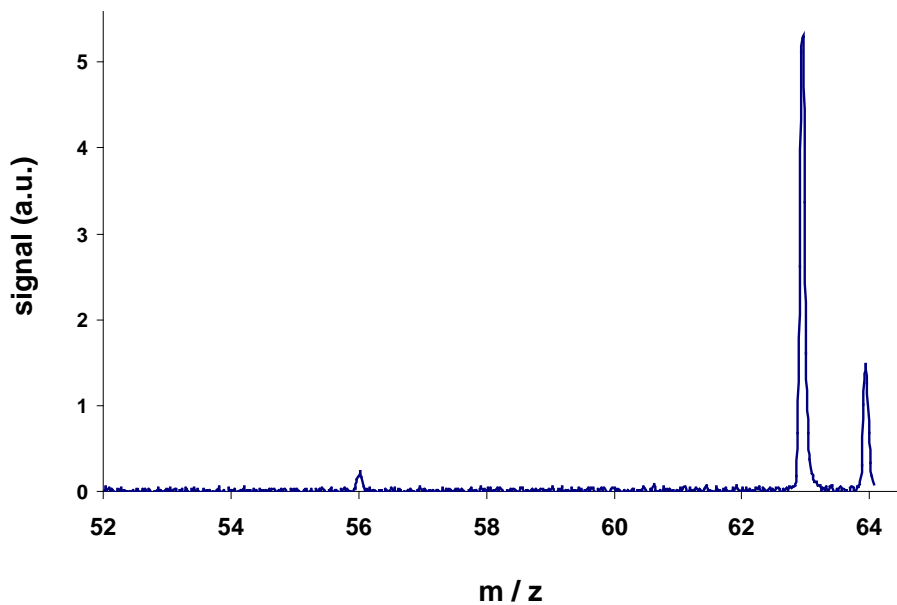


Figure 5-3. Iron signal resulted from ablation of stainless steel using power-chip Nd:YAG laser. Cathode potential = 1.75 kV. The peaks at $m/z = 63$ and 64 are the ^{63}Cu and ^{64}Zn from the brass cathode.

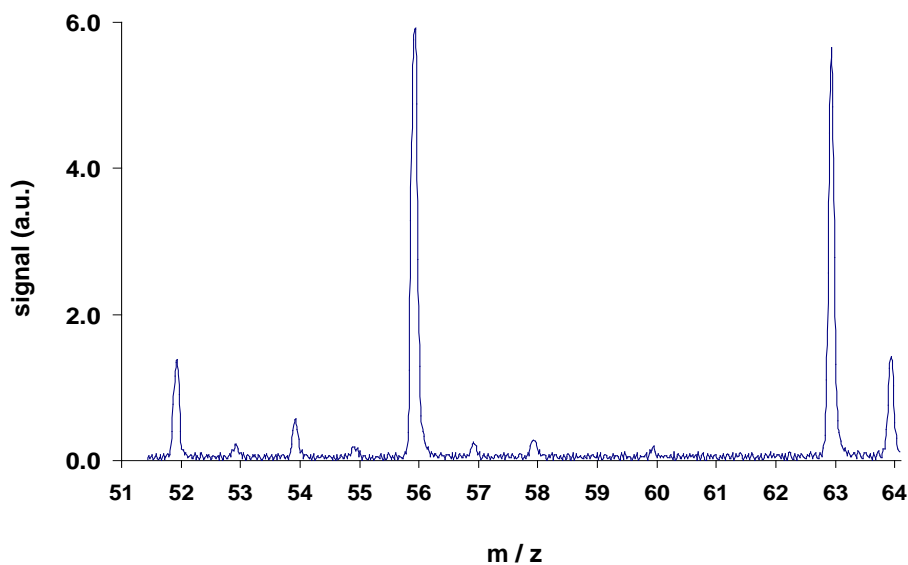


Figure 5-4. Mass spectrum resulted from ablation of stainless steel using the Q-switched, flashlamp-pumped Nd:YAG laser at its maximum pulse power. Cathode potential = 1.75 kV. The peaks at $m/z = 63$ and 64 are the ^{63}Cu and ^{64}Zn from the brass cathode.

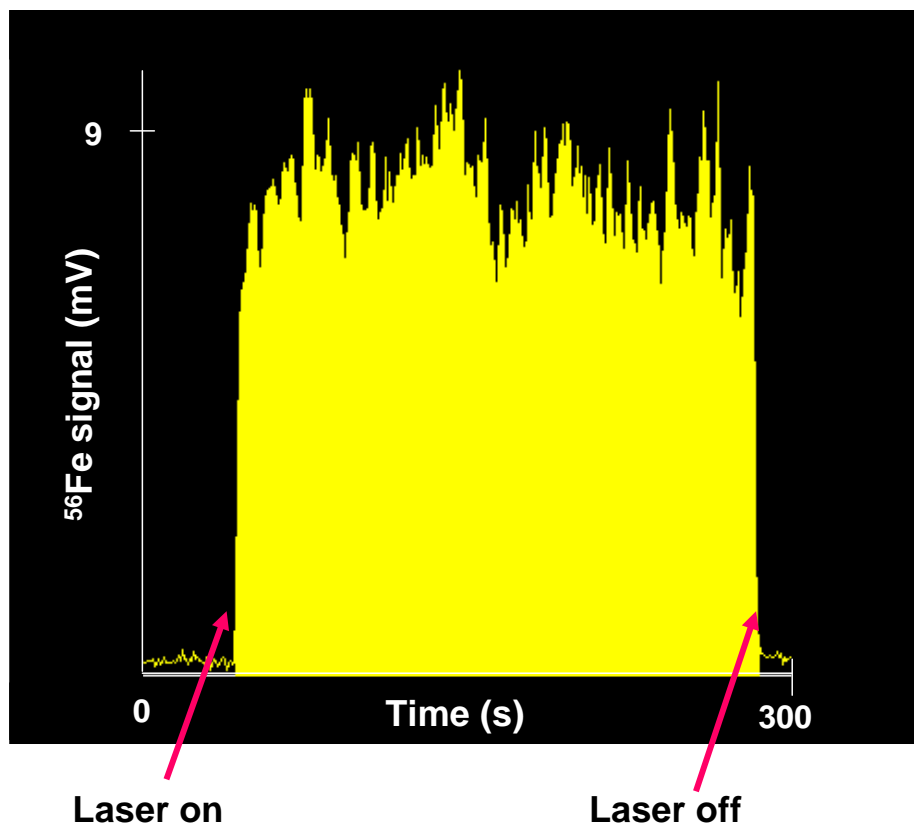
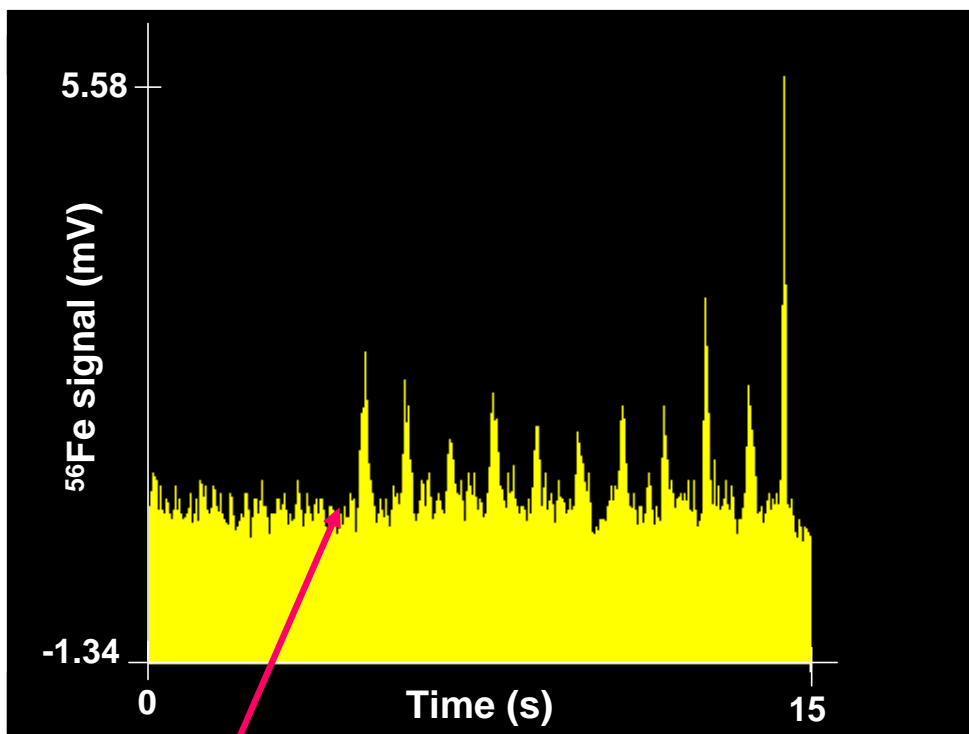


Figure 5-5. Monitoring the ^{56}Fe ion signal as a function of time for 300 seconds. Laser ablation of stainless steel was performed for 240 seconds of the time. Cathode potential = 1.75 kV, Laser frequency = 10 Hz, Integration time = 500 ms



Laser on

Figure 5-6. Monitoring the ^{56}Fe ion signal as a function of time for ablation of stainless steel using 11 single laser shots. Cathode potential = 1.75 kV, Laser frequency = 1 Hz, Integration time = 10 ms

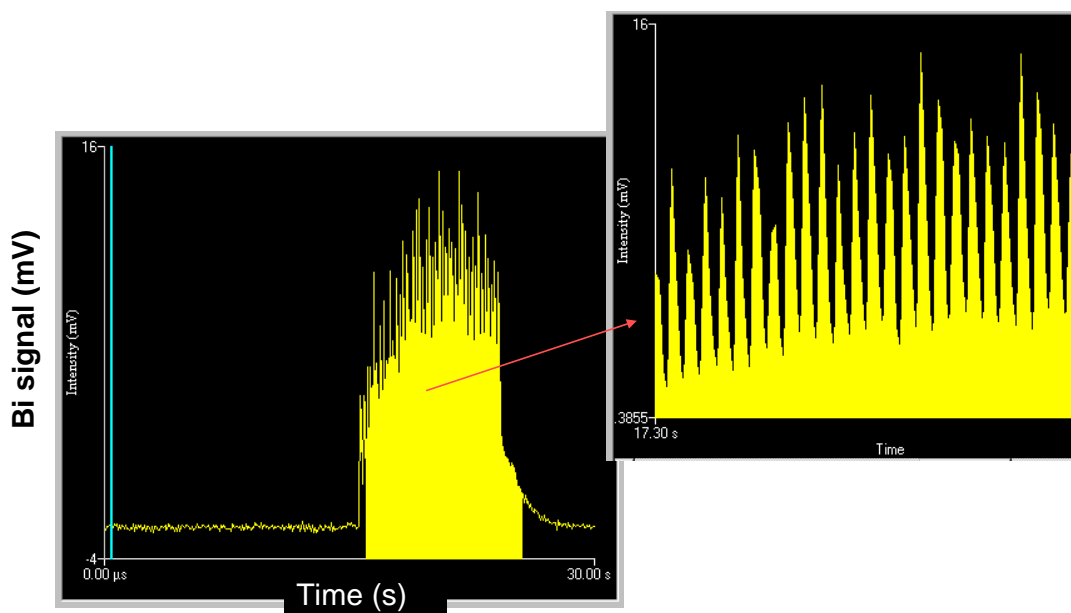


Figure 5-7. Monitoring the ^{209}Bi ion signal as a function of time for laser ablation of bismuth alloy. Cathode potential = 1.78 kV, Laser frequency = 5 Hz, Integration time = 50 ms

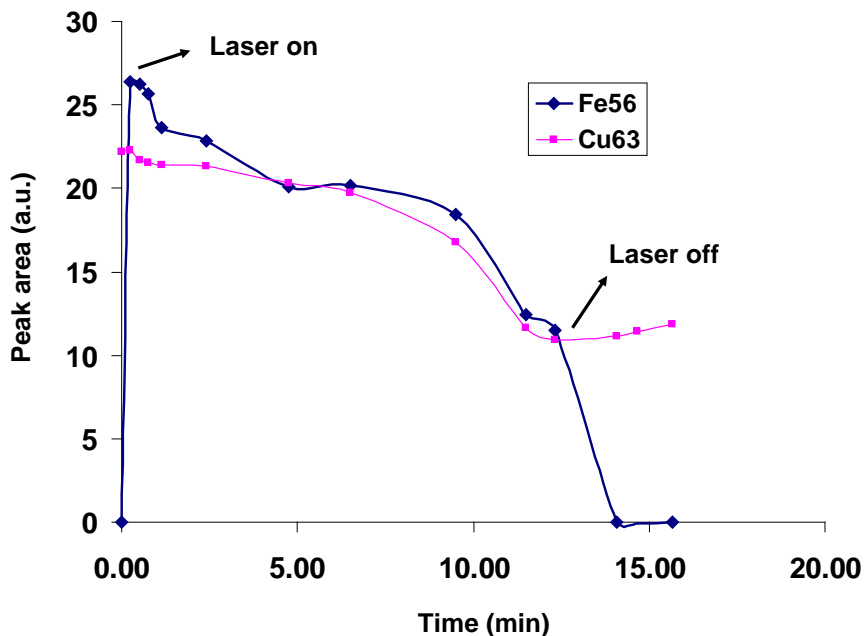


Figure 5-8. Monitoring the ^{56}Fe and ^{63}Cu ion signals as a function of time for approximately 13 minutes of stainless steel ablation. Cathode potential = 1.75 kV, Laser frequency = 10 Hz, Integration time = 500 ms

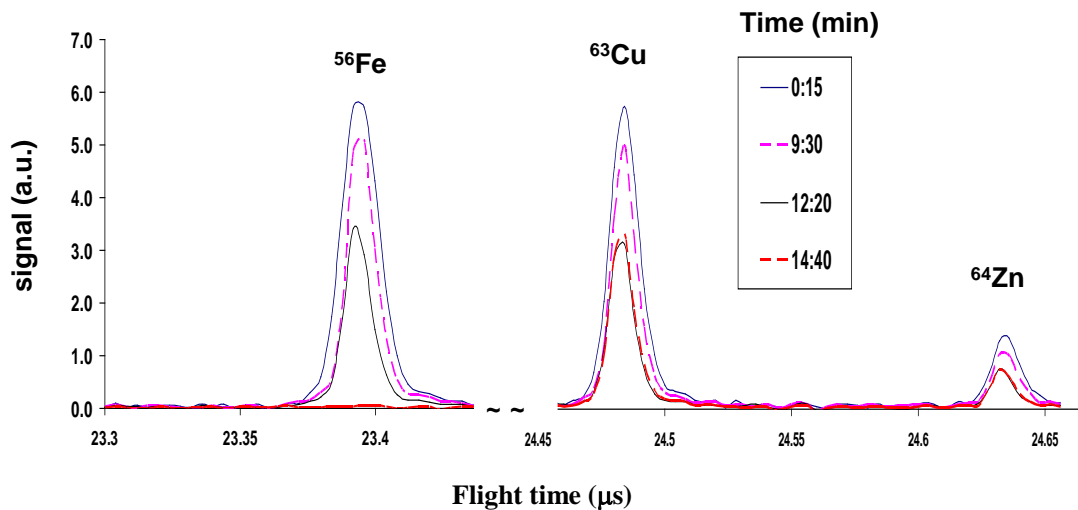


Figure 5-9. Iron, copper and zinc ion signals, at 4 different time domains. The laser is turned off at $t = 13$ min. The x axis shows the flight time instead of the m/z .

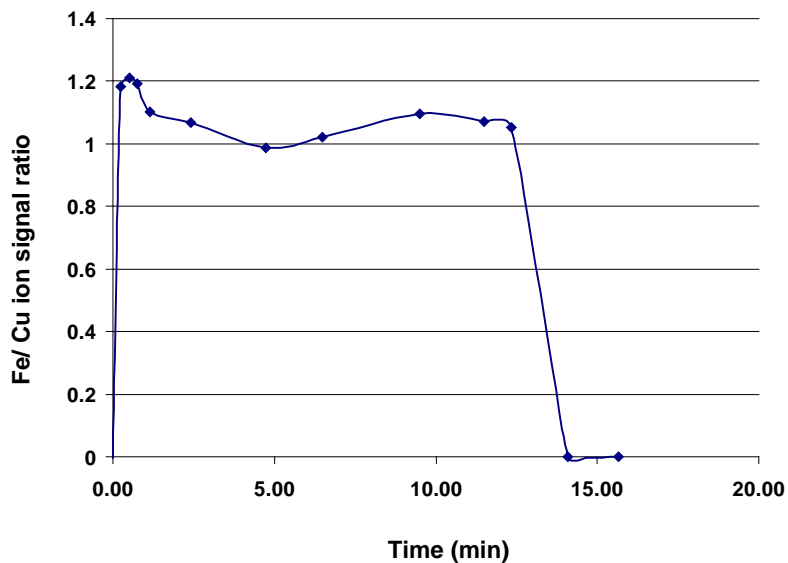


Figure 5-10. The signal ratio for ^{56}Fe to ^{63}Cu , almost remains constant for the 13 minutes duration of laser ablation.

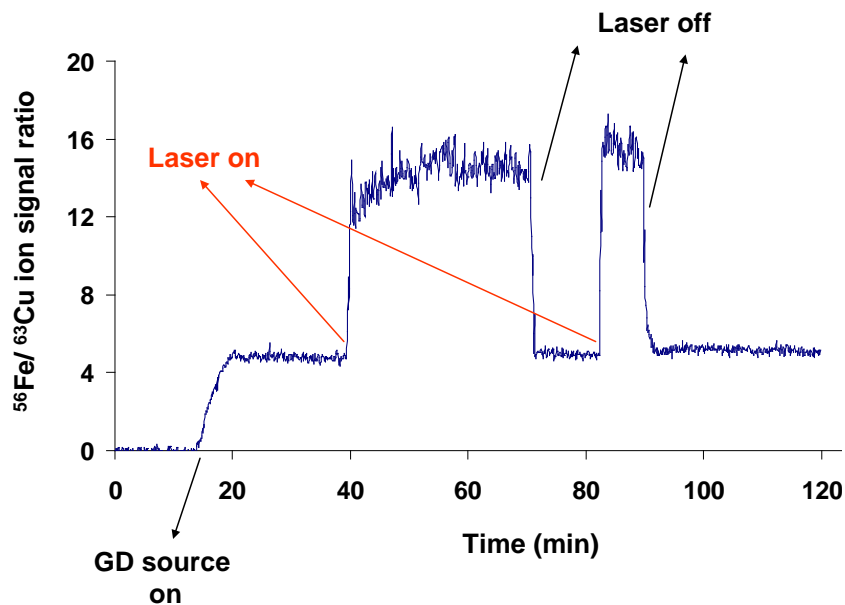


Figure 5-11. The cathode signal from sputtering the brass cathode increases due to ablation of a brass sample.

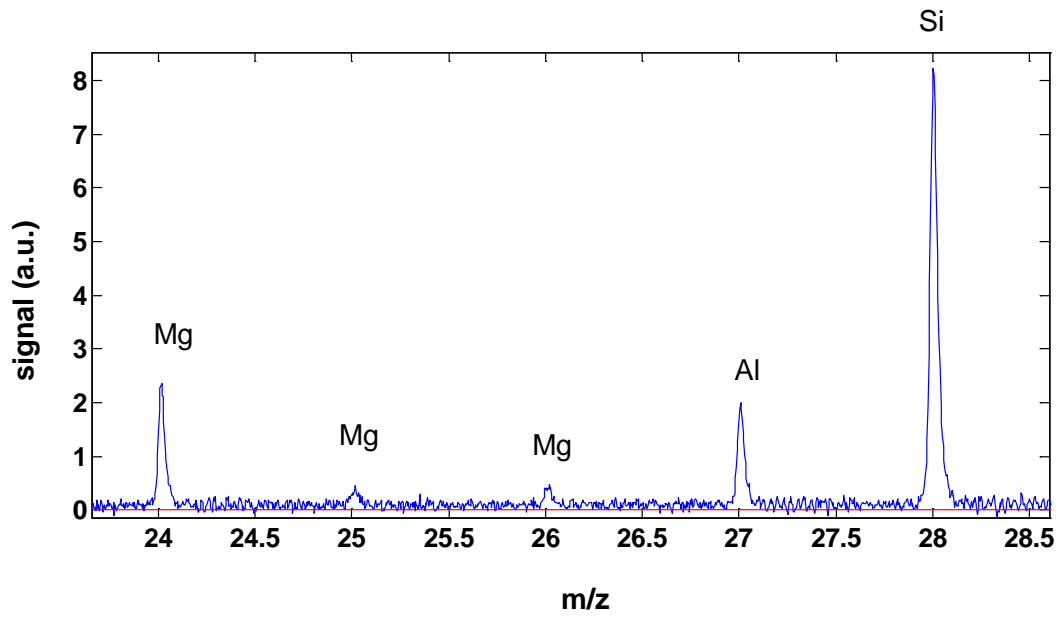


Figure 5-12. Mass spectrum from laser ablation of a Macor sample.

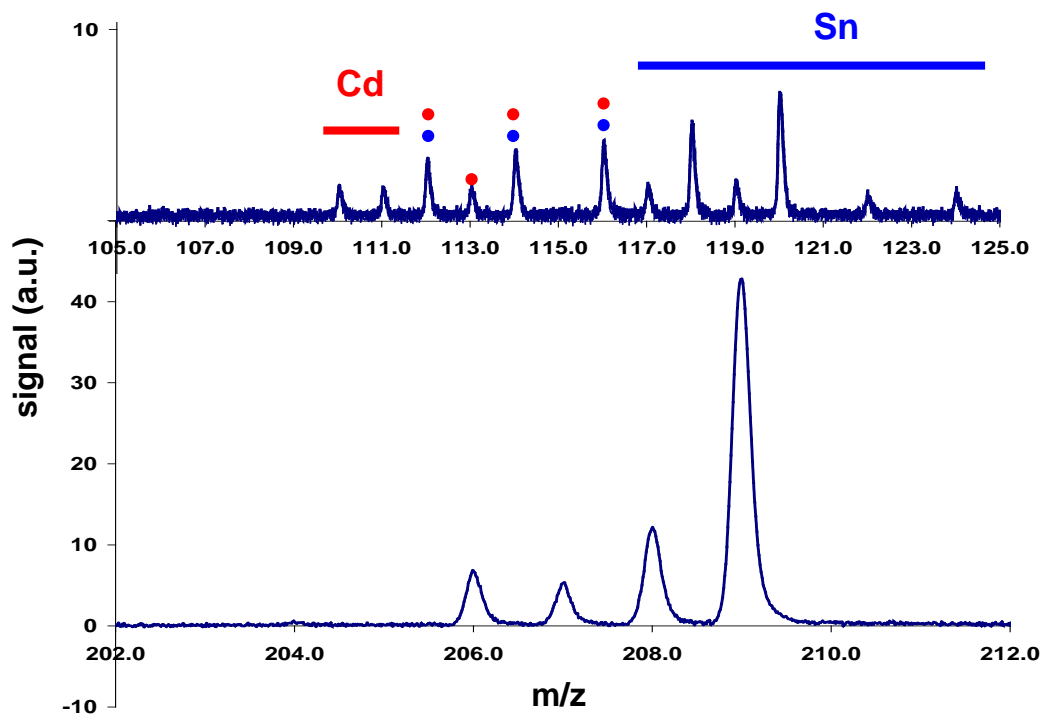


Figure 5-13. Mass spectrum from laser ablation of a bismuth alloy sample.

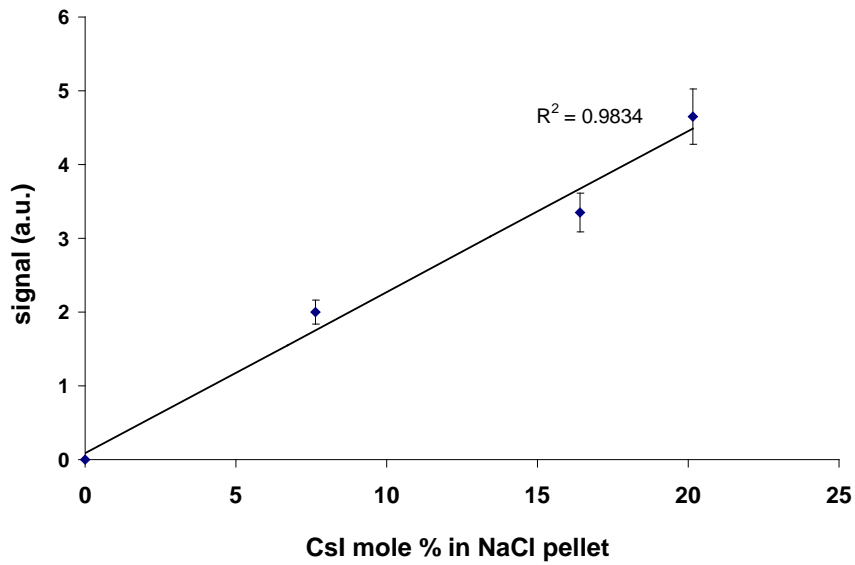


Figure 5-14. Cesium signal vs. mole % of cesium at different salt pellets.

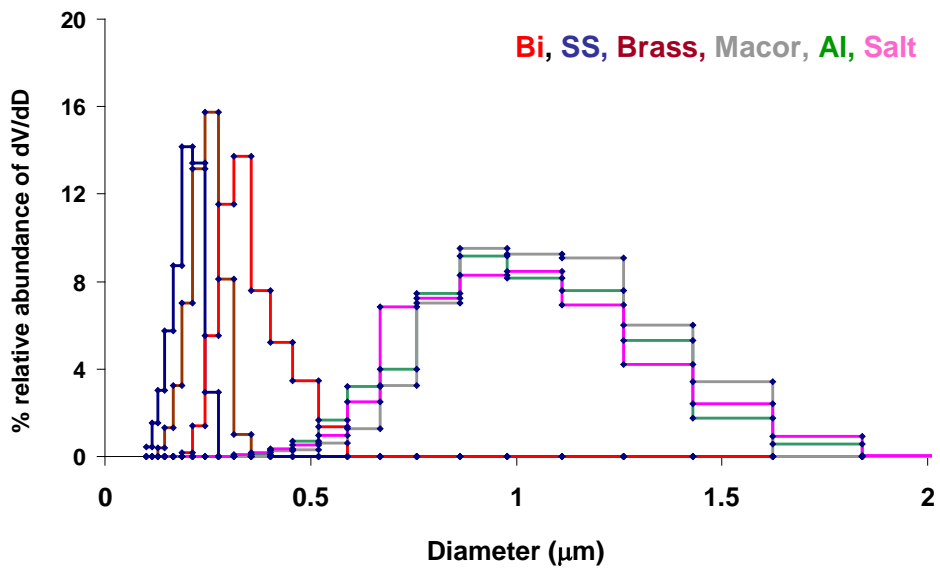


Figure 5-15. Particle size distributions for aerosols generated from different samples.

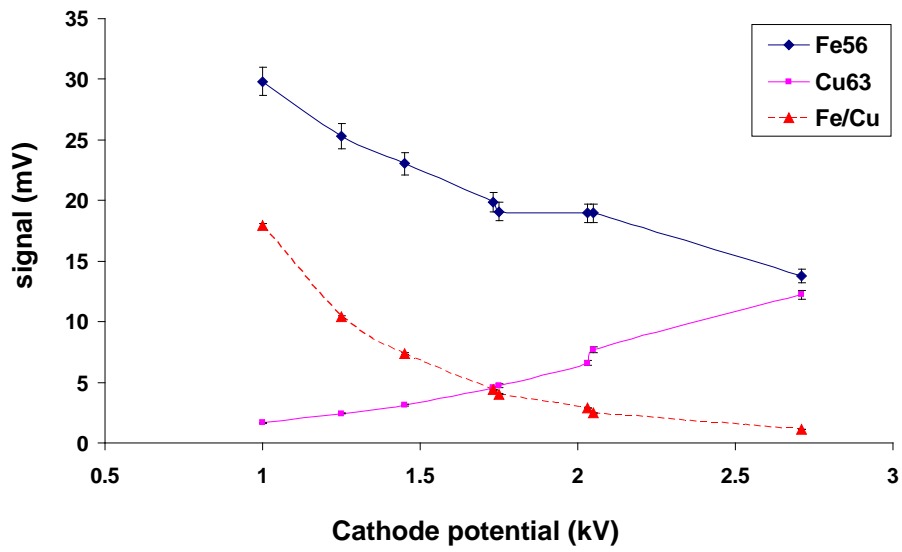


Figure 5-16. The effect of cathode potential on ionization of stainless steel particles (^{56}Fe signal) is compared with its effect on cathodic sputtering of brass (^{63}Cu signal).

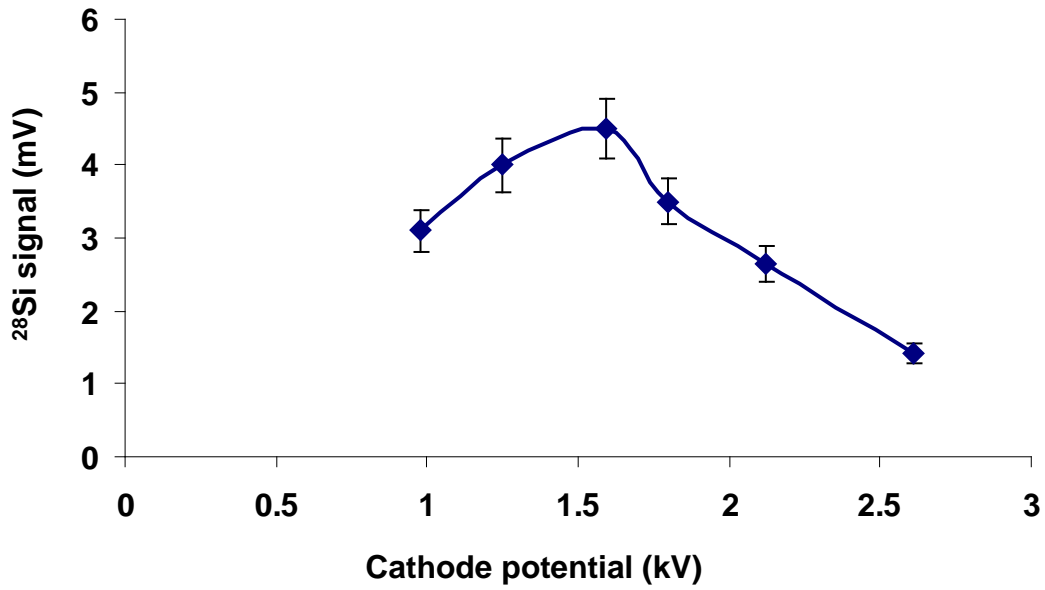


Figure 5-17. The effect of cathode potential on ionization of Macor particles.

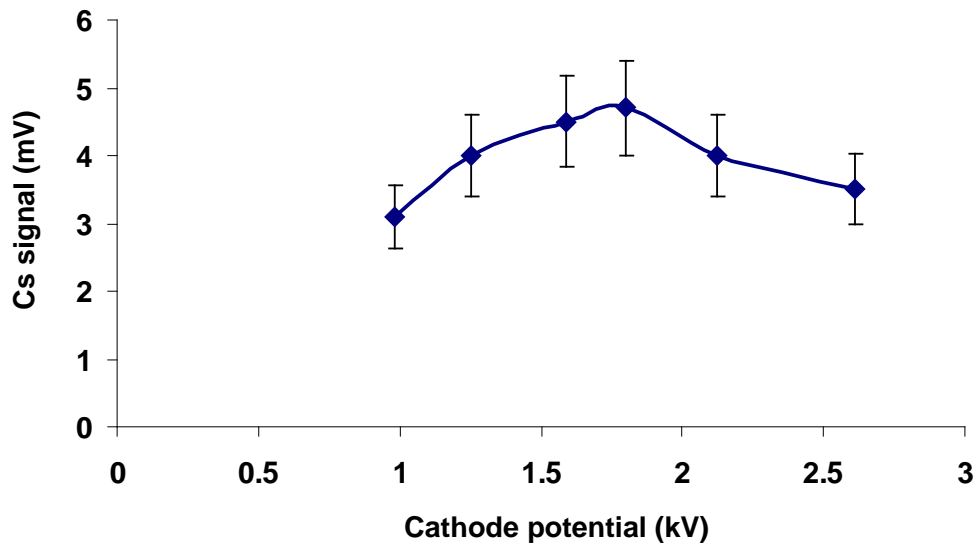


Figure 5-18. The effect of cathode potential on ionization of salt particles.

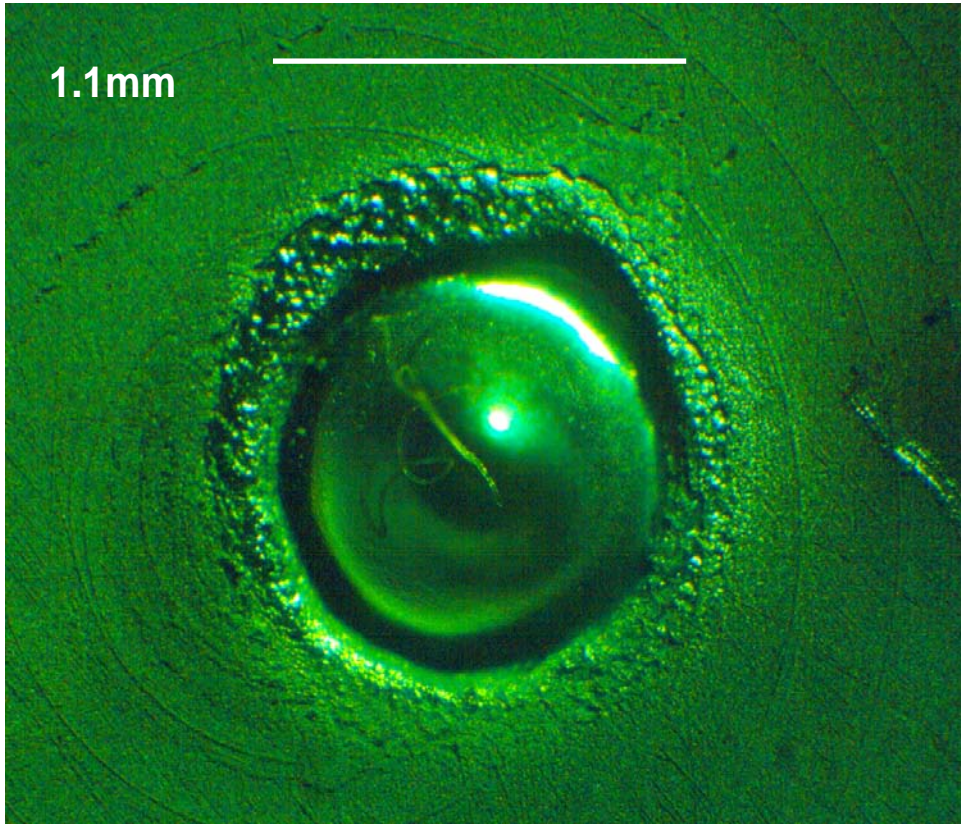


Figure 5-19. Crater image of bismuth sample after ablation by 219 laser shots at 10 Hz and maximum energy. Crater diameter = 1.1 mm.

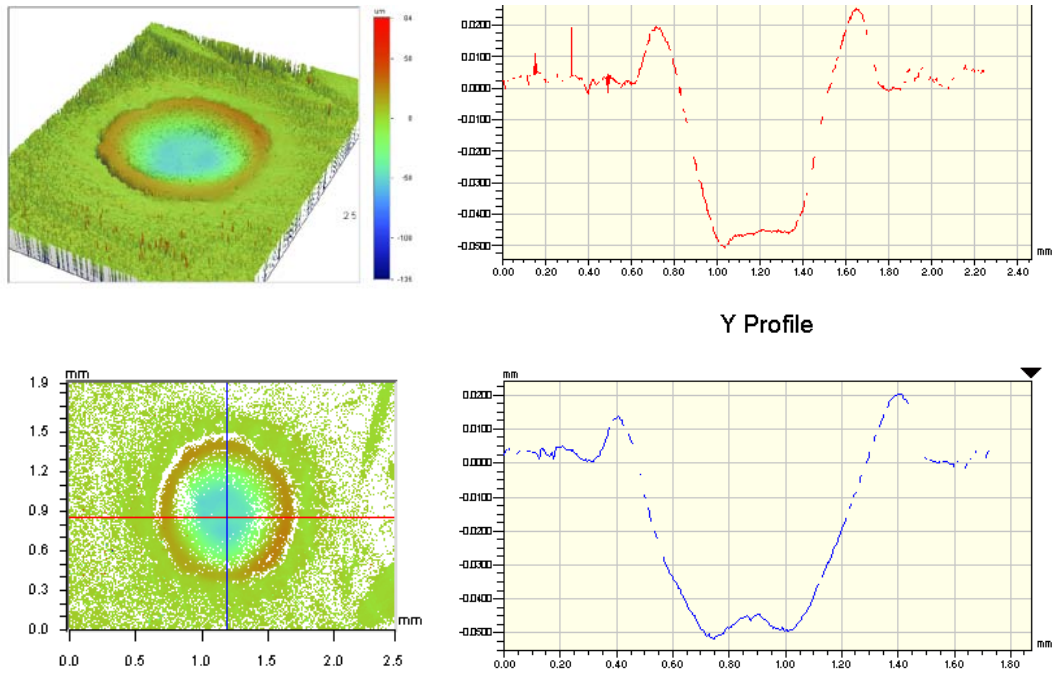


Figure 5-20. The crater profile shape and dimension measured by an optical profilometer. After ablation by 219 laser shots at 10 Hz and maximum laser energy.

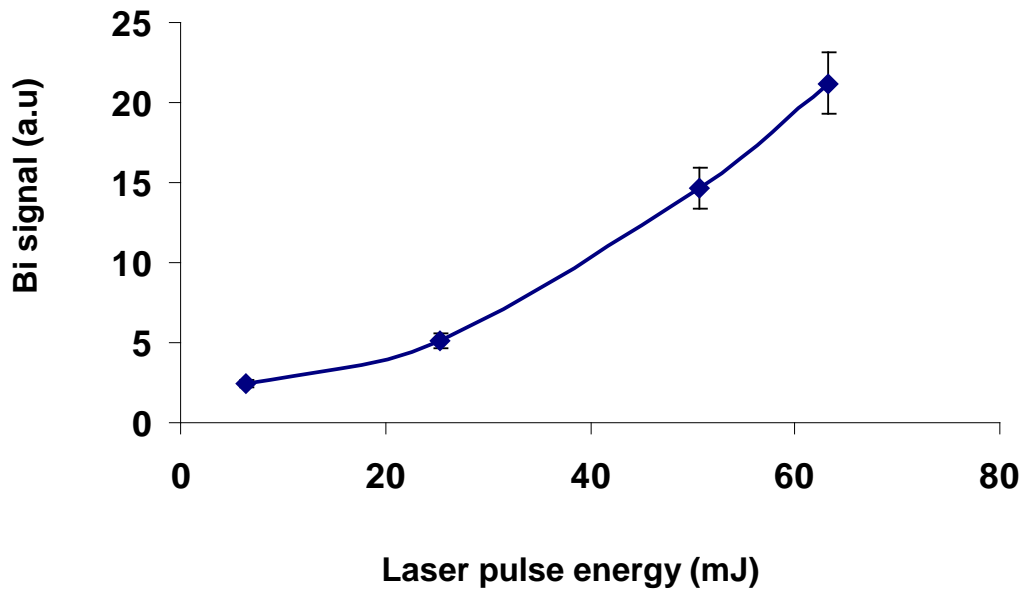


Figure 5-21. The effect of laser pulse energy on LA-GD-MS Bi ion signal of bismuth alloy particles.

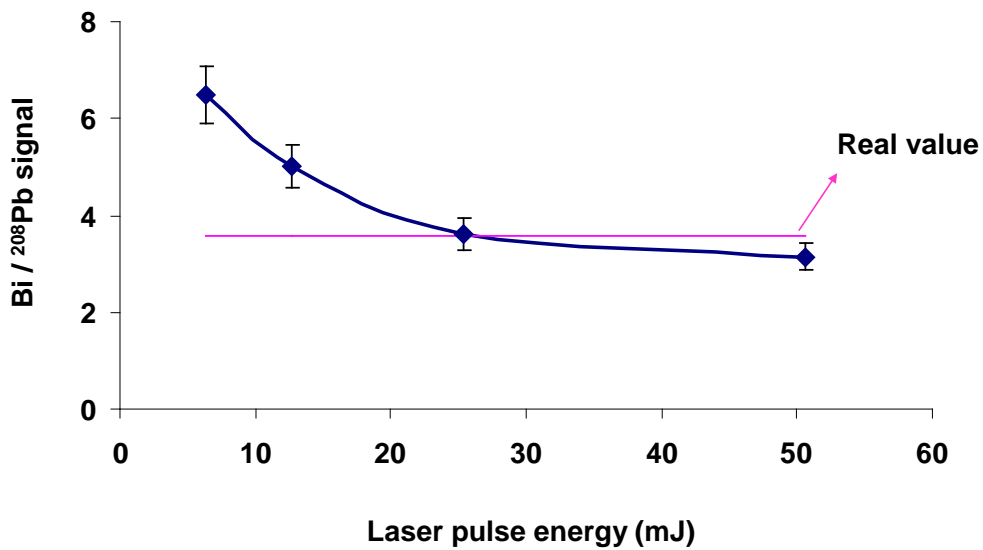


Figure 5-22. The effect of laser pulse energy on ²⁰⁹Bi to ²⁰⁸Pb signal ratio.

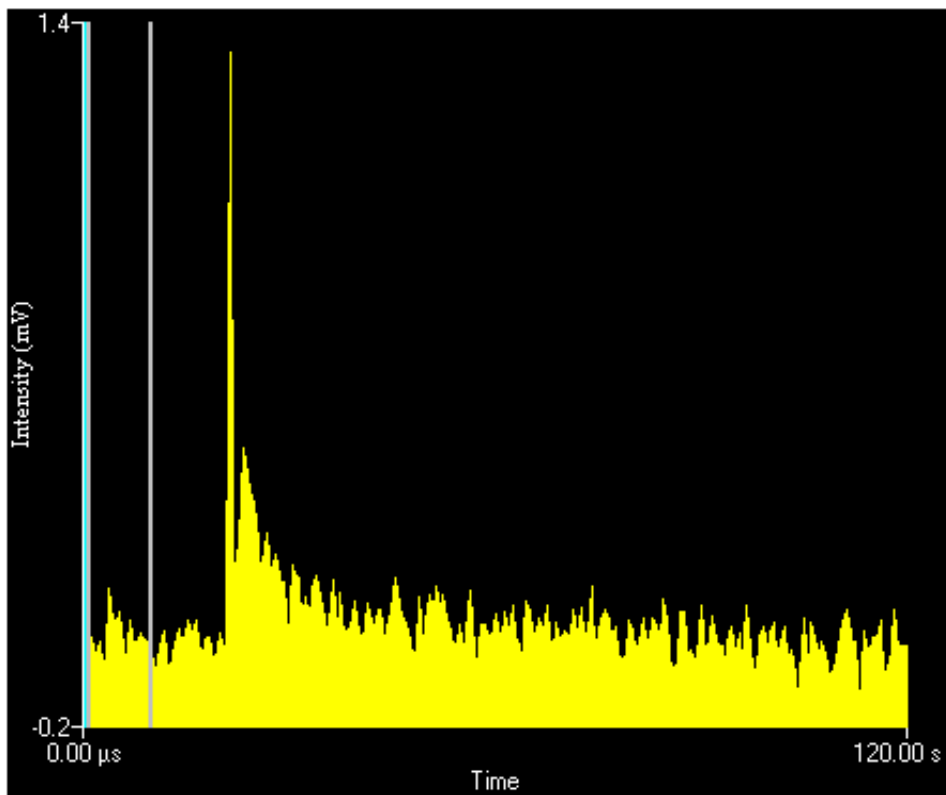


Figure 5-23. Memory effect investigation: The initiation of glow discharge after ablation of bismuth sample (305 shots) ended resulted in a spike in Bi signal.

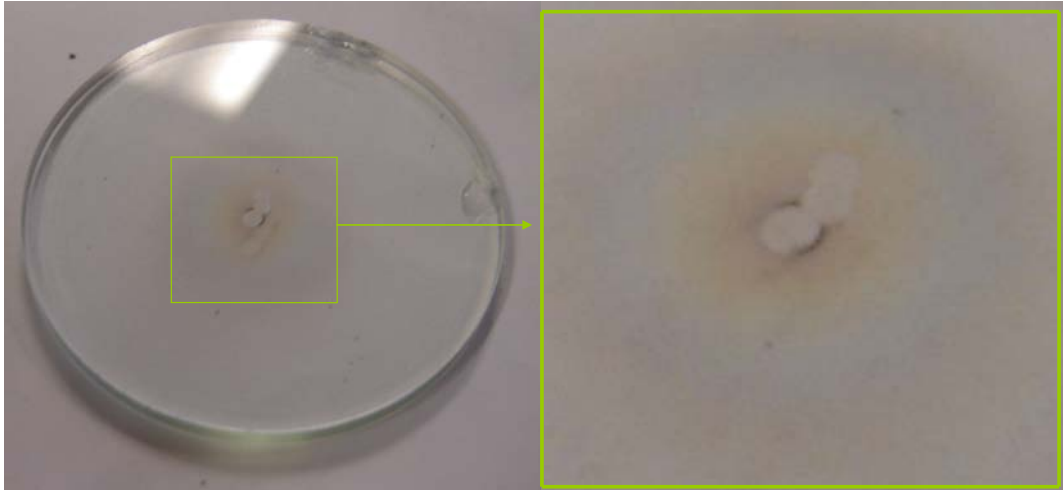


Figure 5-24. Particle deposition and laser back ablation of bismuth alloy on quartz window.

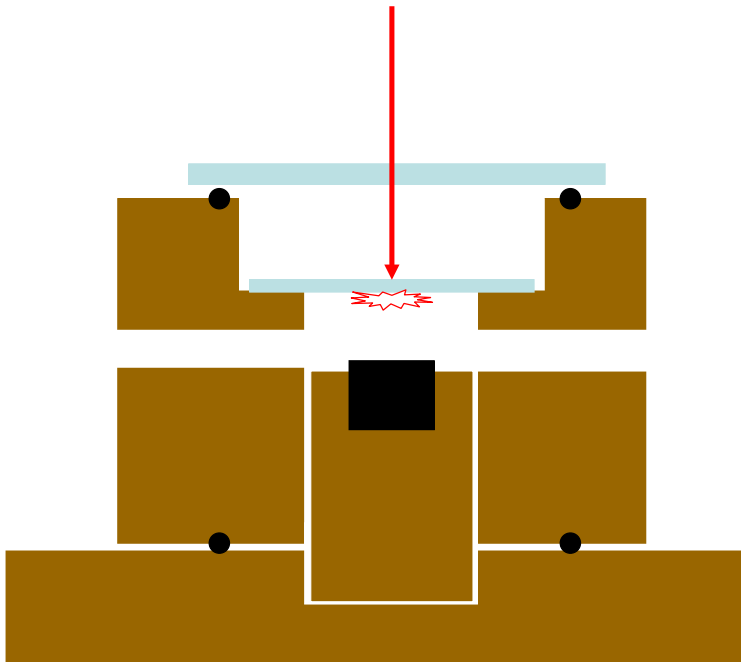


Figure 5-25. Ablation cell set up for laser back ablation of sample from the surface of the quartz window.

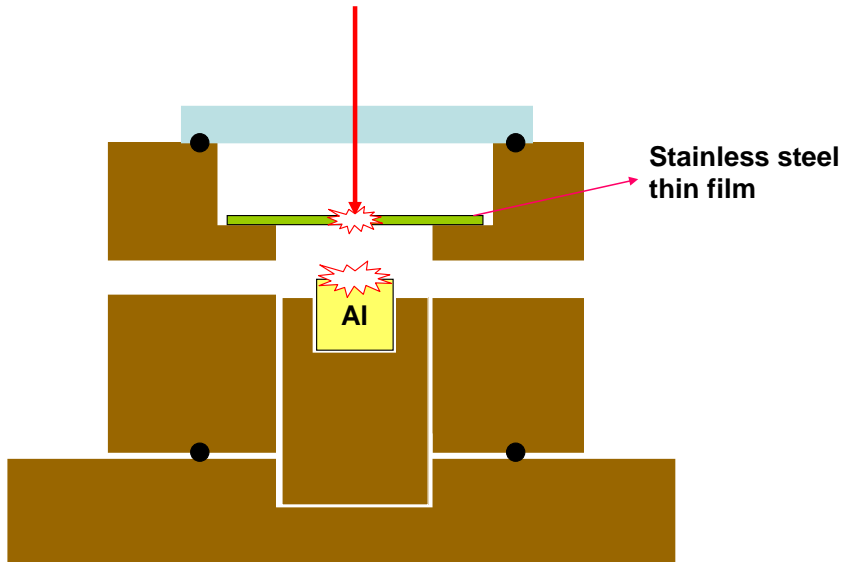


Figure 5-26. Ablation cell set up for laser back ablation of a thin stainless steel film located above a sample of aluminum.

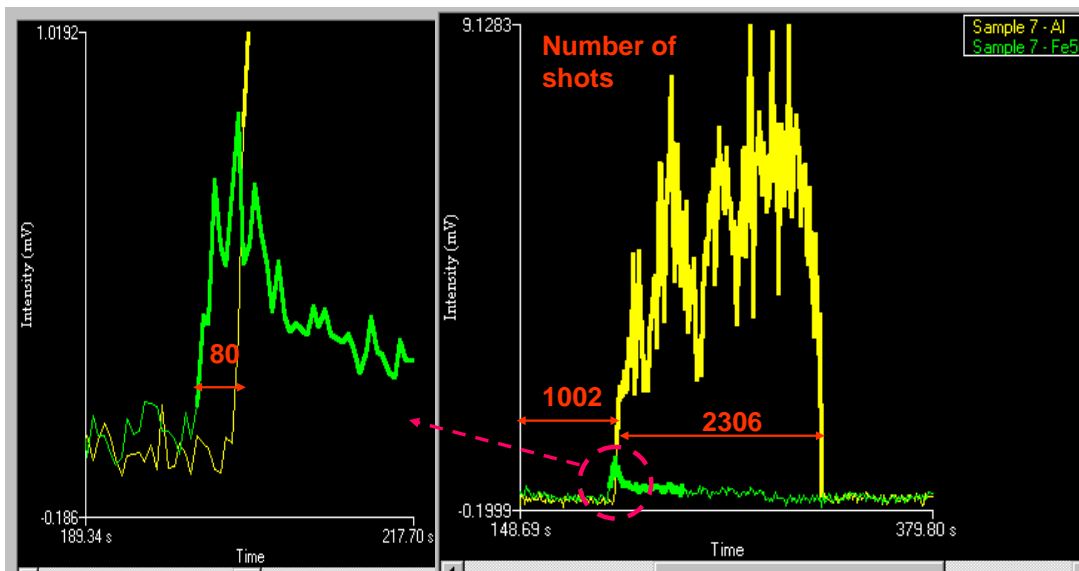


Figure 5-27. Signal vs. time for back ablation of stainless steel followed by regular ablation of aluminum sample. After about 1000 shots the stainless steel sample is completely etched and ablation of aluminum starts.

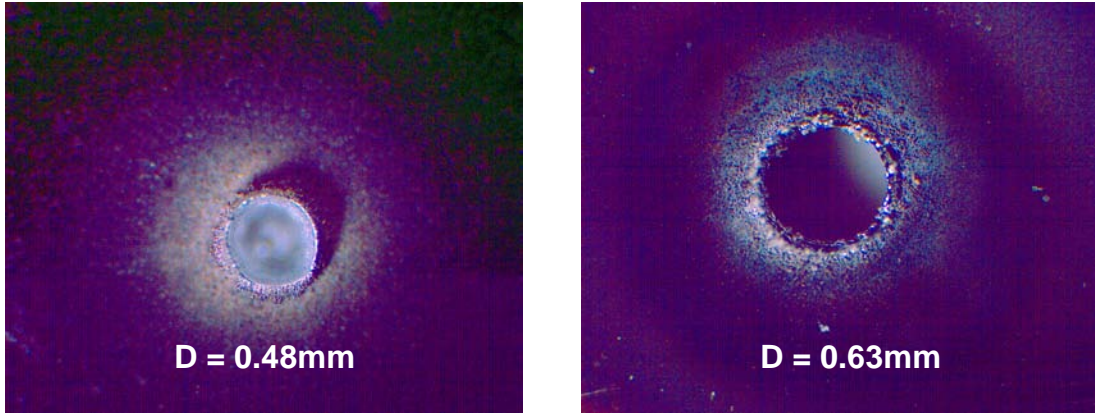


Figure 5-28. Crater diameters for stainless steel and aluminum.

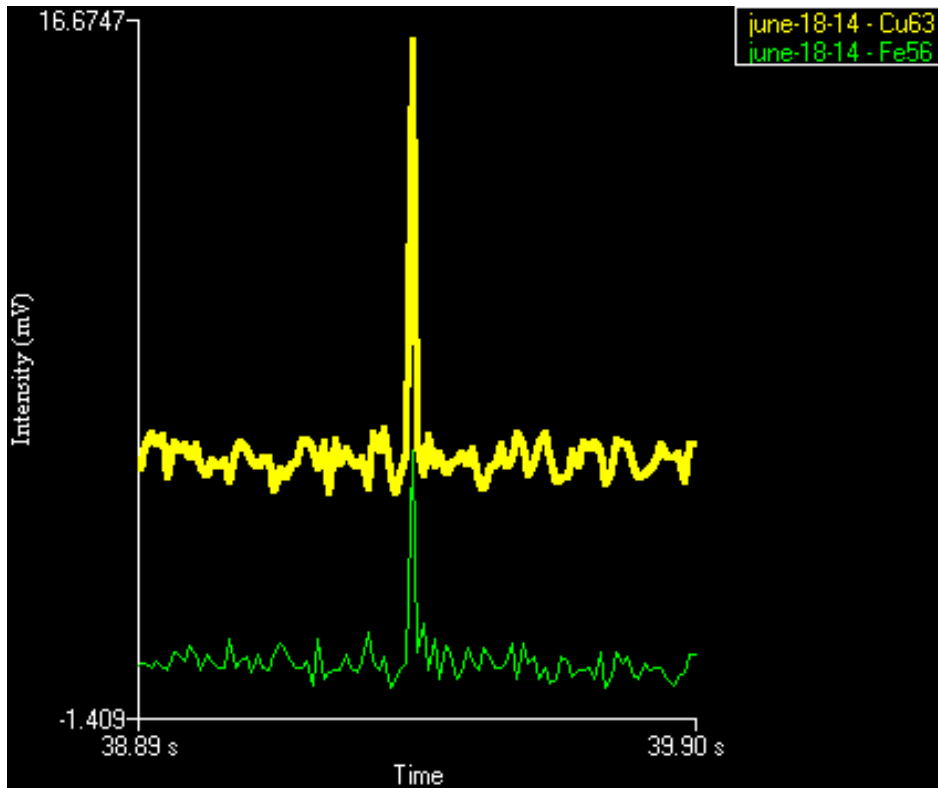


Figure 5-29. Spike in copper signal due to entrance of stainless steel particles into the discharge, by a single laser shot.

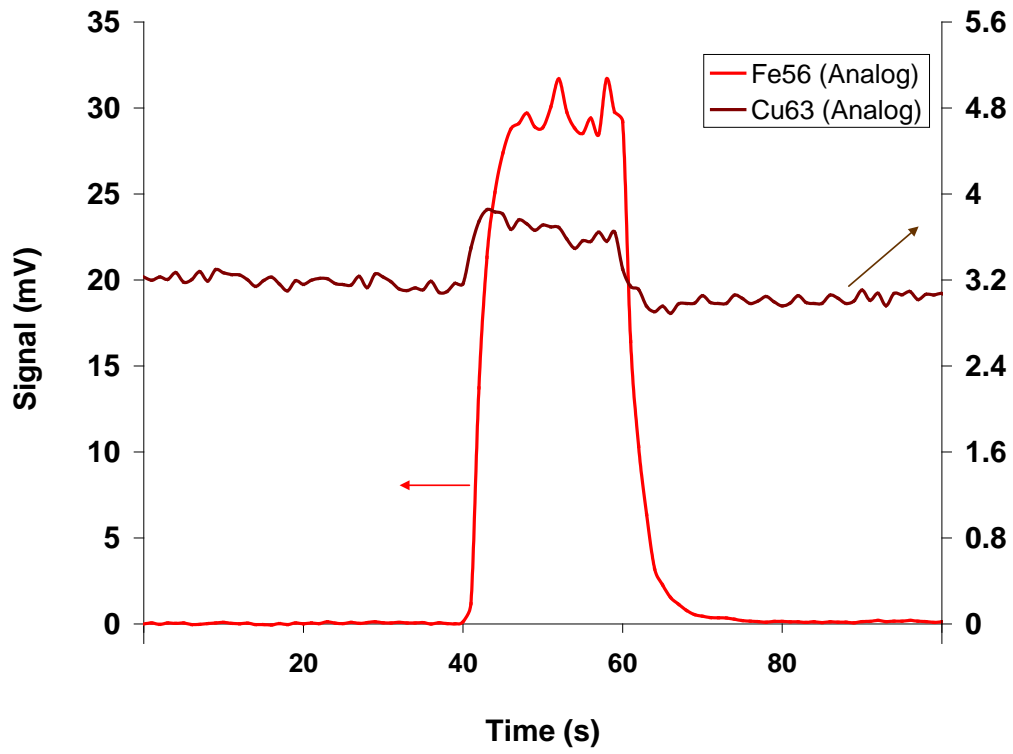


Figure 5-30. Increase in copper signal due to entrance of a 20 second ablated package of stainless steel particles into the discharge.

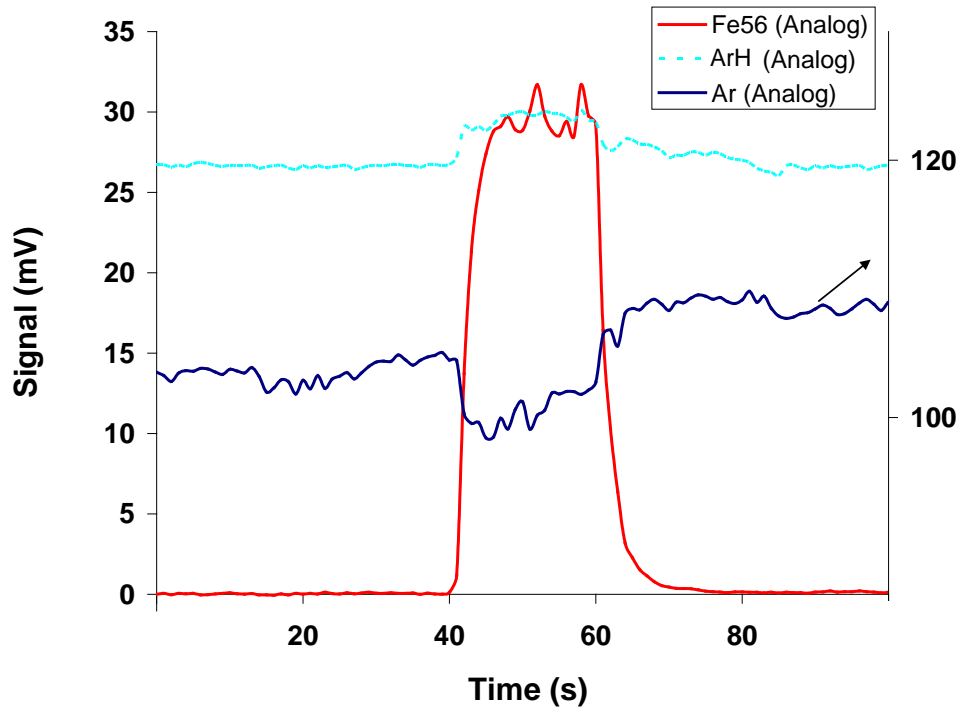


Figure 5-31. The effect of ablation of stainless steel on Ar^+ and ArH^+ ion signals. The right hand Y-axis is for the argon ion only.

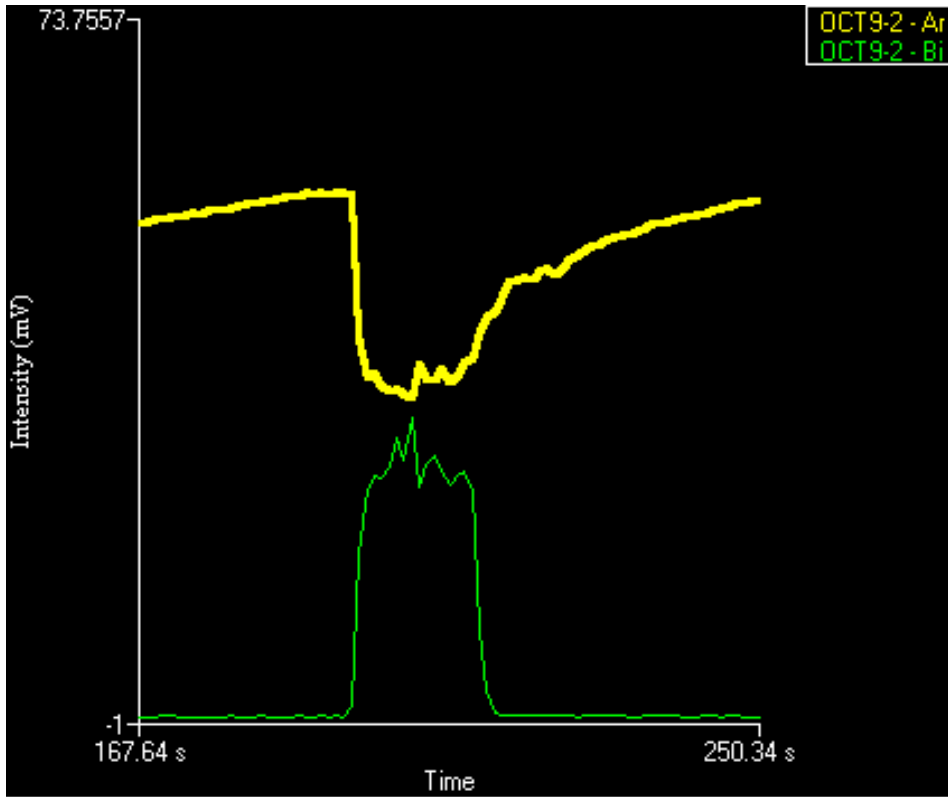


Figure 5-32. The effect of bismuth alloy ablation on Ar^+ ion signal.

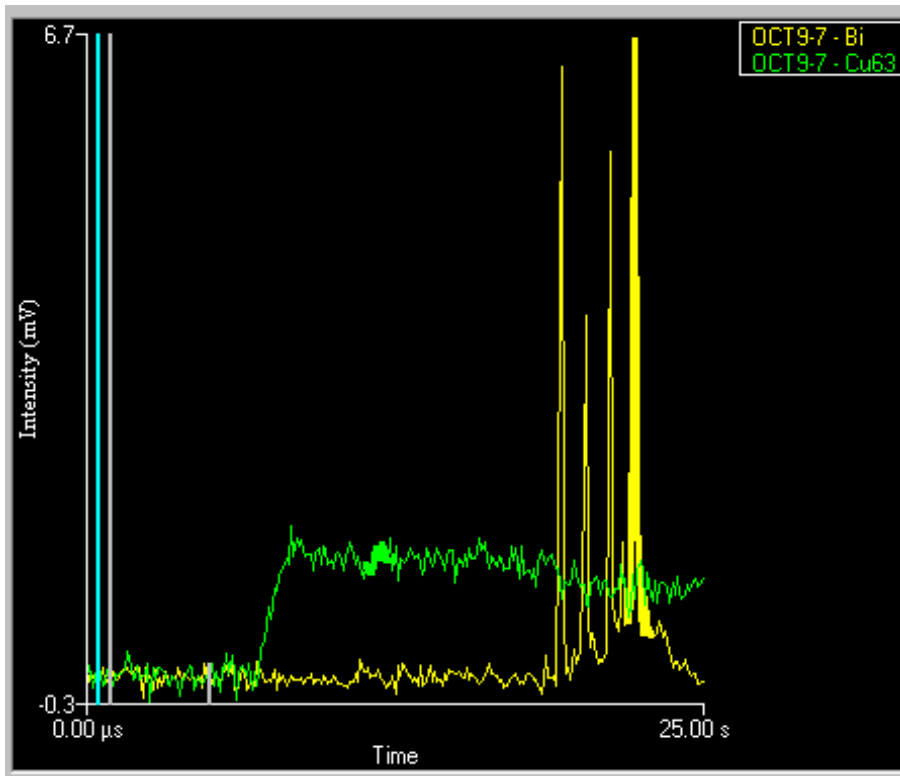


Figure 5-33. The effect of 4 single shots of laser ablation of bismuth alloy on $^{63}\text{Cu}^+$ ion signal. No significant change in copper ion signal is observed.

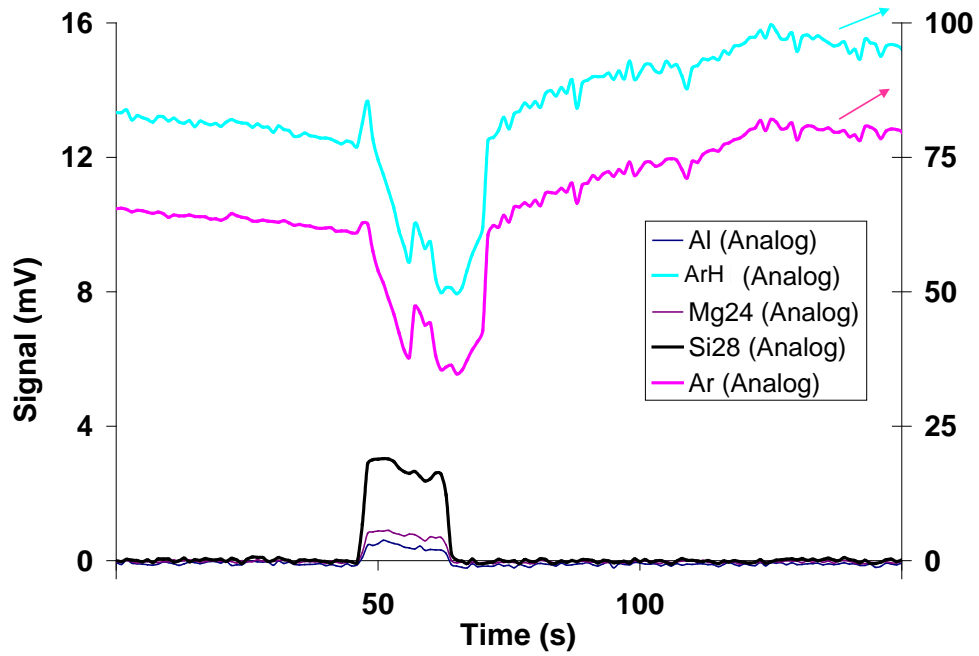


Figure 5-34. The effect of ablation of Macor on $^{40}\text{Ar}^+$ and ArH^+ ion signals.

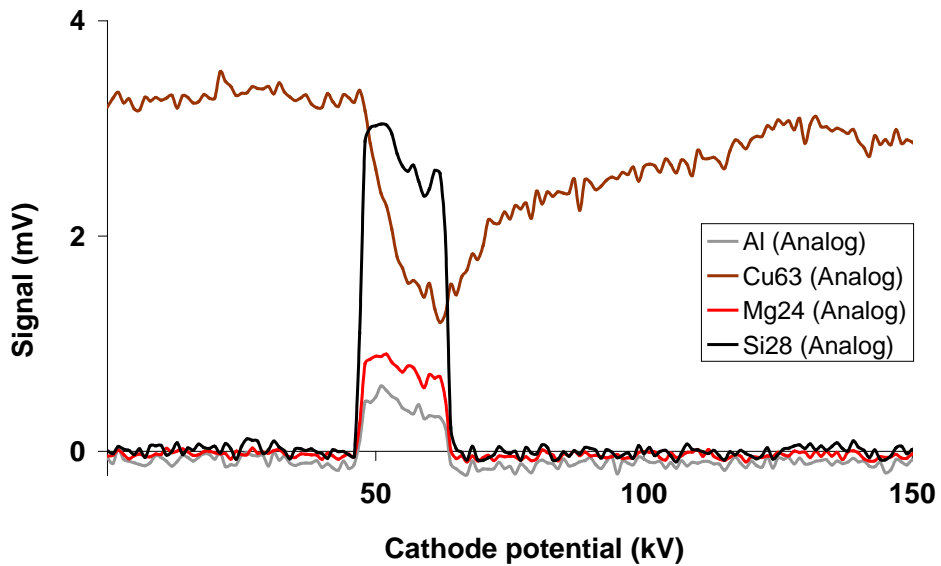


Figure 5-35. The effect of ablation of Macor on $^{63}\text{Cu}^+$ signal.

CHAPTER 6 CONCLUSION AND FUTURE WORK

This work showed that the low pressure ionization source of a pulsed glow discharge plasma can provide enough energy for production of ions from particles. In other words, the Grimm source is capable of vaporization-atomization and ionization of aerosols with volume mean diameters ranging from 100 nm up to 900 nm. It is believed that only the cathode dark space (CDS) of our glow discharge is capable of providing enough energy for this process. High energy species such as fast argon ions (population of about 4×10^{13}),¹⁰¹ fast argon atoms and fast electrons in this region⁷ will sputter the particle while it passes through this region. The linearity of signal vs. concentration of salt even in the presence of a buffer background salt provides evidence for complete particle vaporization in the CDS. The fact that the signal vs. cathode potential reaches a plateau also proves this hypothesis as the particles are completely vaporized.

The problem of sending a nebulized aerosol into the glow discharge is mostly due to the interface between the atmospheric pressure sample and a low pressure source (Chapters 3 and 4). The laser ablation generation of aerosols allowed for producing the particles at a low pressure similar to that of the discharge source (Chapter 5). Therefore, no restriction between the aerosol source and plasma was required. The LA-GD-MS resulted in higher intensities compared to that of solution nebulization GD-MS.

The introduction of particles into the discharge resulted in the change in plasma conditions. The plasma cooling always caused a decrease in $^{40}\text{Ar}^+$ signal. Most particles boosted the $^{63}\text{Cu}^+$ as the ions from the particles enhanced cathode sputtering. The cathode becomes contaminated if a large amount of aerosol is introduced and requires cleaning. Usually metal samples are less problematic in comparison with non-conductive samples such as Macor and salt particles. However, if aerosols are introduced in short packages in terms of time, (1-20 seconds) the

discharge will return to its original condition shortly after the particle introduction is halted. The argon signal will rise up to its previous intensity and the cathode will be cleaned by cathodic sputtering.

It is important to note that our aim was the characterization of particle- glow discharge interactions, and therefore not strictly analytical. For analytical purposes, the low pressure plasma of glow discharge is no match for a powerful technique such as ICP-MS. The gas kinetic temperature of a pulsed glow discharge is about 800 K^{102, 103} and might reach as high as 1000 K.¹⁰¹ On the other hand, gas kinetic temperatures as high as 5700 K for argon ICP plasma has been reported. The limits of detection in aqueous solution were 13 ppm, 14 ppm and 5 ppm for cesium, iodine and sodium, respectively. Using the same TOF mass spectrometer, detection limit of 0.1 ppm for lead in a wine sample was reported when ICP was the source of ionization.¹⁰⁴ For analysis of solid samples by LA-GD-MS, the detection limit was 1% for lead in the bismuth alloy. Detection limits of 0.1-1 ppb for LA-ICP-MS has been reported.⁸⁴

One of the main reasons for such high limits of detection in our set up is the poor ion transfer and extraction. The majority of positive ions formed in the CDS will return to the cathode due to the high electric field in this region. Reversing the cathode-anode polarity might offer a solution to this problem. Another reason for low ion signal is the poor extraction efficiency at the skimmer. The skimmer of the instrument is grounded and practically there is no sampler aperture. The only force to extract the ions from the first stage into the second stage is the pressure difference between the two stages. As a result, the majority of the ions are just pumped out with the flow of argon. The use of ion funnels to transfer more ions into the second stage and geometrical modifications of the source could alleviate this problem and increase the ion transfer efficiency.

Future work should continue in the following three areas. First, the geometry of the glow discharge should be modified to allow an easier access to the laser beam (in the case of laser ablation studies) and a better sampling efficiency of the ions produced. Second, the study should be extended to other elements and other type of aerosols (for example, biological aerosols). Third, the electrical operating characteristics of the source should be modified, in order to allow the use of much longer voltage pulses (of the order of milliseconds) and therefore attempt a more complete characterization of the particle composition (elemental as well as molecular).

As this work showed, the geometry of the glow discharge ionization source can play an important role in particle ionization efficiency. For example, in a preliminary experiment in which the cathode surface was made smaller, the signal intensity increased by a factor of ~4. As Figure A-12 in Appendix A shows, in this configuration, the smaller cathode surface will intensify the ion and electron current per unit area of the cathode. Another future work consideration for modification of GD geometry would be to design a discharge configuration in which the laser beam can ablate the sample immediately next to the discharge plasma. This will increase the aerosol transfer efficiency into the plasma. However, a shorter transfer pathway of aerosol might result in smaller packages of particles, which might require synchronization between laser and glow discharge pulses to observe particle-plasma interaction.

Although our present LA-GD-MS set-up does not provide analysis of elements with sub-percentage composition, it can still be used for sample identification. For example, some geological samples can be distinguished from each other by analysis of major elements, usually present at percentage levels in the sample. Moreover, the lower cost of a GD source is an advantage over ICP.

Elemental analysis, even at limits of detection as high as 1%, can provide meaningful information in some biological applications. For instance, elemental analysis of fish scales¹⁰⁵ for the purpose of water pollution studies and mapping of bio-mineral structures such as uroliths¹⁰⁶ can be done by LA-GD-MS. Another interesting application for LA-GD-MS would be in cases where sample ablation occurs at low pressures, while ICP is limited to atmospheric pressure. For example, LIBS analysis of hematite under a Mars-like atmosphere has been investigated.¹⁰⁷ In order to investigate the same system by mass spectrometry one can use the low pressure (~10-20 torr) ablation cell along with the pulsed GD source.

One of the objectives in this research was to obtain molecular information as well as elemental analysis. However, the results of particle ionization did not show any evidence toward the existence of molecular ions, which could be due to the short duration of the ionization pulse. Using a millisecond ionization pulse (instead of microsecond) could increase the possibility for observation of molecular ions at the after pulse. It would be interesting to study biological and organic aerosols, because they are easier to vaporize and the possibility of observing molecular ions increases.

APPENDIX
COMPLEMENTARY FIGURES

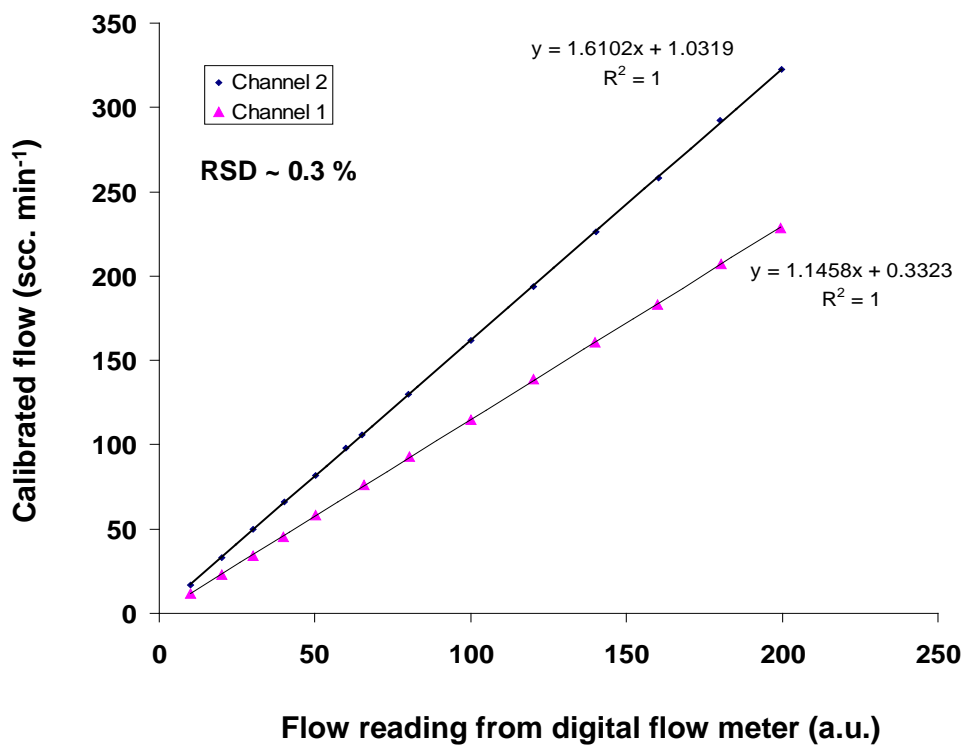


Figure A-1. Calibration of the digital flow meter by the soap bulb method. The real value of flow in standard cubic centimeter per min is shown.

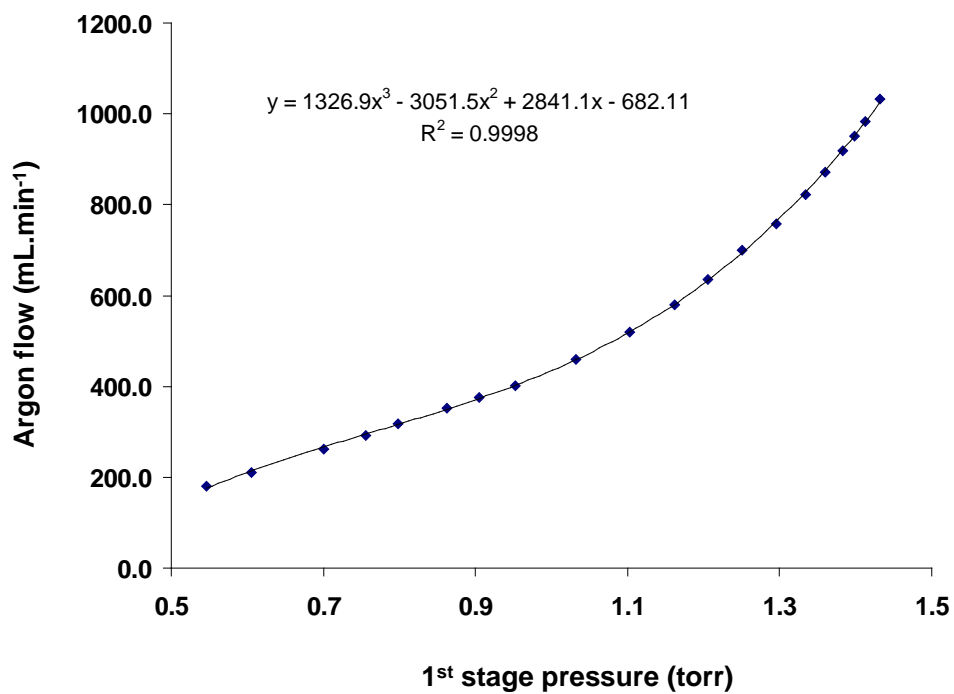


Figure A-2. Calibration of the argon flow into the glow discharge with respect to the first stage pressure. The position of vacuum valve must remain constant (all open) for this calibration graph to be valid.

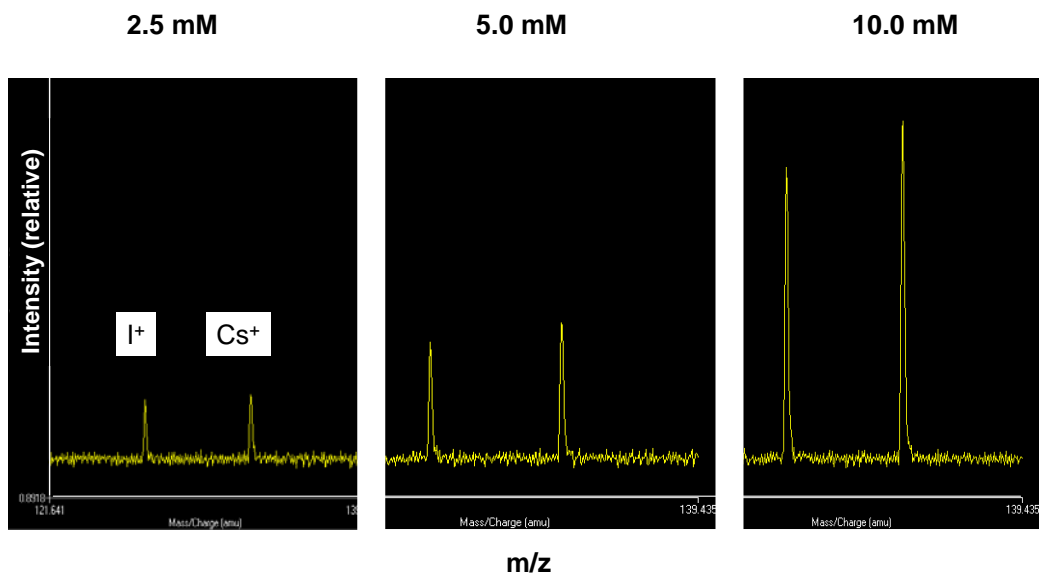


Figure A-3. Signal intensities for Cs and I at three different concentrations of CsI solution are shown.

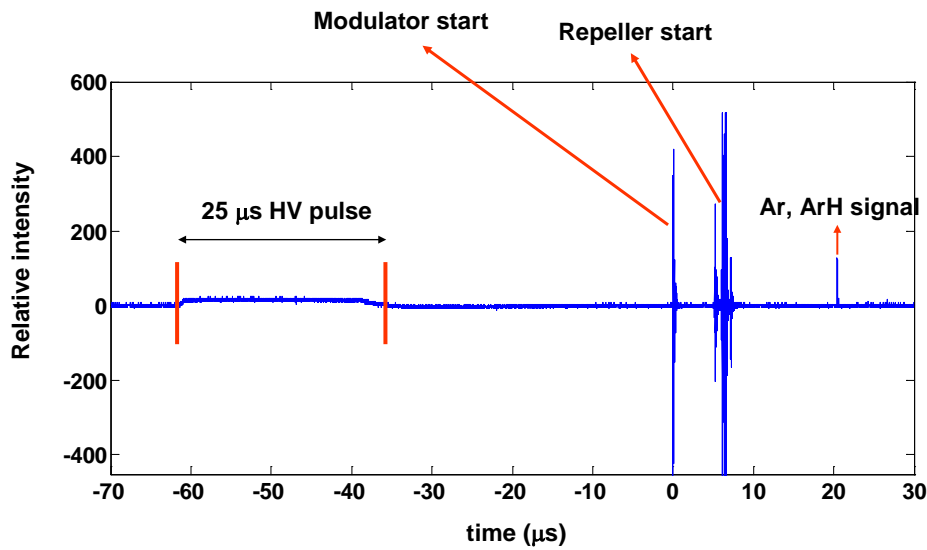
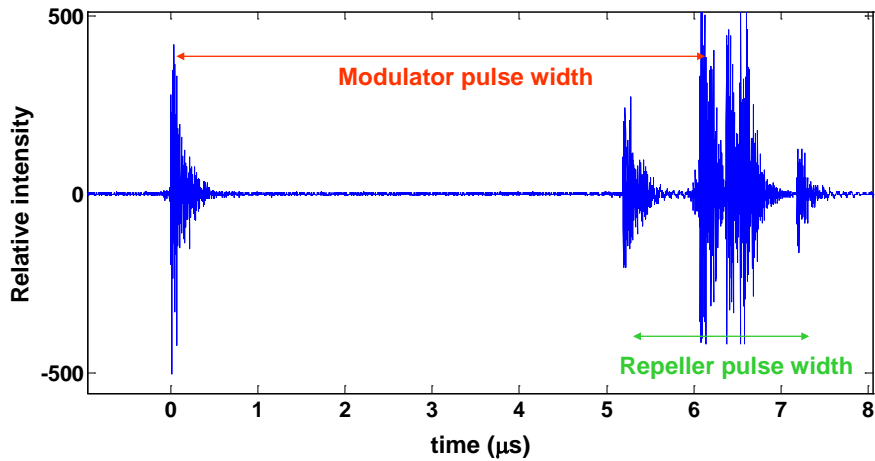


Figure A-4. Repeller and modulator ringing from the oscilloscope is shown. The HV pulse is also detected at a delay time of $\sim 65 \mu\text{s}$ before the repeller pulse (bottom). The repeller and modulator pulses are shown with higher magnification as well (top).

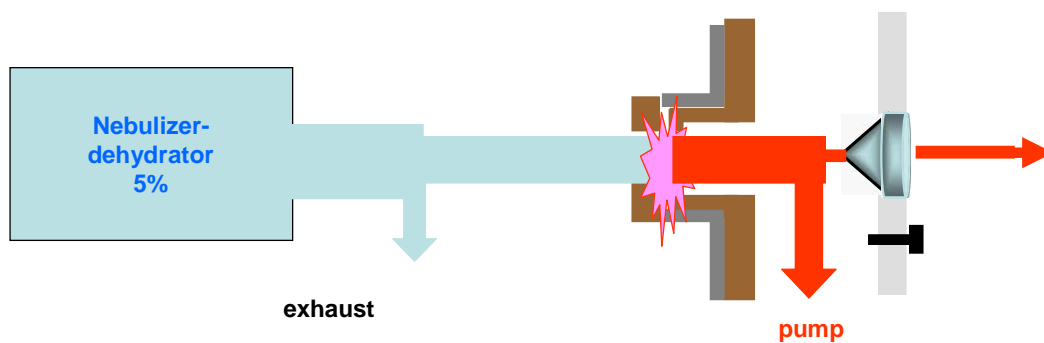


Figure A-5. The sources of particle and ion loss before the skimmer of time-of-flight are shown.

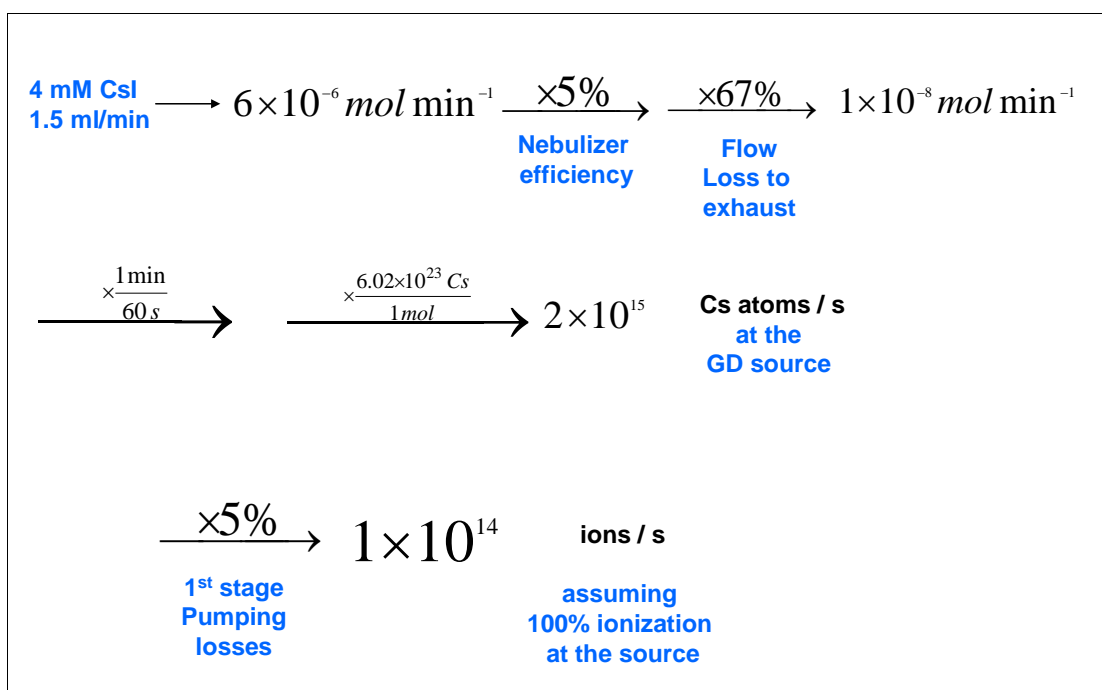


Figure A-6. Calculation of the number of ions expected to arrive at the detector assuming 100% ionization and ion transfer efficiency.

$$\begin{array}{l}
 \text{20 mV signal} \xrightarrow[\text{R=5K}\Omega]{V=RI} 4 \times 10^{-6} \text{ C/s} \xrightarrow[\text{Electron charge}]{\frac{1e}{1.6 \times 10^{-19} \text{ C}} \times \frac{1ion}{10^6 e}} \text{Detector gain} \\
 \\
 2.5 \times 10^7 \text{ ions/s} \\
 \\
 \text{Ionization efficiency} = \frac{2.5 \times 10^7}{1 \times 10^{14}} \times 100 = 2.5 \times 10^{-5} \%
 \end{array}$$

Figure A-7. The overall efficiency of the particle vaporization-atomization-ionization and ion transfer to detector is calculated.

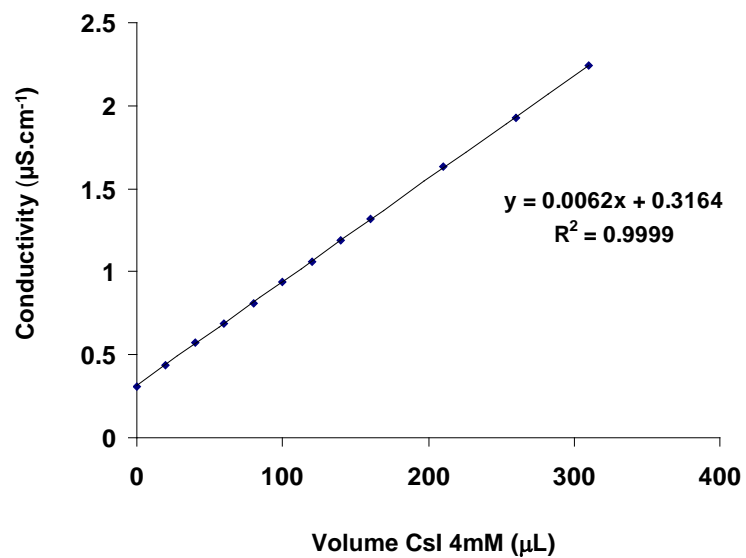


Figure A-8. Calibration graph for conductivity vs. concentration of CsI. The volume of the 4 mM CsI solution added to a 100 ml solution is directly proportional to conductivity of the final solution.

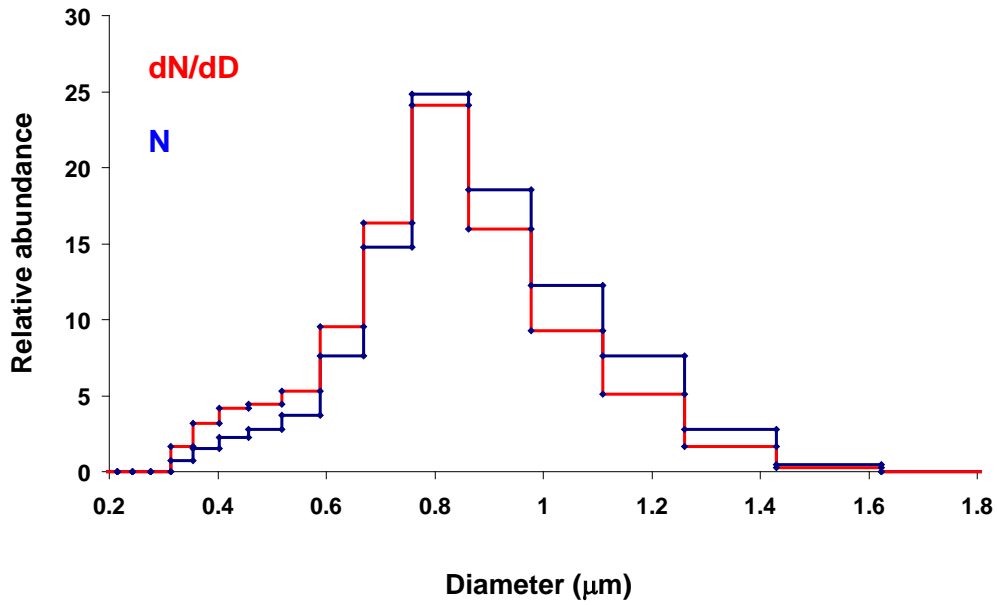


Figure A-9. Result of the particle size distribution measurement for ablation of Macor. Relative abundances of dN/dD is compared to N . At larger bin sizes the dN/dD is smaller than N and vice versa.

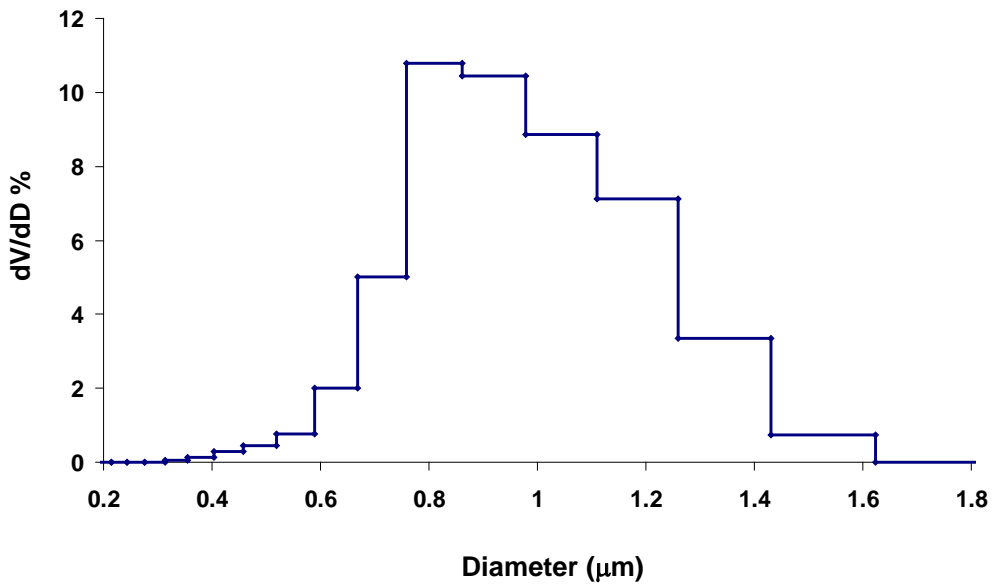


Figure A-10. The particle size distribution for Macor aerosol is shown as dV/dD . The relative intensity at larger particle diameters increases.

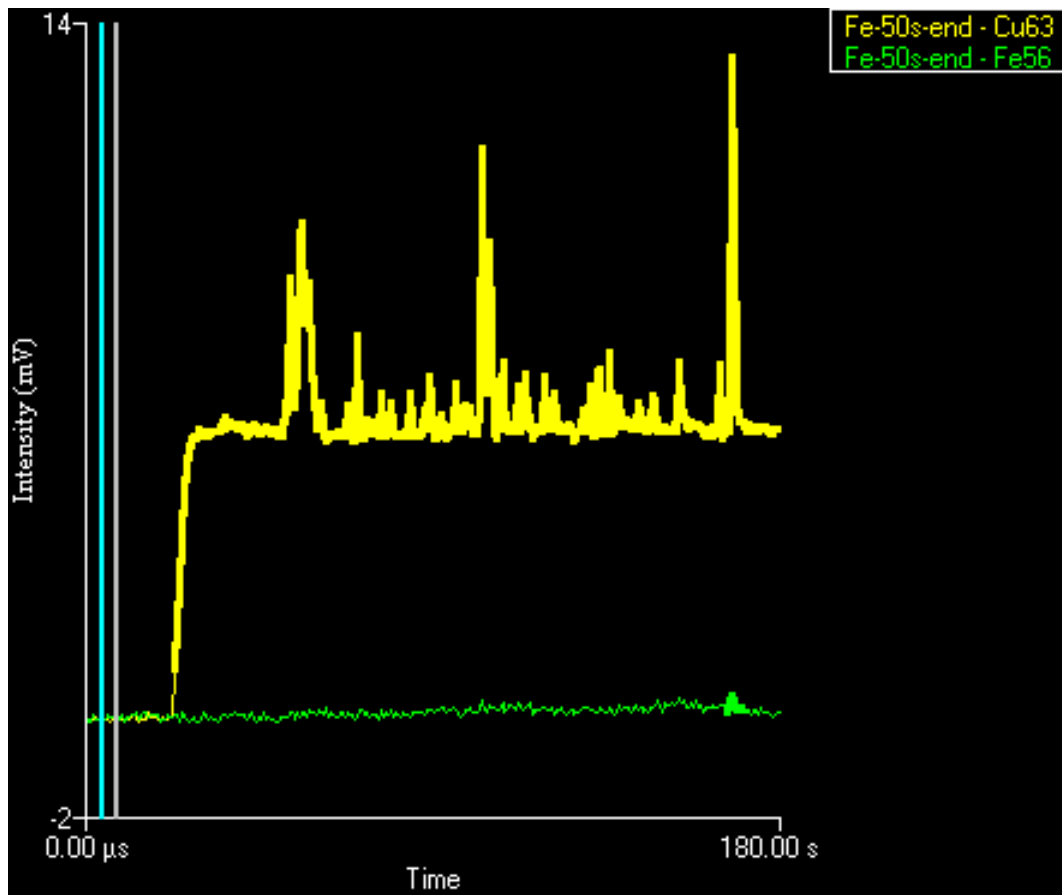


Figure A-11. The effect of ablating stainless steel by the power-chip Nd: YAG laser on copper signal. Although, no iron signal is detected, the copper signal is influenced by laser ablation of the stainless steel sample.

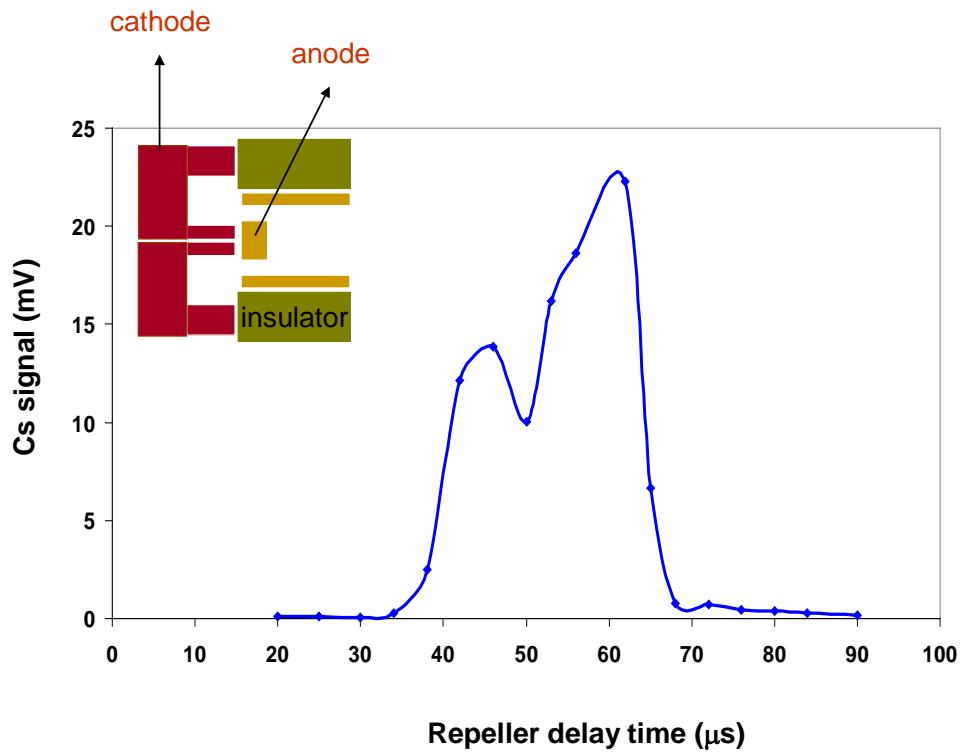


Figure A-12. Geometrical modification of cathode resulted in ion signal as high as 22 mV for Cs^+ upon nebulization of a 4 mM CsI solution.

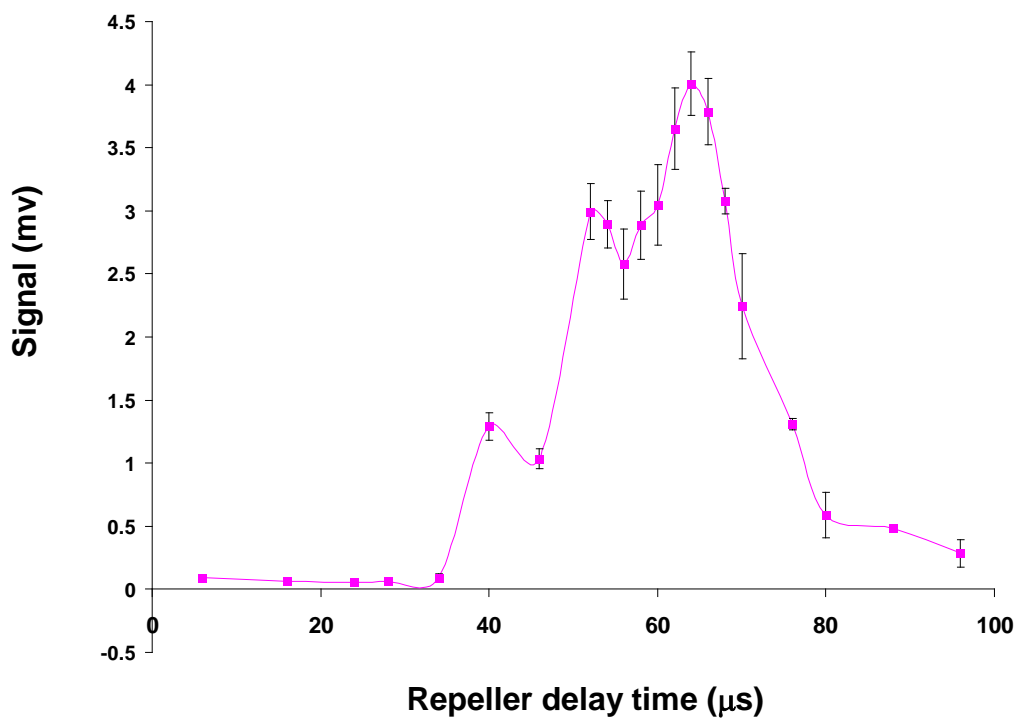


Figure A-13. The Cs⁺ signal vs. delay time is shown as well as the error bars. The error bars represent the standard deviation of the mean for 5 series of collection. The pressure of the first stage is 1.45 torr. Refer to figure 3-9 for data related to other pressures.

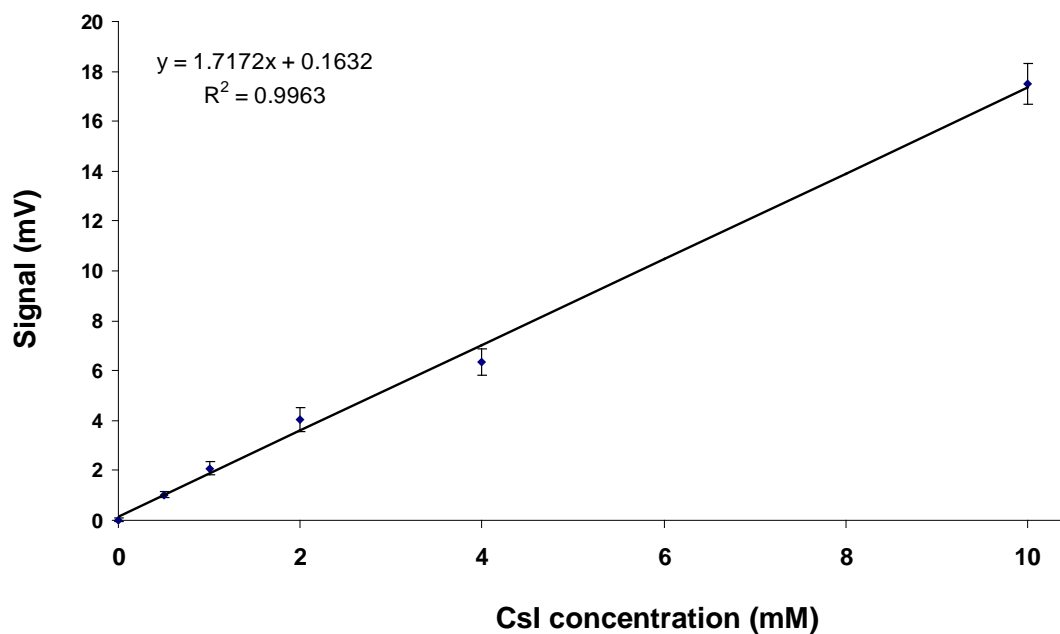


Figure A-14. The signal for Cs^+ ion vs. CsI concentration show a linear dynamic range from 0.50 mM to at least 10.0 mM. The concentrations higher than 10.0 mM were not used to avoid sending an excess amount of salt into the system. Limit of detection of 0.1 mM was calculated based on standard deviation of background = 0.05 mV. Cathode was heated to 75°C and cathode potential = 1.80 kV.

LIST OF REFERENCES

1. J. D. Cobine, *Gaseous Conductors: Theory and Engineering Applications*, Dover Publications, Inc. 1958.
2. A. M. Howatson, *An Introduction to Gas Discharges. 2nd Ed.*, Pergamon Press Ltd. 1976.
3. R. K. Marcus and J. A. C. Broekaert, *Glow Discharge Plasmas in Analytical Spectroscopy*, John Wiley & Sons, Inc. 2003.
4. D. Fang and R. K. Marcus, *Glow Discharge Spectrosc.*, 1993, 17-66.
5. H. A. Hyman, *Physical Review A: Atomic, Molecular, and Optical Physics*, 1979, **20**, 855-859.
6. R. J. Carman, *Journal of Physics D: Applied Physics*, 1989, **22**, 55-66.
7. A. Bogaerts, Mathematical modeling of a direct current glow discharge in argon. Ph.D. dissertation, Universiteit Antwerpen, Antwerpen, Belgium, 1996.
8. D. Fang and R. K. Marcus, *Spectrochimica Acta, Part B: Atomic Spectroscopy*, 1990, **45B**, 1053-1074.
9. E. S. Oxley, The microsecond pulsed glow discharge: developments in time-of-flight mass spectrometry and atomic emission spectrometry. Ph.D. dissertation, University of Florida, Gainesville, Florida, 2002.
10. G. F. Weston, *Cold Cathode Glow Discharge Tubes*, Iliffe. 1968.
11. J. M. Schroerer, T. N. Rhodin and R. C. Bradley, *Surface Science*, 1972, **34**, 571-580.
12. R. V. Stuart and G. K. Wehner, *Journal of Applied Physics*, 1964, **35**, 1819-1824.
13. C. G. Bruhn, B. L. Bentz and W. W. Harrison, *Analytical Chemistry*, 1978, **50**, 373-375.
14. C. G. Bruhn and W. W. Harrison, *Analytical Chemistry*, 1978, **51**, 16-21.
15. E. Oxley, C. Yang and W. W. Harrison, *Journal of Analytical Atomic Spectrometry*, 2000, **15**, 1241-1245.
16. P. Sigmund, *Physical Review*, 1969, **184**, 383-416.
17. P. W. J. M. Boumans, *Analytical Chemistry*, 1972, **44**, 1219-1228.
18. N. Laegreid and G. K. Wehner, *Journal of Applied Physics*, 1961, **32**, 365-369.
19. K. Wagatsuma, *Glow Discharge Optical Emission Spectrometry*, 1997, 167-175.
20. R. L. Smith, D. Serxner and K. R. Hess, *Analytical Chemistry*, 1989, **61**, 1103-1108.

21. E. B. M. Steers and R. J. Fielding, *Journal of Analytical Atomic Spectrometry*, 1987, **2**, 239-244.
22. E. B. M. Steers and F. Leis, *Journal of Analytical Atomic Spectrometry*, 1989, **4**, 199-204.
23. A. Bogaerts and R. Gijbels, *Spectrochimica Acta, Part B: Atomic Spectroscopy*, 1998, **53B**, 1-42.
24. A. Bogaerts, L. Wilken, V. Hoffmann, R. Gijbels and K. Wetzig, *Spectrochimica Acta, Part B: Atomic Spectroscopy*, 2001, **56B**, 551-564.
25. E. W. Eckstein, J. W. Coburn and E. Kay, *International Journal of Mass Spectrometry and Ion Physics*, 1975, **17**, 129-138.
26. B. L. Bentz, C. G. Bruhn and W. W. Harrison, *International Journal of Mass Spectrometry and Ion Physics*, 1978, **28**, 409-425.
27. K. R. Hess and W. W. Harrison, *Analytical Chemistry*, 1988, **60**, 691-696.
28. K. C. Smyth, B. L. Bentz, C. G. Bruhn and W. W. Harrison, *Journal of the American Chemical Society*, 1979, **101**, 797-799.
29. W. Vieth and J. C. Huneke, *Spectrochimica Acta, Part B: Atomic Spectroscopy*, 1991, **46B**, 137-153.
30. W. W. Harrison and W. Hang, *Journal of Analytical Atomic Spectrometry*, 1996, **11**, 835-840.
31. W. W. Harrison, W. Hang, X. Yan, K. Ingeneri and C. Schilling, *Journal of Analytical Atomic Spectrometry*, 1997, **12**, 891-896.
32. E. Oxley, C. Yang, J. Liu and W. W. Harrison, *Analytical Chemistry*, 2003, **75**, 6478-6484.
33. C. Yang, M. Mohill and W. W. Harrison, *Journal of Analytical Atomic Spectrometry*, 2000, **15**, 1255-1260.
34. H. Schuler and H. Gollnow, *Zeitschrift fuer Physik*, 1935, **93**, 611-619.
35. W. Grimm, *Spectrochimica Acta, Part B: Atomic Spectroscopy*, 1968, **23**, 443-454.
36. C. M. Barshick, D. C. Duckworth, D. H. Smith and Editors, *Inorganic Mass Spectrometry: Fundamentals and Applications. [In: Pract. Spectrosc., 2000; 23]*. 2000.
37. S. L. Mandelstam and V. V. Nedler, *Spectrochimica Acta*, 1961, **17**, 885-894.
38. W. W. Harrison, C. Yang and E. Oxley, *Glow Discharge Plasmas in Analytical Spectroscopy*, 2003, 71-96.
39. W. A. Mattson, B. L. Bentz and W. W. Harrison, *Analytical Chemistry*, 1976, **48**, 489-491.

40. W. W. Harrison, C. M. Barshick, J. A. Klingler, P. H. Ratliff and Y. Mei, *Analytical Chemistry*, 1990, **62**, 943A-949A.
41. J. A. C. Broekaert, *Glow Discharge Spectrosc.*, 1993, 113-174.
42. A. Bengtson and L. Danielsson, *Thin Solid Films*, 1985, **124**, 231-236.
43. K. Wagatsuma and S. Suzuki, *Fresenius' Journal of Analytical Chemistry*, 1997, **358**, 581-584.
44. C. Yang, K. Ingeneri, M. Mohill and W. W. Harrison, *Analytical Chemistry*, 1999, **71**, 5328-5334.
45. A. Bengtson, C. Yang and W. W. Harrison, *Journal of Analytical Atomic Spectrometry*, 2000, **15**, 1279-1284.
46. R. Payling, D. G. Jones, A. Bengtson and Editors, *Glow Discharge Optical Emission Spectrometry*. 1997.
47. K. Wetzig, S. Baunack, V. Hoffmann, S. Oswald and F. Prassler, *Fresenius' Journal of Analytical Chemistry*, 1997, **358**, 25-31.
48. C. Yang, K. Ingeneri and W. W. Harrison, *Journal of Analytical Atomic Spectrometry*, 1999, **14**, 693-698.
49. C. Yang, K. Ingeneri, M. Mohill and W. W. Harrison, *Journal of Analytical Atomic Spectrometry*, 2000, **15**, 73-78.
50. A. Montaser, *Inductively Coupled Plasma Mass Spectrometry*, Wiley-VCH, Inc. 1998.
51. *Personal communications with Fred Smith, CETAC Corp*, 2009.
52. M. A. Tarr, G. Zhu and R. F. Browner, *Applied Spectroscopy*, 1991, **45**, 1424-1432.
53. K. Willeke and P. A. Baron, *Aerosol Measurement: Principles Techniques and Applications*, Van Nostrand Reinhold. 1993.
54. C. J. Tsai, H. M. Chein, S. T. Chang and J. Y. Kuo, *Journal of Aerosol Science*, 1998, **29**, 839-853.
55. http://frontpage.okstate.edu/nanotech/Assignments/Readings/DSL/primer_particle_sizing_static.pdf.
56. R. H. Clifford, H. Tan, H. Liu and A. Montaser, *Spectrochim. Acta, Part B*, 1993, **48B**, 1221-1235.
57. http://www.ceramicindustry.com/Articles/Cover_Story/f8997184a6ac7010VgnVCM100000f932a8c0.

58. K. Willeke and P. A. Baron, *Aerosol Measurement: Principles Techniques and Applications*, Van Nostrand Reinhold. 2001.
59. H.-R. Kuhn, J. Koch, R. Hergenroeder, K. Niemax, M. Kalberer and D. Guenther, *Journal of Analytical Atomic Spectrometry*, 2005, **20**, 894-900.
60. J. H. Seinfeld and S. N. Pandis, *Atmospheric Chemistry and Physics: From Air Pollution to Climate Change*, John Wiley & Sons, Inc. 1996.
61. P. F. Decarlo, J. G. Slowic, D. R. Worsnop, P. Davidovits and J. L. Jimenez, *Aerosol Science and Technology*, 2004, **38**, 1185-1205.
62. M. V. B. Krishna and R. K. Marcus, *Spectrochimica Acta, Part B: Atomic Spectroscopy*, 2008, **63B**, 673-684.
63. J. Castro, M. V. B. Krishna and R. K. Marcus, *American Laboratory (Shelton, CT, United States)*, 2008, **40**, 8-10.
64. T. M. Brewer, J. Castro and R. K. Marcus, *Spectrochimica Acta, Part B: Atomic Spectroscopy*, 2006, **61B**, 134-149.
65. T. M. Brewer, B. Fernandez and R. K. Marcus, *Journal of Analytical Atomic Spectrometry*, 2005, **20**, 924-931.
66. T. E. Gibeau and R. K. Marcus, *Analytical Chemistry*, 2000, **72**, 3833-3840.
67. C. M. Strange and R. K. Marcus, *Spectrochimica Acta, Part B: Atomic Spectroscopy*, 1991, **46B**, 517-526.
68. W. Hang, C. Baker, B. W. Smith, J. D. Winefordner and W. W. Harrison, *Journal of Analytical Atomic Spectrometry*, 1997, **12**, 143-149.
69. A. Sola-Vazquez, A. Martin, J. M. Costa-Fernandez, R. Pereiro and A. Sanz-Medel, *Analytical Chemistry (Washington, DC, United States)*, 2009, **81**, 2591-2599.
70. S. Wang and M. V. Johnston, *International Journal of Mass Spectrometry*, 2006, **258**, 50-57.
71. J. T. Jayne, D. C. Leard, X. Zhang, P. Davidovits, K. A. Smith, C. E. Kolb and D. R. Worsnop, *Aerosol Science and Technology*, 2000, **33**, 49-70.
72. A. C. Aiken, P. F. DeCarlo, J. H. Kroll, D. R. Worsnop, J. A. Huffman, K. S. Docherty, I. M. Ulbrich, C. Mohr, J. R. Kimmel, D. Sueper, Y. Sun, Q. Zhang, A. Trimborn, M. Northway, P. J. Ziemann, M. R. Canagaratna, T. B. Onasch, M. R. Alfarra, A. S. H. Prevot, J. Dommen, J. Duplissy, A. Metzger, U. Baltensperger and J. L. Jimenez, *Environmental Science & Technology*, 2008, **42**, 4478-4485.
73. S. J. Ray and G. M. Hieftje, *Analytica Chimica Acta*, 2001, **445**, 35-45.

74. J. P. Guzowski, Jr. and G. M. Hieftje, *Journal of Analytical Atomic Spectrometry*, 2000, **15**, 27-36.
75. D. Fliegel, R. Waddell, V. Majidi, D. Guenther and C. L. Lewis, *Analytical Chemistry*, 2005, **77**, 1847-1852.
76. C. L. Lewis, M. A. Moser, D. E. Dale, Jr., W. Hang, C. Hassell, F. L. King and V. Majidi, *Analytical Chemistry*, 2003, **75**, 1983-1996.
77. C. L. Lewis, M. A. Moser, W. Hang, D. E. Dale, Jr., D. C. Hassell and V. Majidi, *Journal of Analytical Atomic Spectrometry*, 2003, **18**, 629-636.
78. V. Majidi, M. Moser, C. Lewis, W. Hang and F. L. King, *Journal of Analytical Atomic Spectrometry*, 2000, **15**, 19-25.
79. H. A. Wilson, *Physical Review*, 1916, **8**, 227-237.
80. G. O. Nelson, *Controlled Test Atmospheres*, Ann Arbor Science, Ann Arbor, Michigan. 1980.
81. R. C. Weast, *CRC Handbook of chemistry and physics*, Boca Raton, Fl. 1986.
82. I. N. Levine, *Physical Chemistry. 2nd Ed*, McGraw-Hill. 1983.
83. H. Steckel, F. Eskandar and K. Witthohn, *Journal of Aerosol Medicine*, 2003, **16**, 417-432.
84. J. S. Becker and H.-J. Dietze, *International Journal of Mass Spectrometry*, 2003, **228**, 127-150.
85. S. F. Durrant and N. I. Ward, *Journal of Analytical Atomic Spectrometry*, 2005, **20**, 821-829.
86. C. C. Garcia, M. Waelle, H. Lindner, J. Koch, K. Niemax and D. Guenther, *Spectrochimica Acta, Part B: Atomic Spectroscopy*, 2008, **63B**, 271-276.
87. M. Tariq and D. Gunther, *Spectrochimica Acta, Part B: Atomic Spectroscopy*, 2009, In Press, Accepted Manuscript.
88. T. M. Naeem, H. Matsuta and K. Wagatsuma, *Analytical and Bioanalytical Chemistry*, 2004, **379**, 115-119.
89. T. M. Naeem, H. Matsuta and K. Wagatsuma, *Analytical Sciences*, 2004, **20**, 1717-1720.
90. C. Lewis, S. K. Doorn, D. M. Wayne, F. L. King and V. Majidi, *Applied Spectroscopy*, 2000, **54**, 1236-1244.
91. K. R. Hess and W. W. Harrison, *Oxford Series on Optical Sciences*, 1990, **1**, 205-222.

92. J. T. Shelley, S. J. Ray and G. M. Hieftje, *Analytical Chemistry (Washington, DC, United States)*, 2008, **80**, 8308-8313.
93. C. C. Garcia, H. Lindner and K. Niemax, *Journal of Analytical Atomic Spectrometry*, 2009, **24**, 14-26.
94. D. Guenther and B. Hattendorf, *TrAC, Trends in Analytical Chemistry*, 2005, **24**, 255-265.
95. J. Koch and D. Guenther, *Analytical and Bioanalytical Chemistry*, 2007, **387**, 149-153.
96. B. Fernandez, F. Claverie, C. Pecheyran and O. F. X. Donard, *TrAC, Trends in Analytical Chemistry*, 2007, **26**, 951-966.
97. K. Niemax, *Fresenius J Anal Chem*, 2001, **370**, 332-340.
98. C. C. Garcia, H. Lindner and K. Niemax, *Spectrochimica Acta, Part B: Atomic Spectroscopy*, 2007, **62B**, 13-19.
99. I. Horn and D. Gunther, *Applied Surface Science*, 2003, **207**, 144-157.
100. S. M. Eggins, L. P. J. Kinsley and J. M. G. Shelley, *Applied Surface Science*, 1998, **127-129**, 278-286.
101. A. Bogaerts and R. Gijbels, *Journal of Analytical Atomic Spectrometry*, 2000, **15**, 895-905.
102. A. Bogaerts, A. Okhrimovskyy and R. Gijbels, *Journal of Analytical Atomic Spectrometry*, 2002, **17**, 1076-1082.
103. G. Gamez, A. Bogaerts and G. M. Hieftje, *Journal of Analytical Atomic Spectrometry*, 2006, **21**, 350-359.
104. M. Balcerzak, *Analytical Sciences*, 2003, **19**, 979-981.
105. M. Hola, K. Novotny, J. Kaiser, D.W. Hahn, P.K. Diwakar, J. Kalvoda, Hana Novakova and V. Kanicky, Elemental distribution in fish scales using LIBS and LA-ICP-MS methods, Poster presentation, North America Laser Induced Breakdown Spectroscopy Symposium, New Orleans, LA, United States, July 2009.
106. J. Kaiser, M. Hola, K. Novotny, D. W. Hahn, P. K. Diwakar, R. Malina, M. Galiova, V. Kanicky and M. Liska, LIBS and LA-ICP-MS complementary study of uroliths, Poster presentation, North America Laser Induced Breakdown Spectroscopy Symposium, New Orleans, LA, United States, July 2009.
107. A. Bauer, J. Black, M. Schmidt and A. J. R. Bauer, LIBS Analysis of Hematite Under a Mars-like Atmosphere, Poster presentation, North America Laser Induced Breakdown Spectroscopy Symposium, New Orleans, LA, United States, July 2009.

BIOGRAPHICAL SKETCH

Farzad was born in the city of Mashhad, in the province of Khorasan, Iran. He finished high school in 1996, after winning the National gold medal in Chemistry Olympiad in 1995. He got his B.Sc. in chemistry from the University of Tehran-Iran in 1999, and went on to mentor the Iranian team for the 32nd International Chemistry Olympiad in Denmark in July 2000. It was there that he received a visitor visa from the American embassy in Copenhagen.

In August 2000, Farzad came to the United States and spent six months in Berkeley, California, where he participated in English classes in Berkeley adult school and took the GRE and TOEFL exams.

From January 2001 to August 2003, Farzad worked toward his master's degree in Professor Jason Telford's research group at the University of Iowa, where his research focused on organic synthesis of calixarene and cyclodextrine derivatives.

Farzad began his Ph.D. studies at the University of Florida in 2003. He started his research as a graduate student under the supervision of Professor Nicolo Omenetto in the fall of 2004. His research focuses on fundamental aspects of pulsed glow discharge mass spectrometry and investigation of particle ionization in the pulsed discharge, using time-of-flight mass spectrometry. He also worked for a short period of time in 2003, in Dr. Martin's laboratory, on making single conical nano pores on polycarbonate membranes. During his time at the University of Florida, Farzad was a teaching assistant for multiple courses and labs, including general, inorganic, organic, physical and analytical chemistry.

Farzad defended his Ph.D. dissertation on July 24, 2009 and obtained his Ph.D. in analytical chemistry in August 2009.